STRUCTURAL OPTIMIZATION OF COMPOSITE HELICOPTER ROTOR BLADES

A THESIS SUBMITTED TO
THE GRADUATE SCHOOL OF NATURAL AND APPLIED SCIENCES
OF
MIDDLE EAST TECHNICAL UNIVERSITY

BY

ALPEREN AYBERK IŞIK

IN PARTIAL FULFILLMENT OF THE REQUIREMENTS
FOR
THE DEGREE OF MASTER OF SCIENCE IN
AEROSPACE ENGINEERING

MAY 2018

Approval of the thesis:

STRUCTURAL OPTIMIZATION OF COMPOSITE HELICOPTER ROTOR BLADES

submitted by **ALPEREN AYBERK IŞIK** in partial fulfillment of the requirements for the degree of **Master of Science in Aerospace Engineering Department, Middle East Technical University** by,

Prof. Dr. Halil Kalıpçılar
Dean, Graduate School of **Natural and Applied Sciences** _____

Prof. Dr. Ozan Tekinalp
Head of Department, **Aerospace Engineering** _____

Prof. Dr. Altan Kayran
Supervisor, **Aerospace Engineering Dept., METU** _____

Examining Committee Members:

Prof. Dr. Ozan Tekinalp
Aerospace Engineering Dept., METU _____

Prof. Dr. Altan Kayran
Aerospace Engineering Dept., METU _____

Assoc. Prof. Dr. Demirkan Çöker
Aerospace Engineering Dept., METU _____

Assoc. Prof. Dr. Ercan Gürses
Aerospace Engineering Dept., METU _____

Prof. Dr. Erdem Acar
Mechanical Engineering Dept., TOBB
University of Economics and Technology _____

Date: 11.05.2018

I hereby declare that all information in this document has been obtained and presented in accordance with academic rules and ethical conduct. I also declare that, as required by these rules and conduct, I have fully cited and referenced all material and results that are not original to this work.

Name, Last Name: Alperen Ayberk, Işık

Signature:

ABSTRACT

STRUCTURAL OPTIMIZATION OF COMPOSITE HELICOPTER ROTOR BLADES

Işık, Alperen Ayberk

M.Sc., Department of Aerospace Engineering

Supervisor : Prof. Dr. Altan Kayran

April 2018, 142 pages

Structural optimization of a helicopter rotor blade with uniform aerodynamic surface and twist at the functional region is performed for weight minimization subject to various constraints relevant to helicopter rotor blades. The genetic algorithm based optimization is performed only for the functional region of the blade. Design variables are taken as the number of unidirectional S-glass layers in the spar cap, position of the spar web with respect to the leading edge, nose mass diameter and position of the single spanwise ply-drop-off. Constraints of the structural optimization are defined as maximum strain in the critical sections of the blade in the functional region, relative distances between the feathering axis, mass center, shear center and the neutral axis and natural frequency limits. Optimization is performed in a stepwise fashion for the hover condition and the sectional analysis of the blade is performed by Variational Asymptotic Beam Section (VABS) method. Loads and natural frequencies of the blade are calculated by the multibody simulation tool Dymore. The initial sectional blade loads calculated by Dymore are kept constant and they are not updated in any design iteration during the optimization process. For the optimized blade properties, blade tuning is done by lumped mass attachment to the blade and the sectional blade loads are calculated again by Dymore and another optimization is performed again by keeping the sectional loads as constant in any design iteration of optimization process. Load calculation, blade tuning and optimization cycle is repeated until the sectional

loads calculated by Dymore do not change within a prescribed tolerance to complete full blade optimization. With this approach, the time consuming sectional load calculation process by Dymore is eliminated. The results of the study showed that 16.55% mass reduction could be achieved in the functional region of the blade with respect to the baseline design.

Keywords: Helicopter rotor blade, composites, optimization, blade natural frequency, genetic algorithm.

ÖZ

KOMPOZİT HELİKOPTER ROTOR PALLERİNİN YAPISAL OPTİMİZASYONU

Işık, Alperen Ayberk
Yüksek Lisans, Havacılık ve Uzay Mühendisliği Bölümü
Tez Yöneticisi : Prof. Dr. Altan Kayran

Nisan 2018, 142 sayfa

Helikopter rotor palleri ile ilgili çeşitli kısıtlamalara maruza kalan ağırlık minimizasyonu için fonksiyonel bölgesi değişmeyen aerodinamik yüzeye ve sabit burulma oranına sahip olan helikopter pallerinin yapısal optimizasyonu icra edilir. Genetik algoritma tabanlı optimizasyon sadece pallerin fonksiyonel bölgesi için yapılır. Tasarım değişkenleri; spardaki tek yönlü S-glass tabakalarının sayısı, spar duvarının hücum kenara göre konumu, burun kütlesinin çapı ve pal doğrultusundaki tek istasyonda gerçekleşen spardaki kompozit kat azalma pozisyonu olarak alınır. Yapısal optimizasyonun kısıtlamaları; palin fonksiyonel bölgesinin kritik bölümlerindeki maksimum gerinim, hatve ekseni ile kütle merkezi, kesme merkezi ve nötr eksen aralarındaki mesafeler ve doğal frekans sınırlarıdır. Optimizasyon, askıda uçan bir helikopter pali için kademeli olarak yapılır ve palin kesit analizi, Variational Asymptotic Beam Section (VABS) metodu ile gerçekleştirilir. Palin yükleri ve doğal frekansları, çoklu gövdeli simülasyon aracı Dymore tarafından hesaplanır. Dymore tarafından hesaplanan ilk pal kesit yükleri sabit tutulur ve optimizasyon işlemi sırasındaki herhangi bir tasarım iterasyonunda güncellenmezler. Optimize edilmiş pal özellikleri için, pal frekans ayarlaması, pale eklenen yığılı kütle ile yapılır ve pal kesit yükleri Dymore tarafından tekrar hesaplanır ve bir başka optimizasyon, optimizasyon işleminin herhangi bir tasarım yinelemesinde, kesit yüklerini sabit tutarak tekrar gerçekleştirilir. Yük hesaplama, pal frekansı ayarlama ve optimizasyon döngüsü,

Dymore tarafından hesaplanan kesit yüklerinin, tüm pal optimizasyonunu tamamlamak için öngörülen bir tolerans dahilinde değişmediği sürece tekrarlanır. Bu yaklaşımla, Dymore tarafından gerçekleştirilen ve zaman harcatan kesitsel yük hesaplama süreci ortadan kaldırılmıştır. Çalışmanın sonuçları, referans pal tasarımına göre palin fonksiyonel bölgesinde %16,55 oranında kütle azalmasının sağlanabileceğini göstermiştir.

Anahtar Kelimeler: Helikopter rotor pali, kompozitler, optimizasyon, pal doğal frekansı, genetik algoritma.

To my father Dr. Yusuf IŞIK who taught me the value of the knowledge

ACKNOWLEDGEMENTS

First of all, I would like to express my deepest gratitude to my supervisor Prof. Dr. Altan Kayran for his invaluable criticism, supervision and support throughout this study.

I indebted to my coworker Murat Günel, my manager Serkan Özbay and consultant of my department Mithat Yüce for their guidance on structures area and helicopter field. I am also grateful to my colleagues Melek Esra Erdem and Anıl Koçkar for their support.

I also would like thank to M. Emre Bilen for his help on modelling of helicopter dynamics and my sister Özlem Aybüke Işık for her helps on editing thesis.

Finally, I would like to express my gratitude to my mother Firdes IŞIK and other members of my family for their constant support, love and patience.

TABLE OF CONTENTS

ABSTRACT v
ÖZ vii
ACKNOWLEDGEMENTS x
TABLE OF CONTENTS xi
LIST OF TABLES xiii
LIST OF FIGURES xiv
LIST OF SYMBOLS AND ABBREVIATONS xvi
CHAPTERS
1. INTRODUCTION 1
1.1 General Review 1
1.2 Literature Survey 2
1.2.1 Application of Composites for Helicopter Rotor Blades 2
1.2.2 Blade Modelling 3
1.2.3 Optimization Methods 5
1.2.4 Studies on Rotor Blade Optimization 5
1.3 Motivation of the Thesis 7
1.4 Objective and the Scope of the Thesis 7
2. DESCRIPTION OF THE PROBLEM & MODELLING 11
2.1 Helicopter Rotor Blade and the Baseline Blade Design 11
2.2 Critical Design Constraints 15
2.3 Modelling 20
2.3.1 Theory of Modelling 20
2.3.2 General Approach for Modelling 22
2.3.3 Reference Axis System & Twist Definition 24
2.3.4 Composite Material Axis System Definition 26
2.3.5 2D Cross-Section FE Model of Blade Sections 28
2.3.6 Mesh Convergence Study of 2D Cross-Section Analysis 36
2.3.7 Simplified Multi-Body Model of Rotor and 1D Beam Blade FE Model… 38

2.3.8 Mesh Convergence Study of the 1D Beam Blade Analysis 39
3. OPTIMIZATION OF THE HELICOPTER ROTOR BLADE 43
3.1 Optimization Approach 43
3.2 Design Variables 44
3.3 Cross-Section Optimization (CSO) 46
3.3.1 Genetic Algorithm (GA) 46
3.3.2 Cross-Section Optimization (CSO) Constraints 57
3.3.3 Objective Function for the Cross-Section Optimization (CSO) 59
3.3.4 Convergence Criterion for the Cross-Section Optimization (CSO) . 60
3.3.5 Cross-Section Optimization (CSO) Case Studies 61
3.4 Full-Blade Optimization (FBO) 62
3.4.1 Full-Blade Optimization (FBO) Constraints 62
3.4.2 Blade Tuning 63
3.4.3 Calculation of the Blade Loads 69
3.4.4 Convergence Criterion for the Full-Blade Optimization (FBO) 70
3.4.5 Extended Flow Chart of the Optimization Approach 71
4. RESULTS 73
4.1 Case Study Results 73
4.2 Full-Blade Optimization (FBO) Results 76
5. CONCLUSION 91
REFERENCES 95
APPENDICIES
A. STIFFNESS AND MASS MATRIX TERMS & DEFINITION OF CRITICAL CENTERS 101
B. MATERIAL PROPERTY TABLE 103
C. PREVABS INPUT EXAMPLE 105
D. VABS INPUT FILE EXAMPLE 117
E. PENALTY PARAMETER, POPULATION SIZE AND CONVERGENCE CRITERION SELECTION FOR CROSS-SECTION OPTIMIZATION (CSO) 119

LIST OF TABLES

TABLES

Table 1 Main Design Parameters 15
Table 2 Component-Material Table 15
Table 3 Components of Cross-Section Reference Axis 24
Table 4 Components of the Materials Axis Systems 28
Table 5 Normalized Natural Frequencies of the Baseline Blade Model 65
Table 6 Comparison of the Baseline Design with the Optimized Designs Obtained in Case Studies 1-4 74
Table 7 Normalized Natural Frequencies of FBO Iterations 80
Table 8 Full Blade Optimization (FBO) Results 90

Table A1 Terms of Stiffness Matrix 102
Table A2 Terms of Mass Matrix 102

Table B1 Material Property Table 103

Table E1 Outputs Obtained from the Case Study Trials for Various Penalty Parameters and Population Sizes 121

LIST OF FIGURES

FIGURES

Figure 1 Main Regions of the Helicopter Rotor Blade 11
Figure 2 Cross-Section Model of the Functional Region 14
Figure 3 Typical Fan Plot 19
Figure 4 Beam Model Description of the Helicopter Rotor Blade [37] 23
Figure 5 General Approach for Blade Modelling 23
Figure 6 Reference system for blade cross-sectional properties 24
Figure 7 Twist reference 25
Figure 8 Blade twist distribution 26
Figure 9 Material Axis Systems 27
Figure 10 Sketch of a typical blade cross-section [37] 30
Figure 11 Segment-Subcomponent Relation Description Schema of Baseline Blade 31
Figure 12 Core Meshes of Honeycomb, Nose Block and the Cylindrical Nose Weight 32
Figure 13 Neighbor Node- Parent Element Relation 33
Figure 14 Inner and Outer Boundaries 33
Figure 15 Nose Block and Nose Mass Additional Mesh Seeds 34
Figure 16 Nose Block and Nose Mass Mesh Boundaries 35
Figure 17 *RMS* Selection Study for Cross-Section Analysis 37
Figure 18 Multi Body Model of the Rotor 39
Figure 19 Mesh Convergence Study for the Beam Blade 41
Figure 20 Optimization Flow Chart 44
Figure 21 Design Variables (X_1, X_2 and X_3) 45
Figure 22 Design Variables (X_4) 45
Figure 23 Flowchart of a Typical GA 47
Figure 24 Real-valued Coding 48
Figure 25 Representation of Binary Coded Population in GA 49

Figure 26 Representation of Real-Value Coded Population in GA 49
Figure 27 Real-Valued Chromosome Example Used in CSO 50
Figure 28 Single Point Crossover 53
Figure 29 Binary Mutation 53
Figure 30 Spread of Offsprings [44] 54
Figure 31 Reproduction Illustration of Real-Value Coded Genes 55
Figure 32 Illustration of Natural Frequency Constraints 63
Figure 33 Fan Plot of the Baseline Blade Model 65
Figure 34 Frequency Tuning of the Bending Modes 67
Figure 35 Mode Shapes of the Baseline Blade Model 68
Figure 36 Extended Optimization Flow Chart 72
Figure 37 Fitness Variation of Case Studies 75
Figure 38 Spanwise Distribution of Axial, Chordwise and Flapwise Forces for ongoing FBO Iterations 77
Figure 39 Spanwise Distribution of Torsional, Flapwise Bending and Chordwise Bending Moments for ongoing FBO Iterations 78
Figure 40 Fan Plot Representations of FBO Iterations 79
Figure 41 Mode Shapes of FBO Iterations with Their Tuned Versions 82
Figure 42 Fitness Variation for Iteration 1, 2 and 3 in FBO 82
Figure 43 Cross-Sections of the Baseline and the Optimized Blades 84
Figure 44 Spanwise Mass Property Distributions of the Optimized Blade 85
Figure 45 Spanwise Distributions of Normalized Stiffness Properties of the Optimized Blade 86
Figure 46 Spanwise Distributions of Sectional Centers (CG, SC and NA) with respect to the FA 87
Figure 47 Cross-Sectional Strain Distribution at the Root of the Baseline Blade 89
Figure 48 Cross-Sectional Strain Distribution at the a) Root and b) Drop-off Position of the Optimized Blade 89

Figure E1 Fitness Variation and Convergence Details of Case Study 4 122

LIST OF SYMBOLS AND ABBREVIATONS

Symbols

1D, 2D, 3D	One, two and three dimensional
ω_n	n'th natural frquency
ω	Current rotor speed
ω_{ref}	Operational rotor frequency
S_{ref}	Cross-sectional reference axis system
ϕ	Cross-sectional twist angle
Θ	Ply orientation angle
e	Material direction based reference axis system
y	Aerodynamic surface based reference axis system
RMS	Relative Mesh Size
#N	Number of nodes
i	Number of individuals in a population
v	Number of variables in s chromosome
b	Number of bits used to define a variable in a binary coded chromosome
#Individuals	Total number of individuals in population
#Elite	Number of elites in population
#Crossover	Number of crossover individuals in population
#Mutation	Number of mutation individuals in population
CL	Chord length
$R_{baseline}$	Cylindrical nose mass radius of baseline blade

$STA_{INITIAL}$	Spanwise starting position of the functional region
STA_{FINAL}	Spanwise ending position of the functional region
BS	Blade Span Length
S_{max}	Maximum cross-sectional strain in spanwise direction
CG_n	Non-dimensional chordwise center of gravity position w.r.t. feathering axis
NA_n	Non-dimensional chordwise neutral axis position w.r.t. feathering axis
SC_n	Non-dimensional chordwise shear center position w.r.t. feathering axis
Φ	Objective function
f	Weight function
r	Penalty parameter
$Constraint_k$	k'th normalized constraint
CG_{n_Thick}	CG_n value of the optimized blade before spanwise spar drop-off position
NA_{n_Thick}	NA_n value of the optimized blade before spanwise spar drop-off position
SC_{n_Thick}	SC_n value of the optimized blade before spanwise spar drop-off position
S_{MAX_Thick}	S_{max} value of the optimized blade at the root of the blade
CG_{n_Thin}	CG_n value of the optimized blade after spanwise spar drop-off position
NA_{n_Thin}	NA_n value of the optimized blade after spanwise spar drop-off position
SC_{n_Thin}	SC_n value of the optimized blade after spanwise spar drop-off position

S_{MAX_Thin}	S_{max} value of the optimized blade at the end of spanwise spar drop-off
I	Iteration Number
I_{max}	Maximum Iteration Number
X_1, X_2, X_3, X_4	Design variables 1,2,3 and 4
$Flap_1$, $Flap_2$, $Flap_3$	First, second and third flap modes of the blade
$Torsion_1$	First torsion mode of the blade
Lag_1	First lead-lag mode of the blade
F_1, F_2, F_3	Cross-sectional force components w.r.t S_{ref} at 200% operational rotor speed
M_1, M_2, M_3	Cross-sectional moment components w.r.t S_{ref} at 200% operational rotor speed
$F_{1(j)}$, $M_{2(j)}$, $M_{3(j)}$	F_1, M_2 and M_3 values at j'th iteration of FBO
$S_{i,j}$	Term at the i'th row and j'th column of the stiffness matrix
μ	Mass per spanwise length
m_{11}	Polar mass moment of inertia
m_{22}	Flapwise mass moment of inertia
m_{33}	Chordwise mass moment of inertia
m_{23}	Product of Inertia
x_{m2}, x_{m3}	Falpwise and chordwise center of gravity position w.r.t. feathering axis
x_{s2}, x_{s3}	Falpwise and chordwise shear center position w.r.t. feathering axis
x_{t2}, x_{t3}	Falpwise and chordwise neutral axis position w.r.t. feathering axis
E_{ii}	Elastic moduli in i direction
G_{ij}	Shear modulus
v_{ij}	Poison's Ratio

Abbreviations

VABS	Variational Asymptotic Beam Sectional Analysis
FE	Finite element
FEM	Finite element method
FEA	Finite element analysis
GA	Genetic Algorithm
CG	Center of gravity
SC	Shear center
NA	Neutral axis
FA	Feathering Axis
UD	Uni-directional
FAA	Federal Aviation Administration
VAM	Variational Asymptotic Method
AC	Aerodynamic Center
CAD	Computer Aided Drawing
CSO	Cross-Section Optimization
FBO	Full Blade Optimization
UTS	Ultimate Tensile Strain

CHAPTER 1

INTRODUCTION

1.1 General Review

Weight minimization has a critical role for helicopters as in aircraft in order to increase the flight performance.

Considering the number of rotor blades and their internal structure, blades have high weight contribution to the overall weight of the helicopter.

Composite materials have been widely used in the helicopter blades due to the high specific strength of composite. Structural optimization of composite helicopter blades is crucial for performance enhancement and to reduce the risk of aeroelastic instabilities associated with helicopter blades. Furthermore, the rotation motion generates cyclic loads on the rotor blade. Therefore, using composites is more advantageous than using metallic materials because of their superior fatigue strength.

Besides weight minimization, achieving dynamic and static feasible conditions is essential. While it is necessary to have necessary strength for the operating helicopter blades, natural frequencies of the blade and various sectional properties such as distance between the center of gravity (CG) and the feathering axis (FA) positions etc., have to be checked and adjusted accordingly from the dynamic point of view.

Weight minimization of helicopter rotor blades has retained its importance since its invention. Faster optimization methods, update of multibody solvers and more accurate FEM tools make weight minimization still a hot topic.

1.2 Literature Survey

1.2.1 Application of Composites for Helicopter Rotor Blades

Fiber-reinforced polymer composite materials are in use for half a century. Shortly after composites appeared in industry, they have been used in aerospace structures due to their superior structural properties. Today, composite content to gross weight ratio of an aircraft reaches up to 50 to 60 percent. According to Mangalgri, with the use of composites nearly 30% of overall aircraft weight savings had been estimated [1]. Weight savings in aerospace structures are dramatically increasing because of new material researches, modeling techniques, new optimization approaches and due to better understanding of failure modes.

Composite materials have superior properties. Some are worth mentioning for their utilization in the helicopter rotor blades. High fatigue strength, flexibility to tailor the blade properties such as stiffness and mass, better damage tolerance are some of the good features that composites possess. These features of composites gain importance for helicopter rotor blades which work under cyclic dynamic loading.

In the study of Salkind and Geoffry [2], the design advantages of fiber-reinforced composites in helicopter rotor blades are summarized. Application of composites in blade manufacturing enabled production of a large variety of aerodynamic shapes. Also, composite materials lead to reduction in weight which is very important in aerospace structures. The impact of weight is underlined in the following example. When empty helicopter weight is reduced by 10 percent, this reduction yields a 40 percent increase in the operational ferry range for the CH-47 helicopter. Since helicopter blades are components of the helicopter, minimizing the weight of the helicopter rotor blades is also required for the overall weight minimization of the helicopter. Previously, material weights of blades which sustain the same high cycle fatigue loading were compared by Salkind and Geoffry [2]. It was found that boron composite and S-glass composite blades are 3 times lighter than aluminum ones and

twice lighter than steel ones. Flexibility for tailoring dynamic frequencies and the structural response of the blade are perhaps the most significant advantages that composites provide. For instance, increasing the quantity of fibers oriented at $\pm 45^{o}$ with respect to the blade span leads to a significant increase in the torsional rigidity with a small change in the first flap and lag frequencies. Moreover, using $\pm 45^{o}$ plies gives the advantage of satisfying high specific torsional stiffness for the blade skins. Application of high modulus composites, such as boron or graphite composites, is more advantageous than glass-epoxy composites for tuning torsional and bending stiffness. The reason is that torsional stiffness can alter with a minimum polar moment of inertia change for high modulus materials. S-glass and boron-epoxy rotor blade spars are very common in given examples. Boron composite and S-glass unidirectional composites are also more advantageous than metals in terms of their fatigue behavior [2].

1.2.2 Blade Modelling

Due to the slender shape of the helicopter rotor blade, it can be modeled as either a 3D finite element (FE) model or as a simple model consisting of 2D FE sectional model and 1D spanwise beam model. In the literature, there are studies which compare advantages, disadvantages and theories of 3D FE and beam modeling of helicopter blades such as the one by Hodges [3]. Although the detailed 3D FE model gives more accurate results, the solution time is much higher than the beam model solutions. On the other hand, the simplification of 3D slender structures into a 2D cross-sectional and a 1D nonlinear beam model is respectably faster and gives sufficiently accurate results with the use of correct tools [3].

Cesnik and Hodges [4] developed a new method of modelling of composite rotor blades called as VABS (Variational Asymptotic Beam Sectional Analysis). The theory of VABS which is derived from geometrically nonlinear, 3D elasticity, is applicable to nonhomogeneous initially curved and twisted beams such as helicopter rotor blades

and wind turbine blades [4]. The validation of VABS is done by Yu and co-workers [5]. Various comparisons have been done for the VABS-theory of elasticity, VABS-common engineering calculations for shear center locations and VABS-ABAQUS for 3D stress and strain calculations. This study showed that VABS is at the same level of accuracy as the standard 3D FE codes but requires much lower computational time compared to finite element analysis.

Many tools exist for the 2D FE cross-sectional analysis of beams besides VABS. Chen and co-workers made a comparison between VABS, PreComb, FAROB and CROSTAB and in this study it is claimed that PreComb, FAROB, and CROSTAB all have poor and inconsistent performance for simple cross-sections [6]. For structural properties, VABS can provide the most amount of information for a given cross-section, including Euler–Bernoulli model, Timoshenko model and Vlasov model, and characteristic centers including the mass center, shear center and the neutral axis (tension center). Several benchmark examples are used to evaluate the performance of different tools and huge differences have been found among the 2D FE cross-sectional analysis tools [6].

Dymore [7] is a multibody simulation tool that is compatible with VABS. Both the cross-sectional analysis of VABS and 1D beam analysis of Dymore are derived systematically from the same framework which is proved by Han & Yu [8]. The kinematic formulation of Dymore is given by Bauchau [9]. The dynamic response of nonlinear, flexible multibody systems is simulated within the framework of energy-preserving and energy-decaying time-integration schemes. These schemes provide unconditional stability for nonlinear systems. Dymore multi body formulation is tested and validated by various benchmark problems [10]. The multi body simulation application of VABS has been conducted by Bauchau and Hodges [11] for the dynamic analysis of flexible, nonlinear multibody systems involving elastic members made of laminated, anisotropic composite materials.

1.2.3 Optimization Methods

Ku stated that, many researchers have encountered limitations in gradient based methods for the last two decades of active research in rotorcraft optimization with gradient based methods. The calculation of gradients is a major problem because the finite difference derivatives can be inaccurate unless a proper step size is used, and a feasible design must be used as the starting point. Also, analytical derivatives require extensive changes in analysis programs [12].

According to Crossley and Laananen [13], due to the characteristics of design variables in rotorcraft optimization, not all design variables can be treated as continuous and most design spaces in rotorcraft optimization problems are nonconvex, so that local optima exist. To overcome the obstacles of gradient-based methods in reaching the global optimum, the use of heuristic optimization methods such as the Genetic Algorithm (GA) has been growing.

Hajela [14] reviewed the potential of non-gradient based methods extensively. Among the many different non-gradient based methods, genetic algorithm appeared to be the best candidate due to its maturity level and capacity to incorporate other optimization schemes such as neural networks, fuzzy logic, and the immune system.

1.2.4 Studies on Rotor Blade Optimization

A similar study as the present study for rotor blade optimization is performed by Visweswaraiah and colleagues [15]. In this study, both continuous and integer design variables are used in the optimization process. In this study, optimization of the ply angles and the internal geometry of a composite helicopter blade with a D-spar internal construction is performed. The design involves the simultaneous optimization of several conflicting objectives such as minimizing the deviation from three target stiffness parameters, minimizing the blade mass and the distance between the mass-center and the aerodynamic-center.

Li and coworkers [16] applied a design strategy for helicopter rotor blade cross-section optimization considering manufacturability constraints such as the minimum ply thickness. It is explained that for a realistic cross-section optimization, a parametric meshing tool is necessary. For the cross-section model used, D-spar position, thickness and the fiber angles of the skin laminate, web and D-Spar were included as design variables. Design variables are integer and continuous. A parametric meshing tool was connected to the 2D cross-sectional analysis tool VABS to obtain sectional outputs. Sectional stiffness values, the positions of shear center and mass center were identified as values to be constrained. Results showed that distance between the mass center and the aerodynamic center can be reduced if additional nonstructural point mass is added [16]. Although the nose mass is nonstructural, the covering structure of the nose mass, which is called as the nose block, has to be structural. Hence, point mass addition to the cross-section makes the model less realistic. Many aspects were taken into account in the study such as manufacturability constraints; however, the parametric model did not include the 2D nose mass and the nose block modelling. The modelling of the nose mass and nose block creates an opportunity for a more realistic model and a feasible solution, because the mass center constraint can be satisfied by manipulating the nose mass area with the minimum effect on the other cross-sectional properties. Li and colleagues [16] used a combination of gradient based method (SQP) and non-gradient based (GA) in order to enhance the overall performance of the helicopter rotor blade optimization. Firstly, optimal solution is found by a continuous solution with SQP. Secondly, a realistic discrete solution is obtained from the continuous solution by GA.

Another detailed hybrid optimization study has been performed by J. Ku (2007) [12] for composite helicopter rotor blades. In this study, VABS has been used for cross-sectional analysis, Dymore [7] has been used for multibody solution and VABS-ANSYS macro has been used for the automated meshing of the cross-section. The analysis tools were integrated by MATLAB. In this study, two levels of optimization, at the global and the local level has been applied. Firstly, global-level optimization has been applied to determine the necessary stiffness matrix. Global-level optimization has targeted weight minimization and satisfaction of natural frequency constraints.

Secondly, ply angles and size parameters have been set as design variables to obtain necessary stiffness values in local-level optimization. In local-level optimization, in order to increase the efficiency of the optimization process, a two phase hybrid optimization has been applied. Genetic Algorithm has been applied to the population for clustering around local minima and Gradient-Based method has been employed to reach each local minimum. Finally, by the comparing the local minima, global minimum has been found.

1.3 Motivation of the Thesis

As it is mentioned earlier, weight minimization is crucial for helicopter components similar to all aircraft components. Considering the number of blades and their internal structure, it has been determined that blades have high weight contribution to the overall weight of the helicopter. In the literature, as discussed before, there are studies on helicopter blade optimization. However, most of these studies focus on more simplified blade configurations. The main motivation of the present study is to demonstrate optimization of realistic helicopter blade without overly simplifying the internal structure of the blade. It is considered that the proposed optimization methodology on a realistic helicopter blade can be readily implemented at the industrial level. This has been the main motivation of the study.

1.4 Objective and the Scope of the Thesis

In this thesis, it is aimed to carry out a stepwise optimization work for realistic helicopter rotor blade with the objective of weight minimization. To this end, necessary constraints are included in the definition of the optimization problem for feasible conditions. For the modelling of the blade, the 3D blade structure is separated into a 2D cross-section and a 1D beam. We employ this to simplify the complication of 3D modeling and analysis method. Variational Asymptotic Beam Sectional Analysis (VABS) tool is employed for the 2D modeling and cross-sectional analysis

including stress/strain recovery. For the 1D beam modeling and analysis of the beam-blade, multibody helicopter rotor simulation tool Dymore is employed. The target of the optimization procedure is weight minimization of the blade. The number of unidirectional S-glass layers in the spar cap, position of the spar web with respect to the leading edge, nose mass diameter and position of the single spanwise ply-drop-off are set as design variables. The critical design constraints are adjusted as the maximum global strain, acceptable natural frequency intervals and the sectional position limits of the center of gravity (CG), shear center (SC) and the neutral axis (NA). Before starting the optimization procedure, baseline loads are obtained from the baseline design by Dymore. The overall optimization is performed in two steps: cross-section optimization and blade tuning. In the first step, Genetic algorithm is employed with the maximum global strain, CG, SC and NA position constraints. In the first step of the optimization, cross-sectional analysis by VABS is processed for constant loads determined by the multibody simulation code Dymore. It should be noted that during the first step optimization process, when number of plies numbers changes, inertia loads on the blade also change. However, in the first step of the optimization, loads calculated for the baseline blade are taken as constant to reduce the optimization time which would increase substantially had the Dymore analysis were incorporated in each iteration during the optimization process. In the second step of the optimization, natural frequency tuning is performed by adding lumped mass to the necessary positions of the blade. This is followed by the final load calculation for the current loop of the overall optimization process. It is to be noted that the first and the second step optimizations together is named as an optimization loop. At the end of an optimization loop, blade loads are again calculated by Dymore and compared with the baseline loads. If convergence is achieved in the loads, optimization procedure is completed and if not, blade loads are updated and another loop of optimization is performed.

This thesis starts with an introduction chapter. Here, a general review and literature background is given. The motivation and objective of the study are also presented in this chapter.

In the second chapter of this thesis, the background information on helicopter rotor baseline design is given, and modelling method is explained. In this chapter, the design principals and limitations are also explained together with the literature background.

The third chapter is dedicated to the optimization approach and the background information related to the methods applied. The objective function, design variables, and design constrains are clearly explained and formulated mathematically.

In the fourth chapter, the results obtained from the case studies and complete optimization study are investigated. Charts showing the comparison between the baseline design, case studies and full blade optimization are given to highlight the virtue of this study.

In the fifth chapter, conclusions are given. Furthermore, the advantages of the methods which are used in this study are discussed. Possible enhancements are also mentioned as future work.

CHAPTER 2

DESCRIPTION OF THE PROBLEM & MODELLING

2.1 Helicopter Rotor Blade and the Baseline Blade Design

The necessary lift for the helicopter flight is produced by the helicopter main rotor blades. The rotational motion of the blade is produced by utilizing the engine torque. The torque is produced by the engines and adjusted by the transmission for the necessary rotor frequency. Relative air velocity generated due to the blade rotation and helicopter motion generates the lift mainly in the airfoil sections of the blade.

For a typical helicopter, helicopter rotor blade is composed of three main regions: the root region, transition region and the functional region (Figure 1). The root region and the transition region transmit the torque produced by the engine to the blades for the rotational motion. Since the functional region has airfoil cross-section shape, almost all of the necessary lift is produced in this region. Because of this rotational motion, a cumulative load is produced from tip to root. All the loads acting are transmitted to the rotor hub and consequently it is transmitted to helicopter body by the root and transition region.

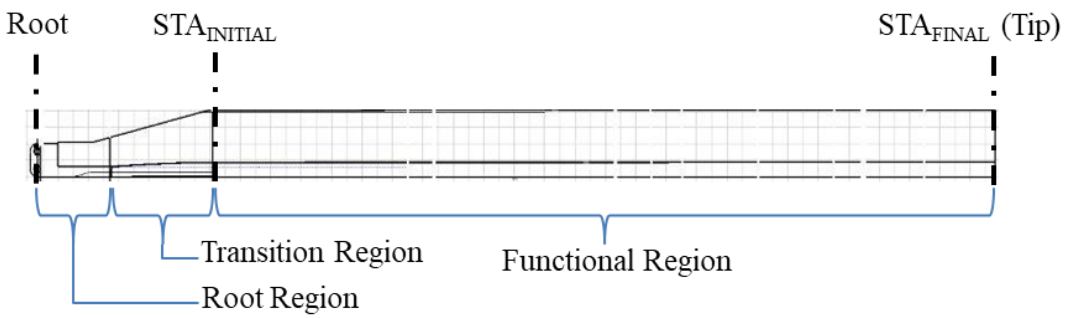

Figure 1 Main Regions of the Helicopter Rotor Blade

Due to the topology of the helicopter rotor blade, most of the blade weight is distributed along the functional region. Sectional changes of the root and the transition region do not affect the overall weight significantly. Additionally, the root region and the transition region are predominantly tailored into a topology with strength concerns. Hence, in this work, the optimization procedure is only applied to the functional region.

Concerning the blades used in this study, Figure 2 shows the baseline model of the cross-section of the blade having 420 mm chord length of a VR-12 airfoil. As it can be seen from Figure 2, the functional region of the blade contains detailed parts including the D-spar, skin, erosion shield, heater mat, film adhesive, cylindrical nose weight and the honeycomb core.

The spar is composed of spar straps, inner-outer wraps, spar wall and nose block. Spar straps, nose block and spar wall are covered by inner and outer wraps. For all spar components glass-fiber material is used. While spar straps and nose block are composed of UD plies; spar wall and inner-outer wraps are composed of ±45 deg. cross-plies. Spar straps and nose block have mainly axial and bending stiffness contributions. Spar wall and inner-outer wraps have mainly torsional and shear stiffness contributions.

The skin is composed of $\pm 45^{o}$ carbon-fiber composite cross-plies. Because of skin geometry and layup configuration, the skin mainly has torsional, shear and chordwise bending stiffness contribution.

Due to the high velocity air flow, a stainless-steel erosion shield is attached to leading edge side of the functional region. Just under the erosion shield, a dummy e-glass heater mat is modeled for deicing. To tune the chordwise center of gravity position, a cylindrical nose weight made of lead is embedded in the nose block. Finally, a honeycomb completes the sandwich between upper and lower skin and has transverse shear contribution. The baseline design parameters for the cross-section of the functional region are listed Table 1. As seen in Table 1, the preliminary design is made based on centrifugal and inertia loading only and aerodynamic load is not taken into

account because the centrifugal and inertial loads are more critical and predictable in this stage. The components of the functional region with the corresponding materials and layups are listed in Table 2.

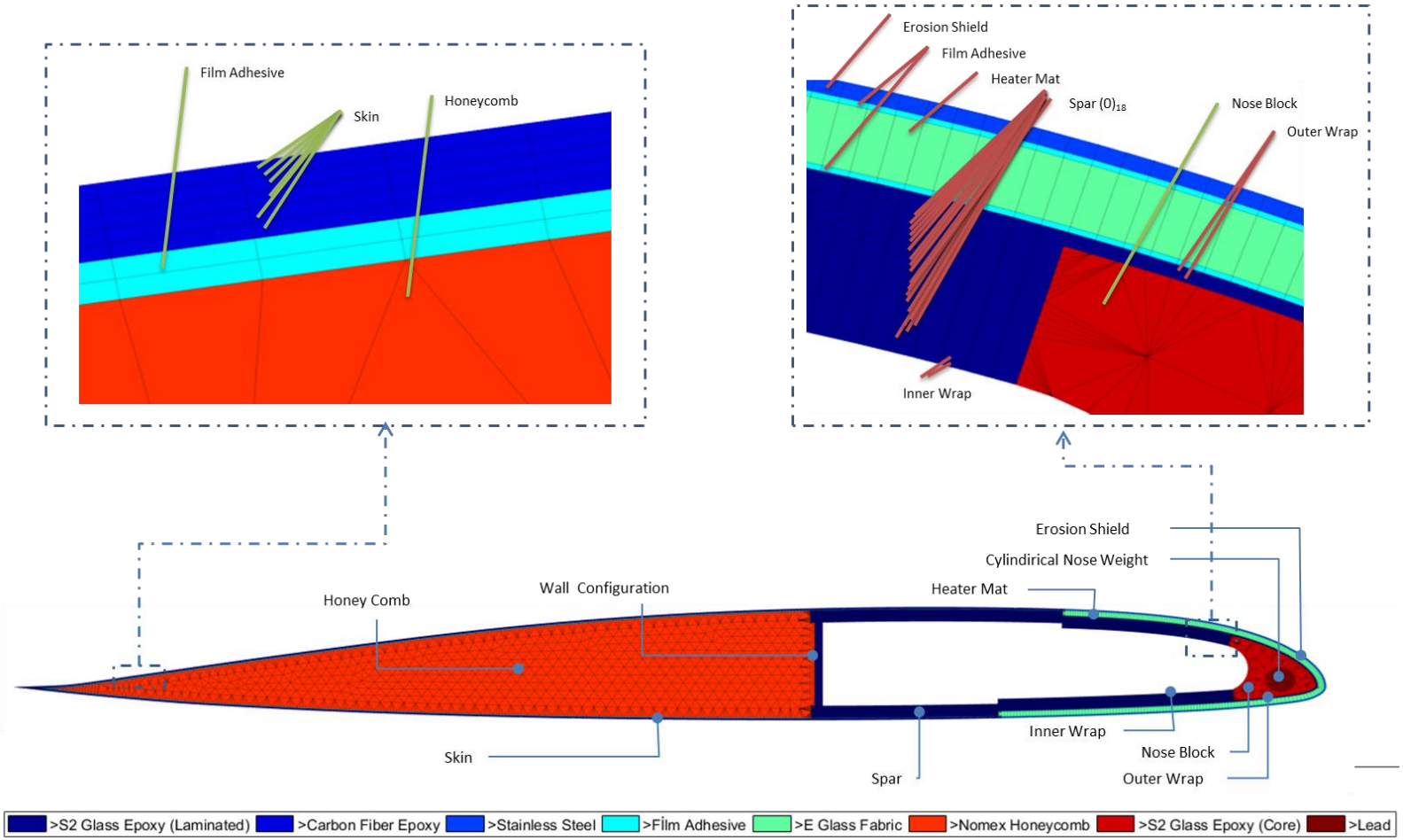

Figure 2 Cross-Section Model of the Functional Region

Blade Modeling

Table 1 Main Design Parameters

Design Parameter Name	Design Parameter Value
Flight Condition	Vacuum
Rotor Type	Articulated Rotor
Number of Blades	5
Hinge Offset	500 mm
Span Length	5900 mm
Rotor Radius	6400 mm
Chord Length of the Functional Region	420 mm

Table 2 Component-Material Table

COMPONENT	MATERIAL	BASELINE DESIGN LAY-UP CONFIGURATION
Spar Straps	S2 Glass Epoxy	$[0]_{18}$
Upper Skin	Carbon Fiber Epoxy	[45/0/-45]
Lower Skin	Carbon Fiber Epoxy	[-45/0/45]
Nose Block	S2 Glass Epoxy	[0]
Inner & Outer Wrap	S2 Glass Epoxy	[45/-45]
Spar Wall	S2 Glass Epoxy	[45/-45]
Erosion Shield	Stainless-Steel	-
Heater Mat.	E Glass Fabric	[45]
Trailing Edge Core	Honeycomb	-
Cylindrical Nose Weight	Lead	-

2.2 Critical Design Constraints

Helicopter rotor blades are high frequency rotating, built-up and composite structures composed of anisotropic and nonhomogeneous materials. The blades are tested for dynamic and strength parameters due to high frequency rotation and various composite

failure modes. The blades must be designed, analyzed and tested considering all possible failure modes, dynamic stability, ground resonance and blade resonance concerns for a flight mature helicopter design. These prominent constraints are called as “critical design constraints”. Critical design constraints have to be narrowed for the preliminary design level optimization of helicopter rotor blades due to the incomplete design stage. In this stage, not only in-flight load spectrum but also failure mode database of the blade is unknown. Moreover, complete helicopter data such as mass of the helicopter body or stiffness and damping parameters of lag dampers and landing gears is supposed to be incomplete for dynamic analysis. However, cross-sectional center positions and blade natural frequencies can be determined. These parameters are only related to components belonging to the rotor kinematic system and the rotor blade design data. After narrowing the critical design constraints, it is necessary to be more conservative about the limitations because at the end of the optimization, the design has to be available for tuning the dismissed critical constraints for the mature design stages Consequently, in this study, critical design constraints are narrowed to the blade natural frequency, sectional-center positions such as shear center, tension center, CG, feathering axis and strength limits for the blade.

In the literature, various methods have been applied for strength concerns in helicopter rotor blade optimization studies. In [17], axial stresses calculated from centrifugal loads and bending loads are checked. Walsh and Chattopadhyay [18] set centrifugal stress calculated from beam analysis as a limit while optimizing the helicopter rotor blade. However, critical centrifugal stress limit is not given by Walsh and Chattopadhyay numerically. Li and coworkers [16] applied Von Mises criterion for isotropic materials and Tsai-Wu criterion for composite materials [19]. Some studies [20] focused on ultimate strain limits in material directions. He and Peters [21] applied fatigue methodology. Besides the literature studies, there exist design and testing advices of aviation authorities for certification of rotorcraft. In Federal Aviation Administration Advisory Circular 29-2C (Certification of Transport Category Rotorcraft) section §29.573, the design considerations are explained for damage tolerance and fatigue evaluation of composite rotorcraft structures [22]. According to

Advisory Circular 29-2C, the maximum allowable design strain level for each full-scale component is established by using the small-scale characterization tests of each composite material. It is also underlined by the Advisory Circular 29-2C that reliability and confidence levels should be considered while attaining maximum allowable design strain values selected because the flaws in the production component may restrict the allowable design strain level to maintain initial level of airworthiness. Design strain limit methodology is also mentioned in the memorandum of FAA for the rotorcraft secondary composite structures [23]. According to to this memorandum, designing the components for strain levels no higher than the limit strain levels is a preferred method for the strength considerations because limit strain levels comprise notch sensitivity, resin microcracking, impact damage, and long term environmental exposure. It is also noted that the values must be validated by the applicants with a strain survey.

Helicopter rotor blades are high frequency vibrating heavy components which are subjected to cyclic loading hence fatigue. Von Mises, Tsai-Wu and Maximum Strain methodologies may not be directly convenient in terms of strength limitations because these methodologies are formulated according to static strength concerns. On the other hand, direct application of fatigue limitations is not possible in the preliminary design stage of the helicopter rotor blade due to incomplete loading data. Moreover, manufacturing defects such as impurities, notch sensitivity, material defects, de-bonding lead to a loss of strength of the materials. It is necessary to obtain loss factors by obtaining sufficient experience about manufacturing stage and testing. Considering the manufacturing defects and fatigue behavior, in the present study maximum strain on global axial system with a conservative reduction is found to be reasonable. In this thesis, maximum strain on global axial system is set as the strength constraint. This methodology is parallel to the limit design strain methodology suggested by FAA [22], [23] and is similar to axial or centrifugal stress constraints used in literature [17], [18] in terms of selected direction of strength limitation.

From the dynamic stability point of view, center of gravity (CG), shear center (SC), neutral axis (NA) and feathering axis (FA) need to be as close as possible to each other.

Increasing the distance between SC and CG leads to aeroelastic instability, a mix of vibratory modes and an increase in pitching moments. In the previous helicopter rotor design and optimization studies [15], [20], [12], [24], [17], [25], [16] the distance between CG and SC is also taken as a design constraint. Furthermore, if the NA and the SC gets closer to the FA, which coincides with aerodynamic center, strain contribution due to the eccentricity of the NA and the SC decreases.

Grandhi [26] reviewed the structural optimization with frequency constraints and pointed out the importance of frequencies for helicopter vibration. For the helicopter rotor blade, blade rotating frequency and its integer multiplies are called as /revs which are critical if they coincide with the blade natural frequencies. Peters and colleagues [17] applied dynamic characteristic optimization to a tilt-rotor blade with blade natural frequency constraints. Except for the first modes, the blade natural frequencies are bounded with 0.3/rev difference. It means that, no natural frequency can be in between $(n \pm 0.3)$/rev where n is a positive integer value. Ganguili and coworkers [27] made a 4/rev hub shear load minimization for 4 bladed hingeless rotor with blade rotating blade natural frequency limitations for the first flap, lag and the torsion modes. He and Peters [21] applied natural frequency placement up to first 9 modes of the helicopter rotor blade while optimizing the blades for combined structural, dynamic and aerodynamic properties. The optimization study [28] is applied to the articulated rotor blades. It is mentioned that first flap and lag modes are disregarded from frequency constraints because they are directly related to rigid body modes [28]. It means that, first flap and first lag mode cannot be tuned by manipulating elastic and mass behavior of the blades.

Fan plot is used to observe whether the blade is in resonance or not. It shows the variations of the natural frequencies of rotating blades versus the rotor speed. A typical fan plot is given in Figure 3 where ω_{ref} is the operational rotor speed, ω is the current rotor speed and ω_n is the natural frequency of the blade for the current rotor speed. Colored lines show the natural frequency variation of the rotor blades with changing rotor speed. Each color symbolizes different vibration mode of the blades. /rev lines are also included in the figure with dashed lines. They are used to show /rev values

(integer multipliers) of any rotor speed. The resonance occurs if natural frequency lines and /rev lines intersects. However, in this thesis, it is necessary to focus only on the vertical ω/ω_{ref} =1 line for the natural frequency constraints, as the blade is designed for the operational speed (ω_{ref}).

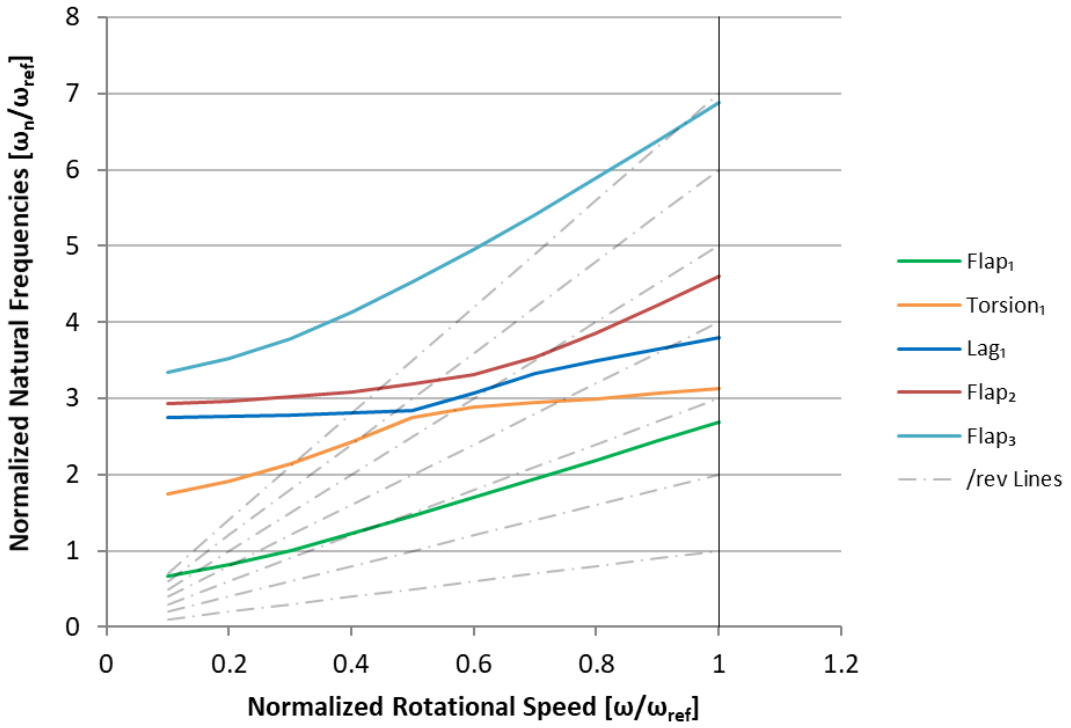

Figure 3 Typical Fan Plot

2.3 Modelling

2.3.1 Theory of Modelling

2.3.1.1 Theory of Elastic Beam

The elastic structure, of which one dimension is much larger than the other two dimensions, is called as beam. Through the history of engineering, beams found many applications in various fields. Most of the structural components of civil engineering constructions are composed of beams. Car axles, shafts, machine linkages and robot arms are the typical examples of beams in mechanical engineering. In aerospace engineering, plane wings, wind turbine, helicopter rotor blade, and jet turbine blades are modelled as beams. The “beam theory” definition starts with idea that the geometric feature of the beam gives an advantage to analyze the deformation behavior. This is achieved by eliminating shorter dimensions for the modelling of beam. However, preserving 3D strain energy of a deforming 3D physical structure when it is implemented as 1D deforming beam model is a challenging task in implementing the “beam theory”. Beam theory provides simple tools for analysis of numerous structures, and it has a significant role in structural analysis [29]. In common use, beam axis refers to the axis parallel to the longer dimension and the cross-section refers to the section of the structure which is normal to the beam axis. Through the history, a wide range of beam theory methods have been developed from very simple to very complex. However, all of them faced with the difficulty of modelling a 3D physical structure in 1D with an acceptable level of accuracy of 3D strain energy conservation.

Euler-Bernoulli beam theory where the formulation is given in [29] is one of the simplest and earliest method. This method is still useful in many engineering applications such as civil engineering beams. Euler-Bernoulli beam theory formulation assumes that the cross-section plane remains plain and normal to the beam axis while

deforming. The beam is assumed to be isotropic. The beam is also assumed to have deformation modes of extension, twist and bending in two directions.

Timoshenko beam theory [30] [31] is used for shear deformable beams. Extension, shear deformations in two transverse directions, twist, and bending in two transverse directions are the fundamental deformation modes in this theory. For the beams with vibrating in a shorter wave-length than its physical length or the beams which are not slender, Timoshenko beam model gives a better deformation solution than the Euler-Bernoulli beam model.

In the isotropic beams with initial twist or in the beams composed of composite materials, deformation couplings occur. Instead of isolated deformation of extension, twist and bending in two different directions, each deformation mode is mostly-like to affect the others. Symmetric 4x4 stiffness matrix takes place due to the coupling effects in addition to diagonal terms of the Euler-Bernoulli beam. This generalized Euler-Bernoulli theory is called as "classical beam theory".

However, for the anisotropic beams and the beams which undergo small-wave length vibration mode, Timoshenko refinement is crucial. This refinement includes shear deformations and the couplings with the other deformation modes. Giavotto [16] developed a cross-section model by using FE to obtain the 6x6 stiffness matrix for a complex geometry and composite section beam. Stiffness matrix is derived from 6 loads (3 forces and 3 moments) related to 3 strains and 3 curvatures. Moreover, model was capable of obtaining 3D stress and strain field on each element of the cross-section. This model is then refined by Borri and Merlini [32].

For the nonlinear problems, Variational Asymptotic Method (VAM) was developed by Berdichevsky [17] [18]. VAM is capable of cross-sectional analysis for classical modelling of nonhomogeneous, anisotropic beams. VAM is based on the simplification of the three-dimensional slender structure into a two-dimensional cross-sectional and a one-dimensional nonlinear beam. Later on, this work is extended by Cesnik & Hodges [4]. Finally, a simple, low time cost modeling and analysis tool has been developed which is called as "Variational Asymptotic Beam Sectional Analysis"

(VABS). VABS uses the variational asymptotic method (VAM) by applying Generalized Timoshenko model [33], Vlasov model [34] and Trapeze effect [35]. The sectional properties (structural properties and inertial properties) are calculated by VABS via the finite element mesh of the cross-section. All the details of the geometry and the material are included in the FE mesh of the cross-section. To predict the global behavior of the slender structure, it is necessary to implement the sectional properties in the one-dimensional nonlinear beam analysis. The global behavior of the one-dimensional beam analysis allows the recovery of the three-dimensional pointwise displacement/strain/stress distribution within the structure [1]. It is to be noted that Vlasov model is not chosen for the helicopter blade optimization because Vlasov model is suitable for thin walled, open-section models. Trapeze effect is also not included since it is more suitable for torsionally soft beams. Timoshenko-like form is preferred since the rotor blade vibrates in small wavelength modes. The generalized Timoshenko formulation of VABS is given in [33] by extending the initial formulation given in [25]. The validation of VABS is done by Yu and colleagues [5]. Various comparisons have been done for VABS-theory of elasticity, VABS-common engineering calculations for shear center locations and VABS-ABAQUS for 3D stress and strain calculations. In [36], more detailed theory of elasticity validation is also done. The output is that VABS requires much lower computational time than 3D FE analysis while conserving the level of accuracy as the 3D FEA.

2.3.2 General Approach for Modelling

In this thesis study, the helicopter blade is modeled as a beam consisting of 2D cross sectional FE model. This model is generated by a combination of an automated core mesher, PreVABS [7] (VABS built-in meshing tool) and the 1D multi body model. Figure 4 shows the beam model description of the blade which is essentially the blade definition used in PreVABS and VABS.

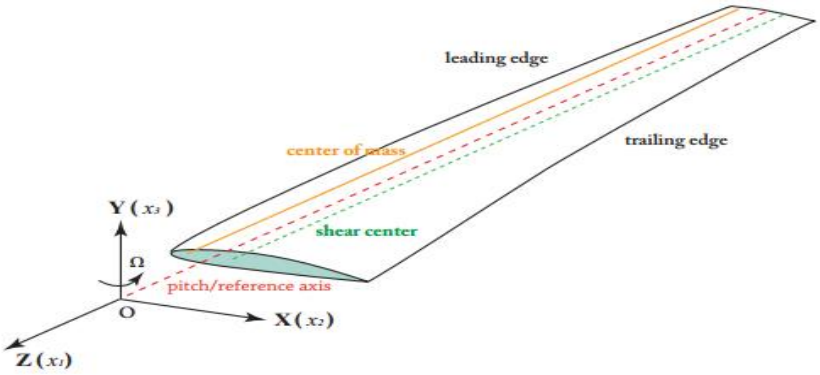

Figure 4 Beam Model Description of the Helicopter Rotor Blade [37]

Cross-sectional properties of the beam blade, such as the neutral axis, shear center, stiffness and mass matrices are calculated by VABS. Stiffness and mass matrix definitions with critical center definitions are given in APPENDIX A. Internal blade loads are obtained from multi body solver Dymore [7]. Internal loads determined by Dymore are then applied to the 2D FE models of the blade sections for strain and for stress calculation in these sections. The general approach for modeling is given as a flow chart in Figure 5.

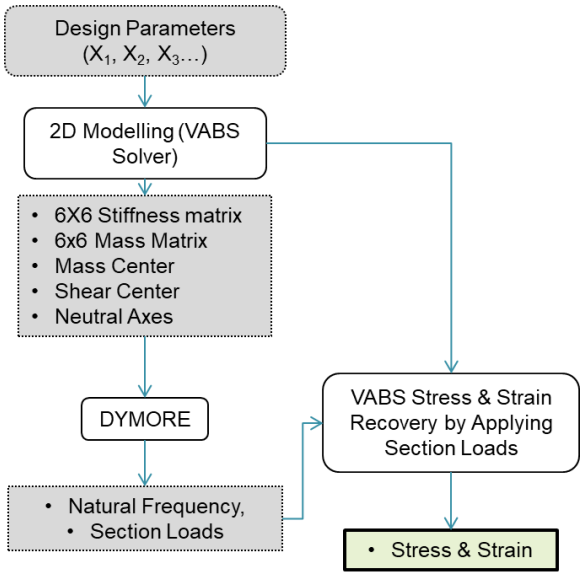

Figure 5 General Approach for Blade Modelling

2.3.3 Reference Axis System & Twist Definition

Aerodynamic Center intersects with the FA. The sectional properties of the blade are defined with respect to the reference axis S_{ref} to be used in Dymore. Components of the reference axis S_{ref} are explained in Table 3.

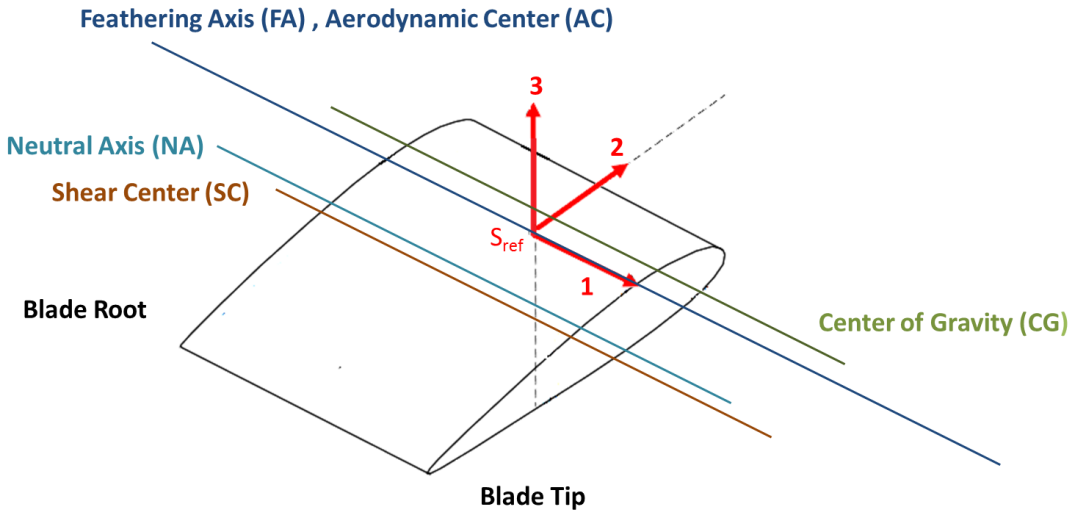

Figure 6 Reference system for blade cross-sectional properties

Table 3 Components of Cross-Section Reference Axis

Origin	Intersection of spanwise station and the FA.
1-direction	Direction towards the blade tip from the blade root coinciding with the FA
2-direction	Parallel to chord line towards leading edge (Chordwise)
3-direction	Towards the upper surface obeying the right-hand rule (Flapwise)

The components of the critical centers are symbolized and given in APPENDIX A. It is to be noted that "2" and "3" vector components of S_{ref} has the same meaning of chordwise and flapwise direction terms respectively. Critical centers used in this thesis

are the center of gravity (CG or mass center), the neutral axes (NA or tension center), and shear center (SC or the elastic axis). x_{m2} is the location of chordwise CG. x_{m3} is the location of flapwise CG. x_{s2} is the location of chordwise SC. x_{s3} is the location of flapwise SC. x_{t2} is the location of chordwise NA. x_{t3} is the location of flapwise NA.

The geometric twist angle (ϕ) is defined by the angle between the vector '2' and the blue line which is parallel to the ground as shown in Figure 7. In nose up position, such as in Figure 7, the sign is positive. The spanwise distribution of ϕ along the blade is given in Figure 8. The blade sectional properties with respect to S_{ref} and the twist distribution are necessary and sufficient to complete the blade model to be used in Dymore.

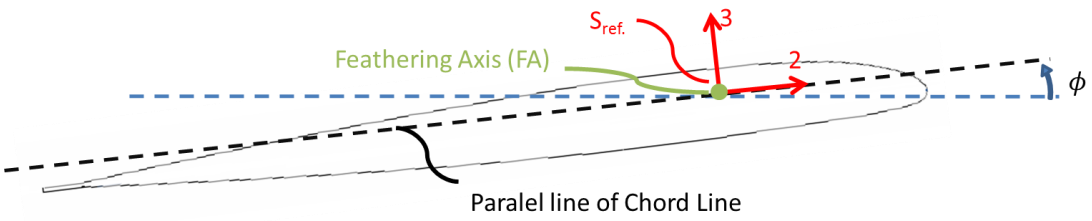

Figure 7 Twist reference

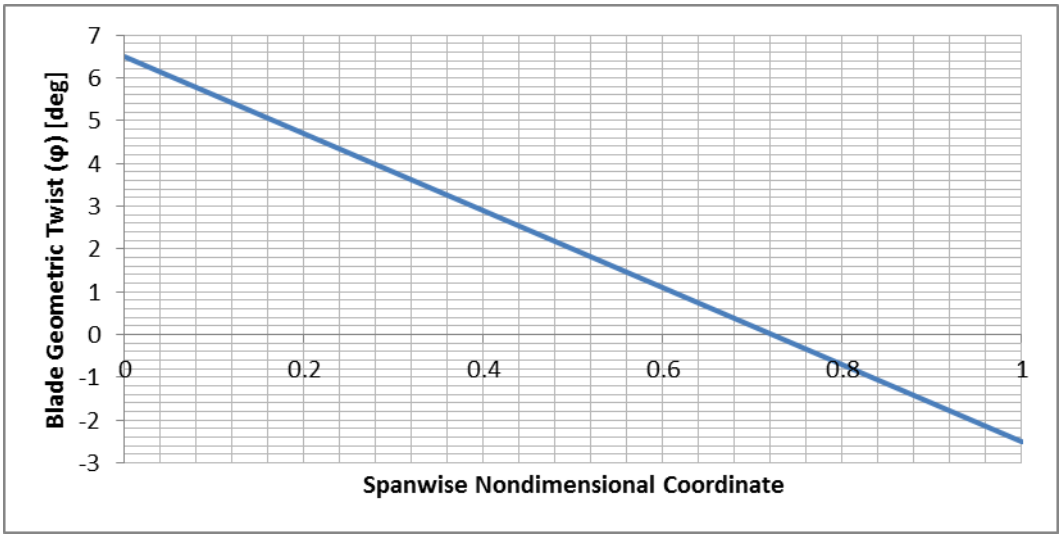

Figure 8 Blade twist distribution

2.3.4 Composite Material Axis System Definition

Finite element modeling of composite materials requires orthotropic material definition with correct orientation. The laminated parts of the rotor blade lay under the aerodynamic surface. Considering the orientation of the laminated parts and the aerodynamic surface geometry, *e* and *y* reference axis systems are defined in Figure 9. Blue and red vectors in Figure 9 symbolize the *e* and the *y* axis systems respectively. For each point of the outer surface of a cross-section, different *e* and *y* axis systems are defined. The y_2 component is always tangent to the outer surface of the cross-section. The direction of y_2 vector follows the outer surfaces of the cross-section in the clockwise direction as given in Figure 9. Material axis system coincides with the *y* axis system if fiber direction is parallel to the FA. For the angle plies, another axis system is defined as the *e* axis system. *y* reference axis system is the parent axis system of the *e* axis system. *e* axis system is on the same plane with the *y* axis system however, e_1 component coincides with the fiber direction while y_1 is parallel to the FA. The angle Θ is defined as ply-orientation and it is equal to the angle between y_2 and e_2. The material directions are finally coupled with the components of the *e* axis system. For example, E_{11}, E_{22} and E_{33} material moduli are defined with respect to the directions e_1,

e_2 and e_3 respectively. The components of the e and y axis systems are clearly explained in Table 4. The densities of materials and the elastic modulus properties with respect to material axis system, e, are collected from the literature for proper aerospace materials. These values and their references are given in APPENDIX B.

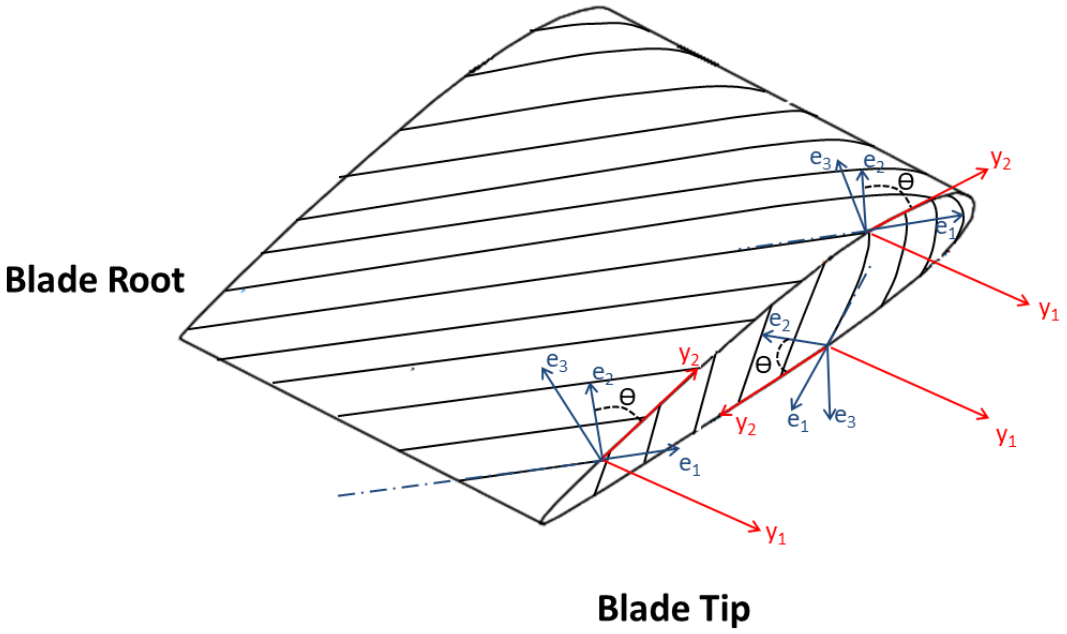

Figure 9 Material Axis Systems

Table 4 Components of the Materials Axis Systems

Origin of *y* & *e*	Any point on the aerodynamic outer surface of the cross-section
$\mathbf{y}_3, \mathbf{e}_3$	Normal to the outer surface
$\mathbf{y}_1$	Direction towards the blade tip from the blade root, parallel to the FA
$\mathbf{y}_2$	Tangent to the outer surface, following the clockwise direction
$\mathbf{e}_1$	Direction coincides with the fiber direction & towards blade tip
$\mathbf{e}_2$	Normal to the fibers obeying right hand rule

2.3.5 2D Cross-Section FE Model of Blade Sections

It is possible to model the helicopter rotor blade cross-section with various commercial products with an interface and simple tools. However, during the optimization procedure, all of the modelling steps have to be automatic for varying design parameters. While constructing the 2D cross-sectional FE model of the blade sections, the following steps are implemented to model automatically without a user interface. The tools used in these steps are chosen by considering their applicability to automation.

2.3.5.1 Preparation of PreVABS Model

For the specialized airfoil profile of the blade with 420 mm chord length, laminated parts of the cross-section are meshed in PreVABS. These parts consist of the erosion shield, dummy heater mat, spar straps, inner and outer wraps, skin, spar web and the film adhesives between neighboring parts.

PreVABS is a computer program which produces high-resolution FE modeling data for VABS. It is a design driven preprocessing program which uses design parameters as CAD geometric data. PreVABS also directly uses both span-wisely and chord-wisely alternating composite laminate definition for the rotor blade and the aircraft wing cross-sections. It can model complicated cross-sectional configurations for a

variety of composite helicopter rotor blades, wind turbine rotor blades and aircraft wind structures. Strikingly, it can also reduce the intensive modelling efforts to generate 3D finite element analysis (FEA) model dramatically. This is important because FEA model is both time consuming and impractical during the preliminary and intermediate design phases [37].

It is possible to model the laminated parts by PreVABS. However, an additional code is necessary to create PreVABS input of the cross-section automatically. The code has to be capable of creating PreVABS input file directly from the design parameters such as wall distance from the leading edge, nose weight radius, skin layup configuration etc. In addition, the code enables parametric modelling of the components. For example, when spar web is moved toward the trailing edge, spar straps and inner-outer wraps enlarge toward trailing edge so that the D-Spar shape is conserved. By this code it becomes possible to automate the cross-section analysis for varying design inputs.

A necessary input for the automation is defined as the relative mesh size (mesh width / mesh height). PreVABS manual [37], suggests a relative mesh size between 3.0 to 8.0. To decrease time cost, maximum relative mesh size is aimed as maximum relative mesh size provides sufficient accuracy. This is done by considering the mesh size convergence. From the mesh size convergence study performed and the suggestions of the PreVABS manual, relative mesh size is taken as 6.0. The details of the study are given in section 2.3.6.

For the meshing of laminated parts by PreVABS; airfoil surface geometry, web definitions including location and angle data, material data and the cross-sectional lamination definition are the necessary inputs for modelling. Although airfoil twist angle is also a necessary input for the modelling, zero twist is utilized in this section for modelling. This is done because constant twist is applied during the multibody solution of the blade in Dymore. Airfoil surface geometry is obtained from a text input. This text input possesses the 2D coordinates of the intersecting points with the airfoil surface. Because D-Spar type is used in this work, a single web perpendicular to the chord and a corresponding single location input are present. These define the web

geometry. The material properties are defined as 3D orthotropic material as mentioned in Section 2.3.4.

The preparation of cross-sectional laminate definitions the key point of automation. The PreVABS inputs are composed of upper surface and lower surface segments. These are necessary to define the chordwise changes in laminates. An example of the segmented definition of a typical blade, which is given in the PreVABS manual, is presented in Figure 10.

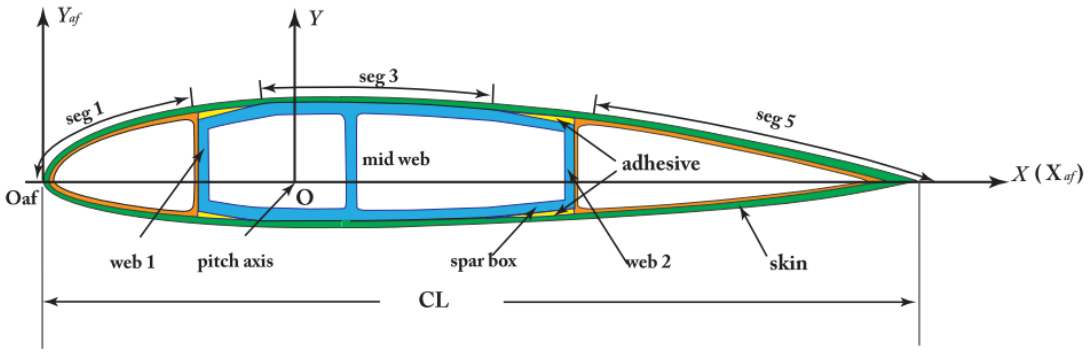

Figure 10 Sketch of a typical blade cross-section [37]

In this study, the cross-section is composed of 4 upper and 4 lower segments. Any changes in the design parameters possibly cause a group of change in various segments in the laminate definition. The segments of the basic design configuration and the corresponding subcomponents of each segment are given in Figure 11. The change of number of spar plies can be examined to explain the relation between design parameters and the segments. The spar is composed of spar straps, inner-outer wraps, spar wall and nose block. Spar straps, nose block and spar wall are covered by inner and outer wraps. The number of spar plies term corresponds to the number of spar strap plies because the spar strap is the main layed-up component of the spar. For instance, A change in the number of plies at the spar requires an alteration in the lamination scheme of 4 different segments in total. There exist Segment 2 and Segment

3 on the outer surface and on the lower surface affected from this change as it can be seen from Figure 11.

An example of PreVABS input file is given in APPENDIX C.

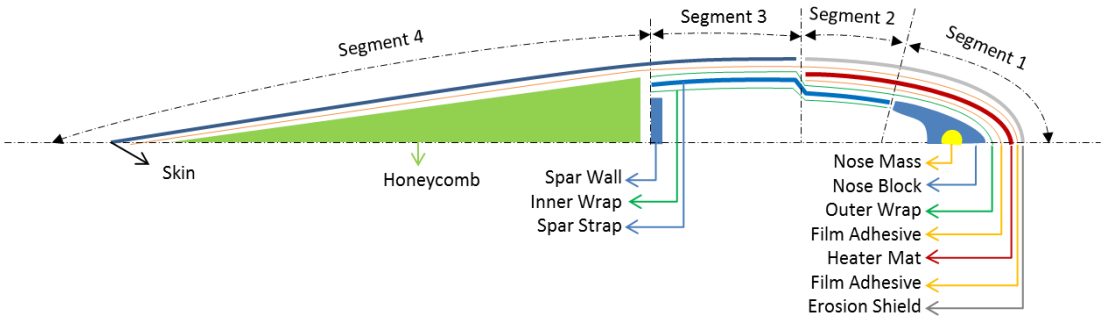

Figure 11 Segment-Subcomponent Relation Description Schema of Baseline Blade

2.3.5.2 Core Mesh Generation

Nose block, nose weight and honeycomb in the trailing edge are meshed. This is done by the combination of Mesh2D, an open source 2D mesh generator, and an automatic mesh attachment code generated by MATLAB [38]. The code attaches the core meshes generated to the PreVABS mesh. Hence, this attachment code enables combining the mesh generated for the honeycomb core, the nose block and the cylindrical nose weight with the PreVABS mesh. Figure 12 shows the trailing edge core and nose block meshes generated.

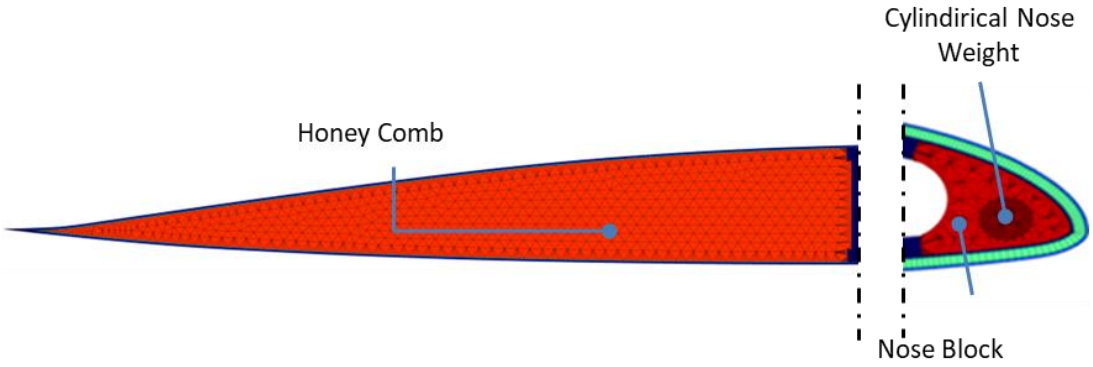

Figure 12 Core Meshes of Honeycomb, Nose Block and the Cylindrical Nose Weight

In order to mesh the core subcomponents, obtaining boundary nodes and the neighboring node connectivity of the boundary is necessary for the 2D open source mesher to work. Following steps are applied during the detection of the boundary nodes and the connectivity information of the honeycomb, nose block and cylindrical nose weight meshed with the neighboring meshes.

First, the boundary nodes of the laminated parts are detected. To detect the boundary nodes, connectivity arrays of each element are checked. By applying an algorithm, inner and outer boundaries are detected. This algorithm runs by searching and checking the element-node-neighbor relation. Any selected inner node in the FE model is supposed to have the same number of neighbor nodes as the number of elements sharing the selected node. As it is illustrated in Figure 13, Node A is not a boundary node. Node A has 4 neighbor nodes and Node A is shared by 4 elements. However, Node B is a boundary node. Node B has 4 neighbor nodes and Node B is shared by 3 elements.

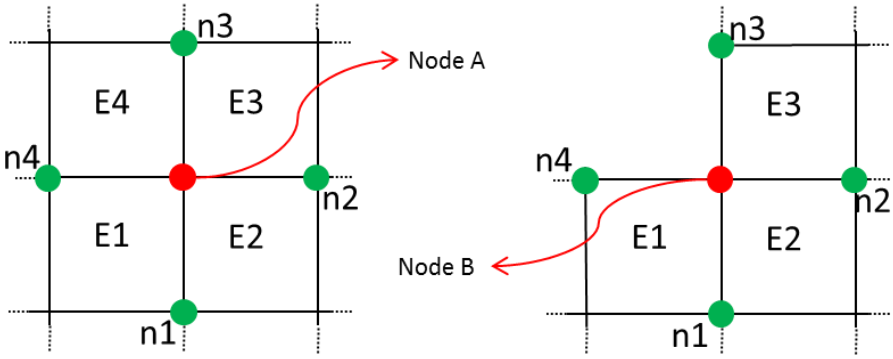

Figure 13 Neighbor Node- Parent Element Relation

Since D-Spar type spar is used in this study, as shown in Figure 14, there exists 3 boundaries which are "outer boundary", "leading edge side inner boundary" and "trailing edge side inner boundary".

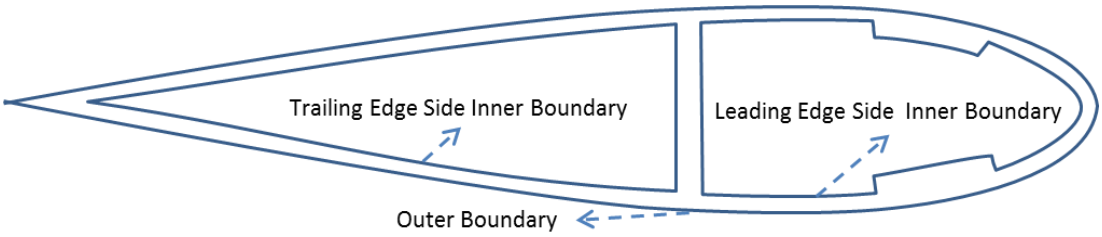

Figure 14 Inner and Outer Boundaries

From the relative positions of geometric centers and the boundary length comparisons of the boundaries, boundaries are identified as outer boundary, trailing edge side inner boundary and leading-edge side inner boundary.

Honeycomb is directly meshed by using the trailing edge side inner boundary.

To mesh the nose block, it is necessary to detect the intersection point of spar straps and the nose block on the leading-edge side inner boundary, one in the upper surface and one in the lower surface. Since the approximate positions of these points are known from the design inputs, corner nodes can be detected by an algorithm. These

nodes, one being in the upper surface and one in the lower surface are completed by an arc. In addition to the positions of these two points, tangency constraint is given to the arc at the upper boundary corner to define a smooth arc. The tangency vector is defined by the angle between Tangency Reference Point and Upper Boundary Corner. Figure 15 shows the construction diagram of nose block boundary nodes on the arc. Hence, the boundary nodes of nose block are assigned and automatically updated for any varying design parameter by the algorithm.

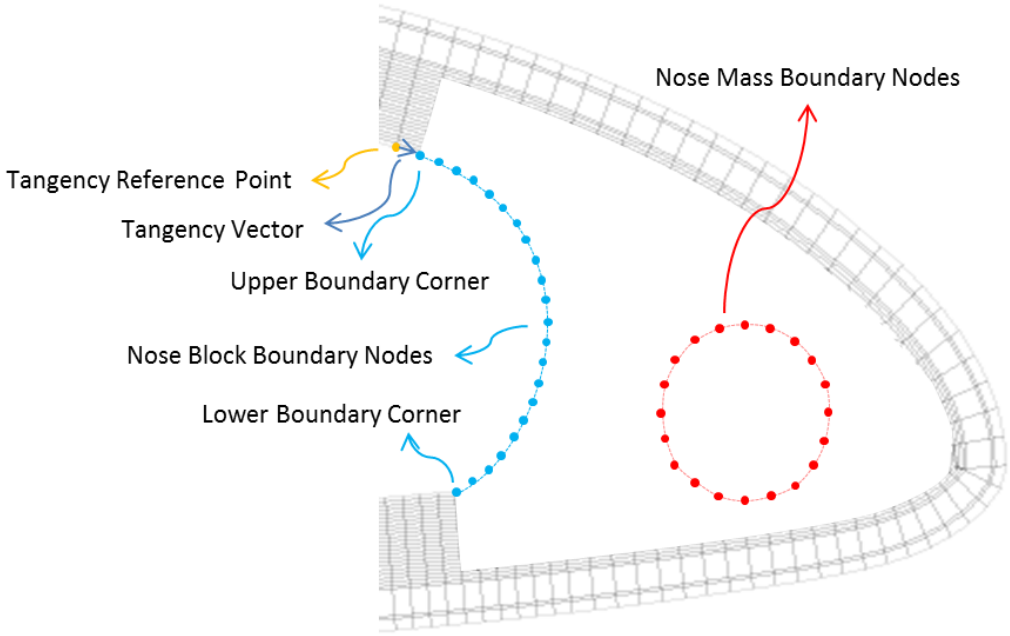

Figure 15 Nose Block and Nose Mass Additional Mesh Seeds

The periphery of the cylindrical nose weight is defined from the design input data. For the nose weight, the design input data is the center position and the radius of the nose weight. After adding mesh seeds to the periphery of the circular nose weight, the seeds are used as the inner boundary of the nose block and as the outer boundary of the cylindrical nose weight.

Finally, nose block is defined and meshed between the arc generated, Leading Edge Side Inner Boundary and the nose mass periphery. Nose mass is defined by using only nose mass periphery nodes. Figure 16 shows the nose block and nose mass mesh.

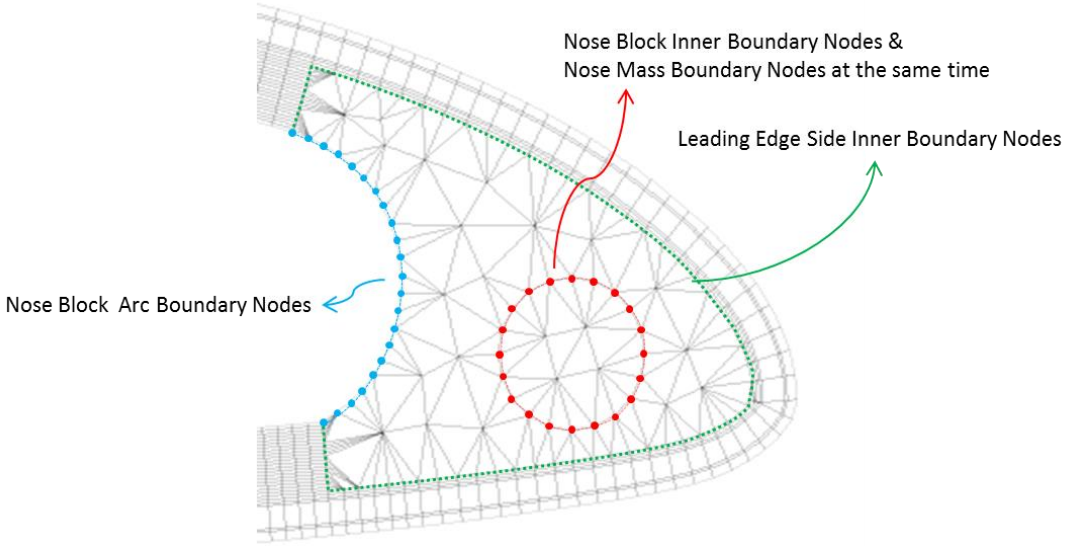

Figure 16 Nose Block and Nose Mass Mesh Boundaries

2.3.5.3 VABS Analysis

After combining the PreVABS and the core meshes in VABS format, VABS analysis is performed to determine the beam sectional properties. The sectional properties used in this thesis are the CG, SC and NA positions with respect to the FA, 6x6 stiffness and 6x6 mass matrices. The beam sectional properties are then used in the multi body solver Dymore and the cross-sectional internal loads are determined. The cross-sectional loads determined by the multi body code are then applied to VABS for strain/stress recovery.

An example of VABS input file is given in APPENDIX D.

2.3.6 Mesh Convergence Study of 2D Cross-Section Analysis

Considering the FE model solutions and the optimization studies using these models, decreasing solution time of each FE model is essential for the governing optimization studies. Increasing the mesh size of the FE model is an effective method to decrease the FE solution time. However, as the mesh becomes coarser, the error increases. Hence, increasing the mesh size decreases solution time but increases the error at the same time. Furthermore, in this study, PreVABS and the developed automatic mesher code did not to work properly sometimes because of too fine or too coarse meshes. A proper mesh size selection becomes crucial because of the behavior of FE models and the meshing problems.

Laminated parts of composite cross-section are modeled by PreVABS as mid-step of FE modeling. Element thicknesses are equal ply thickness by PreVABS syntax. Hence, manipulating element thickness is not possible because ply thickness is defined by the composite materials. Mesh width is on the same direction with outer surfaces and can be altered. Therefore, only by changing Relative Mesh Size (*RMS*, mesh width/mesh thickness), PreVABS can change the mesh size. In Figure 17, the study to select proper *RMS* is shown. In this optimization study, maximum global axial cross-section strain, 6x6 stiffness matrix, 6x6 mass matrix, SC, CG and NA are used as cross-section analysis outputs. The symbols used for 6x6 stiffness matrix, 6x6 mass matrix and the locations of SC, CG and NA are explained in APPENDIX A. However, all the outputs are not visualized. The change of ineffective outputs by *RMS* are omitted in Figure 17 since those are supposed to create a complex understanding. Furthermore, normalized outputs are used to create a simple and clear understanding. The figures of the outputs are gathered in a single figure by normalizing the outputs. Many trials showed that FE model having *RMS* smaller than 5 mostly cannot give a solution. “5” is taken as minimum possible *RMS* and the outputs are considered as correct values. The normalized outputs are calculated by the division of any output at current *RMS* by the same output at *RMS*=5 and they are symbolized as *Output*/*Output_ref*. By this way, different types of outputs can be seen in the same figure and the proximity to the

correct outputs. Moreover, the solution time of FE model for the given *RMS* is shown in the secondary y axis of the figure.

The proper *RMS* is taken as 6 for the cross-section analysis employed in this thesis. As it can be seen in Figure 17, at the point where *RMS*=6 the outputs have less than 0.01% error with respect to the solution obtained for *RMS*=5. Until the *RMS* value of 7, there is no significant change in the solution time while the error becomes twice. On the other hand, by selecting *RMS* value from *RMS*=6 to *RMS*=5, solution time jumps from 45 seconds to 62 seconds.

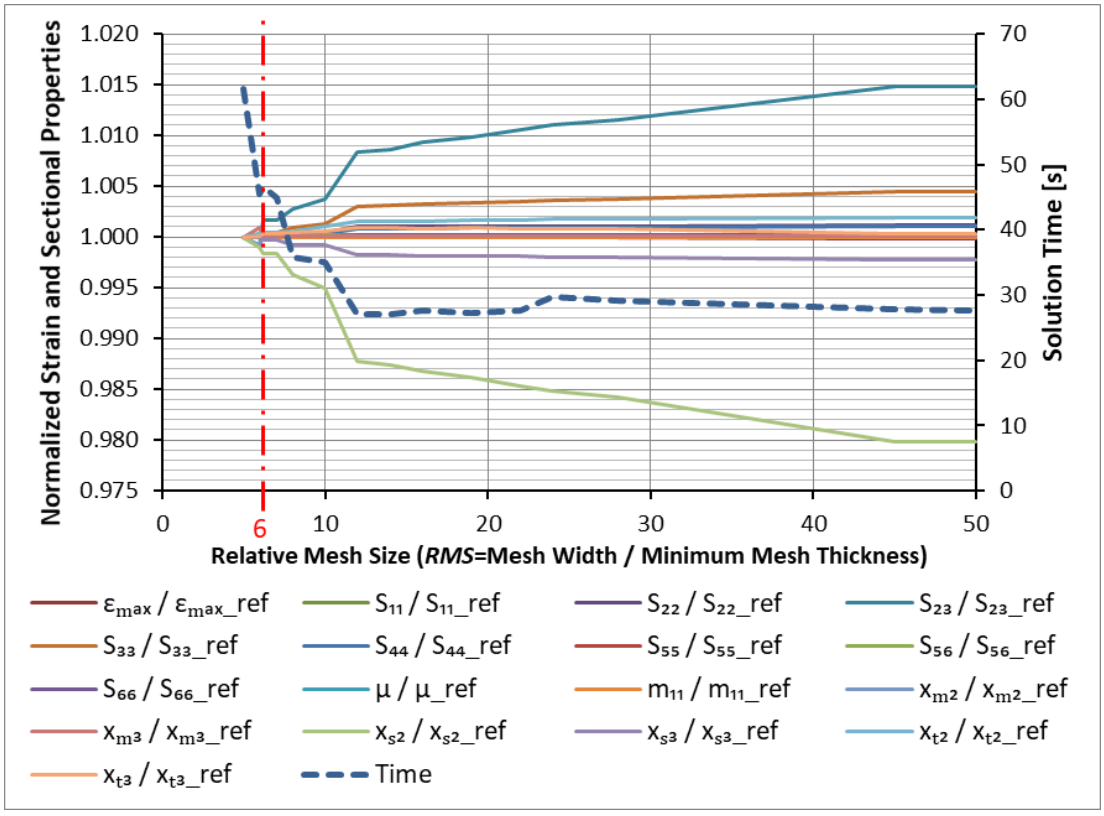

Figure 17 *RMS* Selection Study for Cross-Section Analysis

2.3.7 Simplified Multi-Body Model of Rotor and 1D Beam Blade FE Model

Dymore is utilized as the nonlinear multi body solver. The spanwise loads and natural frequencies for the baseline design and optimized designs are calculated by Dymore. A giant helicopter body data and rotor data is necessary to create a real helicopter model with body weight, inertia, aerodynamic models, mass and stiffness properties of every single rotor components etc. Furthermore, even if each component of the helicopter and the aerodynamic model is complete and correct, it is still difficult to model loads to match the flight loads. However, for an optimization study which covers the preliminary design phase of the rotor blade, the model can be simplified as done in this thesis study. The centrifugal and inertial loads can be easily calculated separately from the aerodynamic loads, the helicopter body and component data of the rotor. Moreover, the highest load contribution for a helicopter rotor blade is due to the centrifugal load because of the high-speed rotation of the helicopter blade. In addition, the accuracy of obtaining centrifugal and inertial loads from the FE modelling is quite acceptable with the application of tools used in this thesis. Considering all of the benefits of model simplification, the model is simplified as shown in Figure 18. Aerodynamic loads are not considered to see the effect of centrifugal loads only. This model is sufficient to obtain blade natural frequencies. It is to be noted that the load contribution of aerodynamics, helicopter body, maneuvers and other contributors are taken into account by magnifying centrifugal loads for the maximum strain check. The magnification method and the constants are given in Calculation of the Blade Loads section.

Articulated rotor with 5 blades is modeled with the blades having 500 mm hinge offset and 5900 mm span length. The operation speed of the rotor is taken as 5 Hz in the counterclockwise direction when viewed from the top. A constant acceleration is defined at the rotor rotation center in order to rotate the blades and obtain a smooth convergence of the model at the operation speed. Up to reaching the constant 5 Hz angular velocity, 11 time steps are defined starting from 0 Hz. As it can be seen from Figure 18, 5 blades are connected to hub with universal joints. Pitching motion at the

root is not allowed as it is constraint by universal joints. The functional region of the helicopter blade is assumed to start at the root. 1-D elastic beam blade is modeled with the elements having four nodes (cubic shape functions are used.). To obtain an appropriate mesh size, a proper mesh selection study is done which is given in the following section. The number of 20 nodes are found reasonable to use in 1D Dymore beam model from this study. Finally, 6x6 stiffness, 6x6 mass properties and the SC, NA and CG positions are assigned to the blades to complete and solve the multi body model.

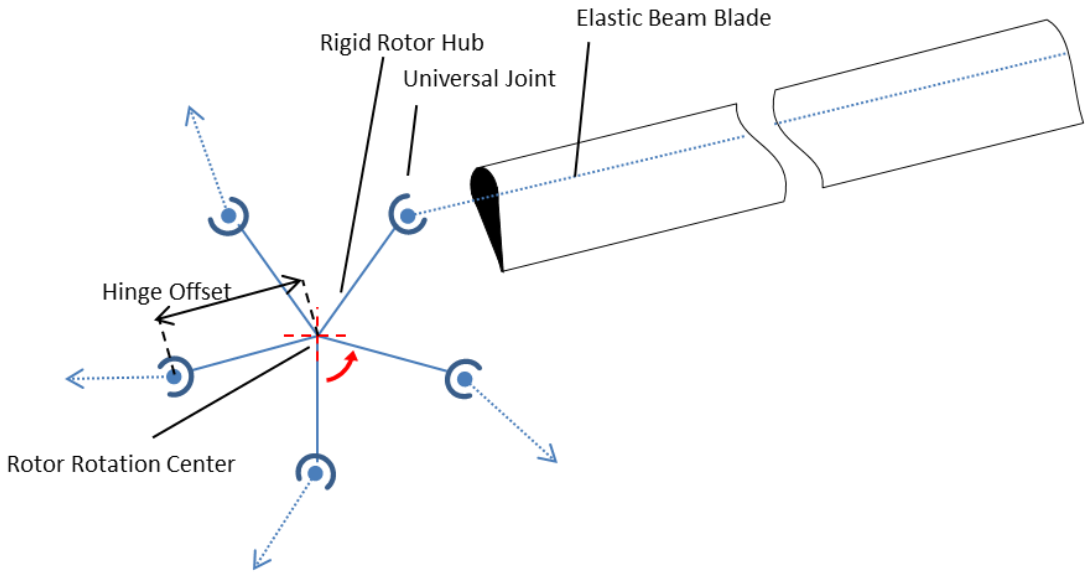

Figure 18 Multi Body Model of the Rotor

2.3.8 Mesh Convergence Study of the 1D Beam Blade Analysis

Another mesh convergence study has been done for 1-D beam analysis which is similar to the convergence study of 2D cross-section analysis explained in Section 2.3.6. 1-D beam analysis is also an element of Dymore multibody model. Solution time and the error of outputs are important in the beam blade analysis as in the cross-section analysis. However, Dymore model is simpler than cross-section model for the mesh

complexity, automation and compact modeling concerns. The Dymore solution outputs converge by varying mesh size. It is clear to see this convergence due to simplicity and compact code behavior in Figure 19. Since the length of beam blade is constant, the number of nodes seeded on constant length beam is inversely proportional to mesh size. For the mesh size selection study, the number of nodes (#N) is used to determine mesh size. The normalized load outputs and the solution time of load outputs are compared for varying node number in Figure 19. Six load components, 3 forces and 3 moments, are calculated with respect to S_{ref} for the baseline model. S_{ref} is the cross-sectional reference axis system where the origin is the FA, "1" direction is towards outboard of the blade, "2" direction is parallel to the chord line towards leading edge and "3" direction is towards the upper surface satisfying the right-hand rule. Hence, cross-sections are modeled without twist. The detailed definition of S_{ref} is given in Section 2.3.3. Furthermore, normalized load outputs are used to create a simple and clear understanding. In the study, #N differs from 5 to 50. The best converged results and minimum mesh size are occur at #N=50 in Figure 19. Therefore, the load outputs can be assumed as correct when #N= 50. The normalized outputs are calculated by the division of any output at the current #N by the same output at #N=50. These are symbolized as Output/Output_ref. Hence, different types of outputs and their proximity to correct output can be seen in the same figure. Moreover, the solution time of FE model for the given #N is shown in the secondary y axis of the figure.

At the end of the study, 20 numbers of nodes are found to be appropriate. The error of outputs when #N=20 are calculated to be less than 0.5% with respect to the results obtained when #N=50. Increasing the number of nodes increases solution time considerably as it can be seen from Figure 19.

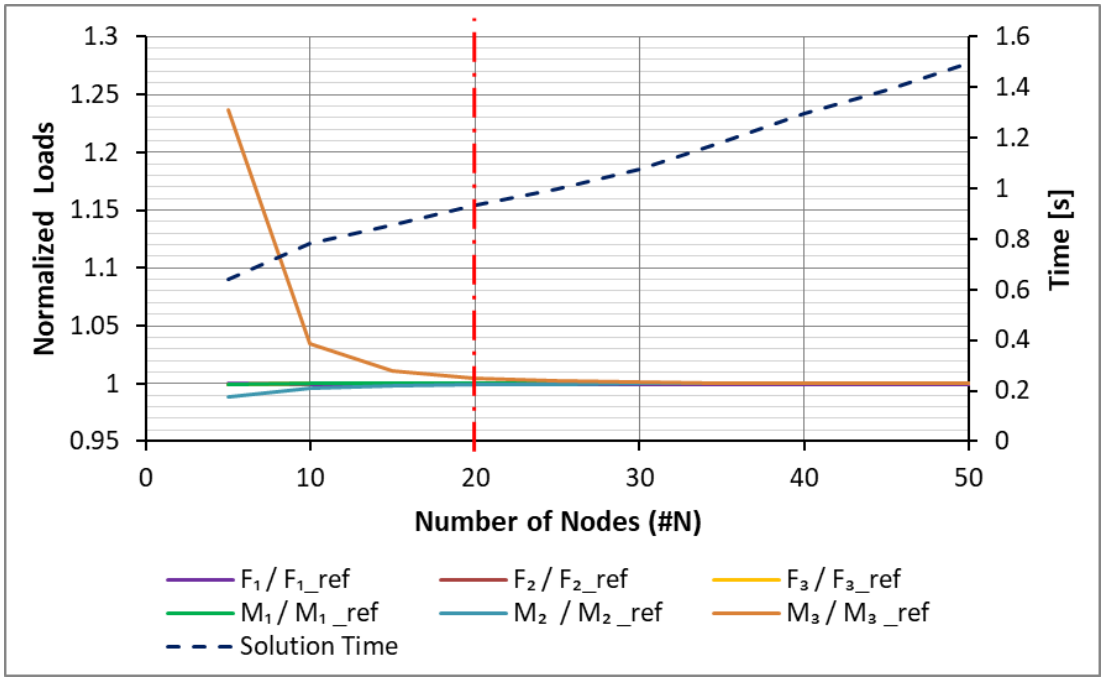

Figure 19 Mesh Convergence Study for the Beam Blade

CHAPTER 3

OPTIMIZATION OF THE HELICOPTER ROTOR BLADE

3.1 Optimization Approach

In this study, a stepwise optimization approach is used instead of a general approach for optimization in order to decrease cost of optimization. These steps are:

- Step 1: Cross-Section Optimization (CSO)
- Step 2: Natural Frequency Tuning

The combination of Step 1 and 2 forms the Full Blade Optimization (FBO).

In detail, weight minimization is aimed by searching optimum cross-section design variables. CSO is performed under strength and critical sectional center constraints. The initial sectional blade loads, calculated by Dymore are kept constant and they are not updated in any design iteration during the first step of the optimization process. Consequently, in the first step optimization, multi body solver is used only once for the creating baseline loads.

In the second step of the optimization, three processes are performed which are the natural frequency constraint check, the natural frequency tuning and the load calculation processes. For the natural frequency tuning, lumped mass is added to the blade model at the cross-sectional CG location while the spanwise location of the added lumped mass is chosen according to the peak points of the mode shapes. Mode shapes are obtained from the multi-body simulation which is performed by Dymore. For the natural frequency tuning, 1D lumped mass is added to the blade by assuming it has only spanwise length and no cross-sectional dimension. Therefore, the cross-section model/models are not manipulated, only the cross-sectional analysis outputs are manipulated. Following the natural frequency tuning, the sectional blade loads are

also calculated by the same tool. And then, first step of the optimization is performed again by keeping the sectional loads as constant in any design iteration of the optimization process. Load calculation, blade tuning and optimization cycle is repeated until the sectional loads do not change within a prescribed tolerance to complete Full Blade Optimization (FBO).

Figure 20 shows the flow chart of the optimization process used in FBO including CSO.

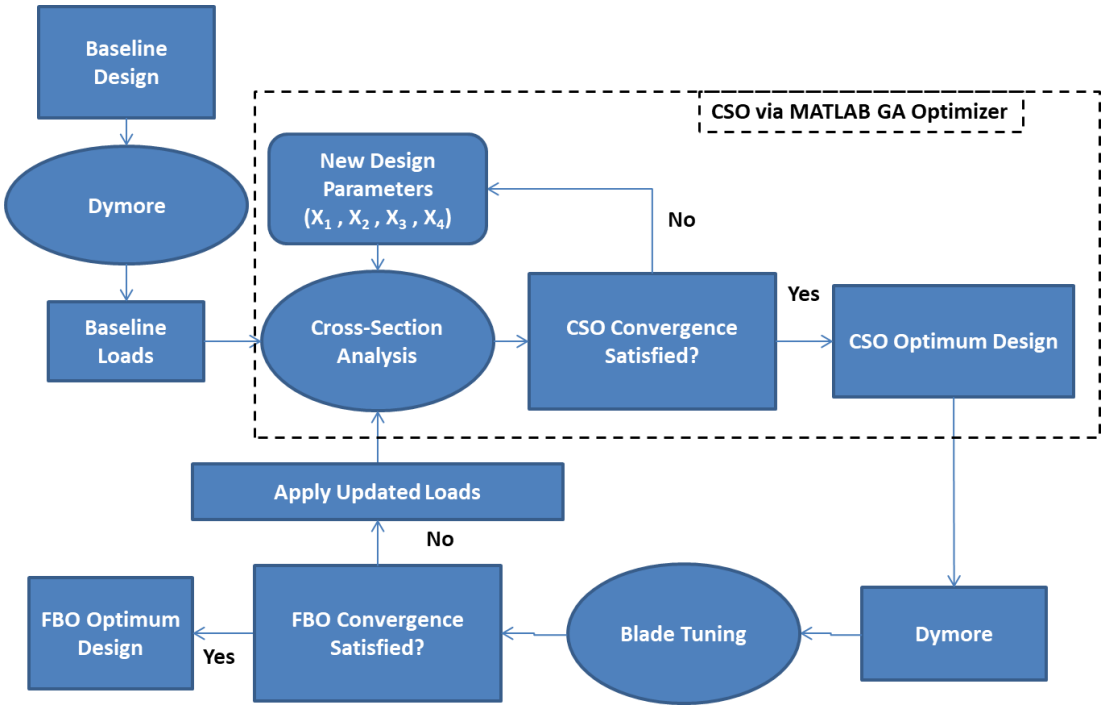

Figure 20 Optimization Flow Chart

3.2 Design Variables

In the present study, genetic algorithm techniques are used for the optimization with the objective of minimizing the total weight of the functional region. Design variables of the optimization which are shown in Figure 21 and Figure 22, are:

- X_1: Wall distance from the leading edge
- X_2: Nose weight radius
- X_3: Number of 0-degree plies in the D spar after the drop-off (integer variable)
- X_4: Spanwise ply drop-off position of the spar plies

It is to be noted that, 0-degree ply number of the spar before drop-off position is taken as 18 which is constant as in the baseline design. Hence, X_3 is a variable which is applicable after the drop-off position.

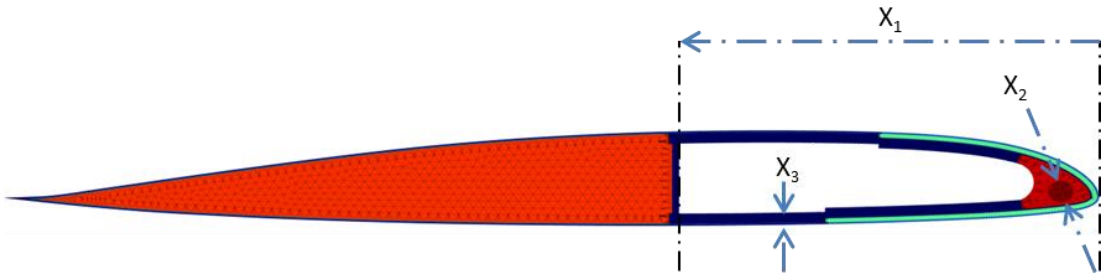

Figure 21 Design Variables (X_1, X_2 and X_3)

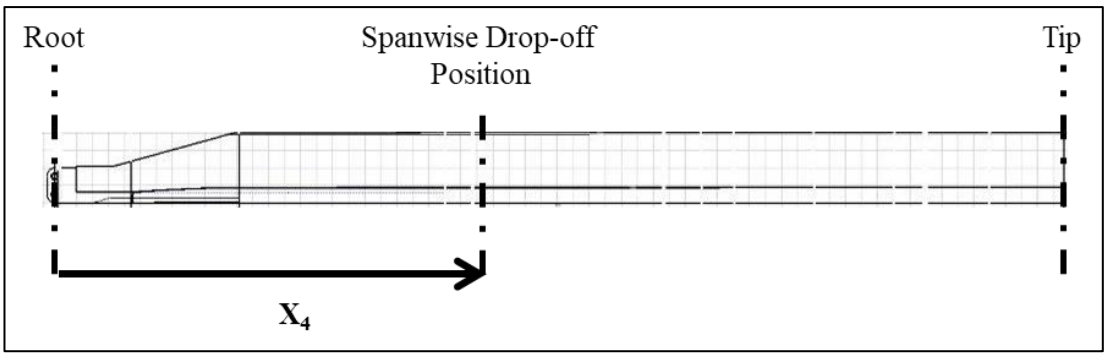

Figure 22 Design Variables (X_4)

3.3 Cross-Section Optimization (CSO)

3.3.1 Genetic Algorithm (GA)

Genetic algorithm (GA) is an optimization and search technique that mimics the principles of genetics and natural selection. GA allows a population of potential solutions to evolve to a state that maximizes the "fitness" by applying the principal of survival of the fittest. The process of selecting individuals in proportion to their level of fitness in the problem domain and breeding them together creates a new set of approximations at each generation. In order to generate and select individuals and update the population, the operators of natural genetics are used. Utilizing the operators of genetic algorithm, individuals of the evolved population are better suited to their environment than the individuals that they were created from.

In this thesis, Matlab GA toolbox [39] is used due to its high-fidelity and integer variable capability. In the present study, design variables include not only continuous but also integer variables. The number of spar plies is the integer variable. The wall distance from leading edge, nose weight radius and spanwise ply drop-off position of the spar plies are the continuous variables. Mixed Integer capability of Matlab allows one to use both integer and continuous design variables in a GA based optimization problem. The steps of GA are given in Figure 23. The effects of mixed integer optimization on these steps are also explained. The steps are also summarized in the Matlab GA toolbox documentation [39], in Matlab GA User's Guide [40] and in Ahn, 2006 [41].

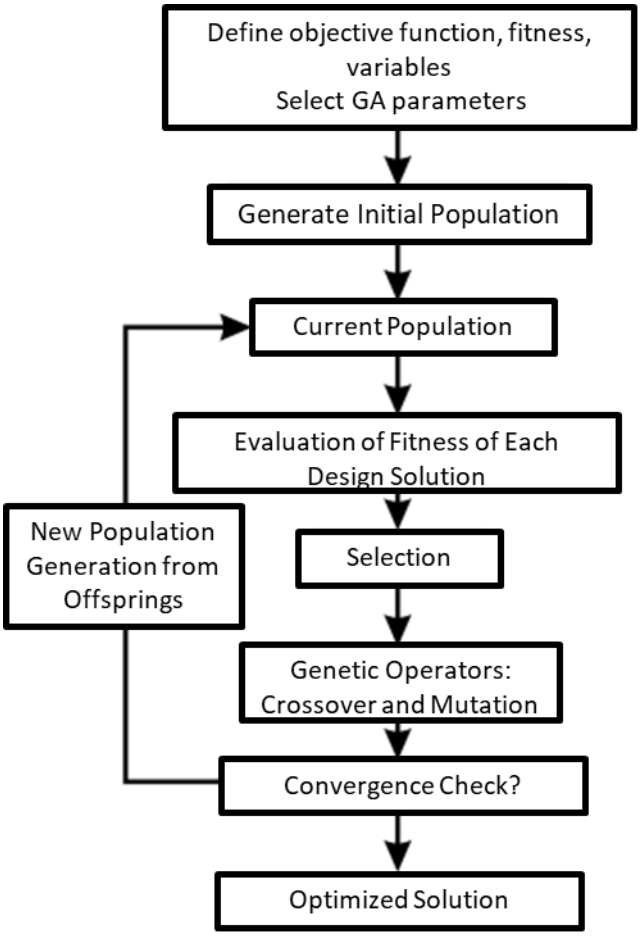

Figure 23 Flowchart of a Typical GA

3.3.1.1 Definition of Genes, Chromosomes, Encoding and Decoding

In GA, design variables are represented as encoded versions instead of the actual values of design variables. The coded version of a variable is called substring. The chromosome refers to a string. It is composed of substrings mapped from all of the design variables in the problem domain. There are different ways of encoding such as binary, ternary, integer, real-valued etc. Binary coding is the most common way of encoding the design variables. The chromosomes are composed of 1's and 0's in binary coding and the bits are called as genes. In the example below, the chromosome structure of a problem with two variables is represented where each chromosome is composed of 4 bits.

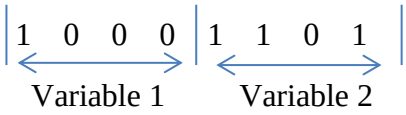

The number of bits describes the number of possible combination of each variable. If m bits are used, there are 2^m possible combinations for a continuous variable. These possible combinations refer to a discrete set between upper and lower limit of each variable. The number of bits used to define each variable can be increased to search the optimum with a better variable precision as the algorithm runs with a discrete set.

Encoding is the process of converting the design variable to a binary substring while decoding is the reverse. Encoding is only necessary for the initiation of the population. Encoded and decoded chromosomes are used in different steps of the GA procedure.

In real-valued coding of chromosomes, real values of the variables are directly used as a double vector which is an array composed of floating numbers. Encoding and decoding is not necessary as real values are the genes of the chromosomes. Integer variables can also be used with their real values as floating points. Moreover, real-values of continuous and integer variables can be used together. The combined version of continuous and integer variables used in optimization problems is called as Mixed-Integer problems by the Matlab definition. An example of real-valued chromosome with 4 design variables and 7-digit precision (Matlab default) is given in Figure 24. It is to be noted that, GA operators of binary coding and real-valued coding for mixed-integer optimization problems also differ. In this thesis, real-valued chromosomes are used because Matlab only provides them for the mixed-integer type optimization problems due to efficiency. Furthermore, discrete feature of binary values leads the loss of precision.

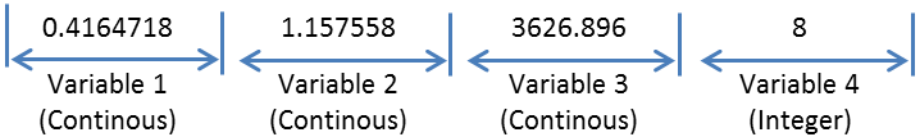

Figure 24 Real-valued Coding

3.3.1.2 Population Representation and Initialization

The set of possible solutions are called population. Individuals of populations are represented with chromosomes. A population composed of number of *i* individuals (or chromosomes) having number of *v* variables each composed of *b* bits are shown in Figure 25. In order to create a simple visualization and understanding, *b* is set as 5.

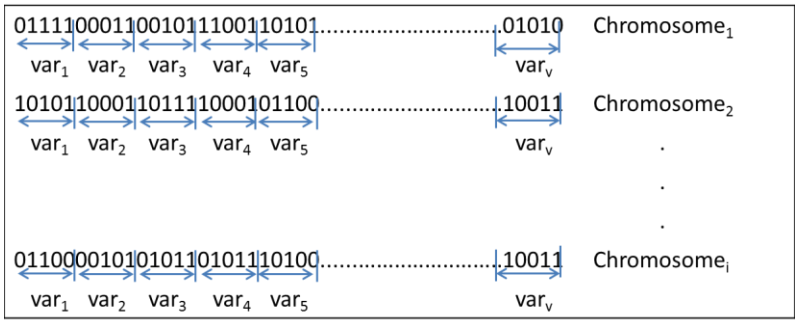

Figure 25 Representation of Binary Coded Population in GA

In mixed-integer problems, chromosomes have the length of number of total variables. It is not necessary to define a substring length. In Figure 26, representation of a mixed-integer problem population is given. The size of the population is *i* and the number of variables is *v*.

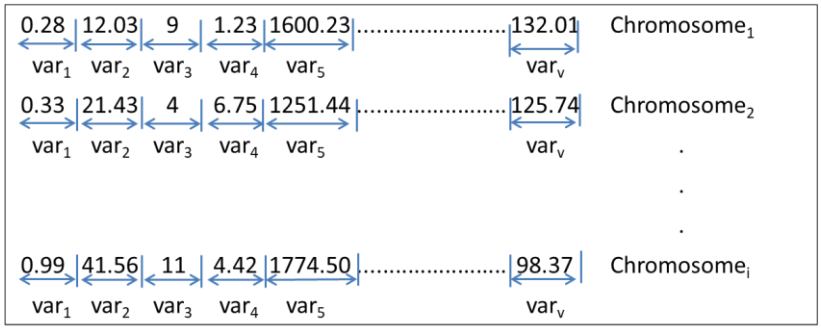

Figure 26 Representation of Real-Value Coded Population in GA

Population is renewed at every cycle of the optimization when the termination criterion is met. New individuals are produced from parent chromosomes which are the new individuals of the previous cycle. In each cycle, after the new individuals are subjected to the steps of the optimization, they become the parent chromosomes.

Typically, a population is composed of between 30 to 100 individuals. In this thesis, the number of individuals in the population is set as 70. Since cross-sectional FE analysis completely automated and not possible to correct manually, the meshing can fail in some specific conditions. For example, PreVABS rarely fails and gives no outputs when its inner nodes of upper and lower surface laminates around trailing edge intersects with each other. Hence, each individual in the population may not give a result. This possibility of unsolved individuals and the number of variables are taken into consideration when deciding on a population of this size. The chromosomes have the length of 4 real-valued vector and composed of continuous and integer genes where an example is given in figure cup.

Figure 27 Real-Valued Chromosome Example Used in CSO

3.3.1.3 Objective Function and Evaluation of the Fitness

As the concept of survival of the fittest is used in GA, it is necessary to define the "fitness" of each individual in the population for the problem of interest. "Fitness" is the quality of the individual with respect to overall population. The formulation to calculate blade weight is called the weight function f in this thesis. If the study were unconstrained optimization, the weight function itself would assess how good a solution an individual provides. However, in this thesis, the optimization problem has

a number of constraints. The design becomes infeasible when the constraint bounds are exceeded although its weight function looks like a good solution. The objective function Φ is used for providing a measure of feasibility of individuals including the design constraints. After evaluating the objective function outputs of the population, each individual is processed by the fitness function. The output of the fitness function is called as "fitness" which indicates the quality of the individual with respect to overall population.

3.3.1.4 Fitness Scaling and Selection

After evaluating fitness values, fitness scaling is generally performed in GA. Raw fitness values obtained from the fitness function are converted to the scaled values. The scaling puts individuals in a range which is suitable for the selection. In the selection step, parents of the next generation are selected by using the scaled fitness values. Individuals with higher scaled fitness have higher probability to be selected. However, scaling method has no effect on some selection methods such as the tournament selection.

In the selection step, poor individuals get eliminated and individuals with high fitness are selected to be reproduced. Selection must occur at each iteration (generation) of the algorithm. The populations of chromosomes evolve over the generations to the mostly fit individuals by selection. Constant number of individuals is kept for mating and the rest die in each generation.

In this thesis, binary tournament selection is used because Matlab GA toolbox provides only binary tournament selection for mixed integer problems. In binary tournament selection, two individuals (or chromosomes) are selected randomly from the population. The individual with higher fitness is selected and this procedure is repeated until the mating pool is full. Each individual has a chance of entering to the mating pool more than once; likewise each individual has a chance of not entering to the mating pool at all. Before starting the tournament selection, fitness values are ordered

according to their absolute fitness values and ranked from highest to the lowest. This process is called rank ordering. Tournament selection is determined by rank ordering of fitness of individuals rather than absolute values. Hence, fitness scaling has no effect on methods used and is not utilized in this thesis.

3.3.1.5 Elitism, Crossover and Mutation

The creation of offspring from two parents (sexual reproduction) or from a single parent (asexual reproduction) is called as reproduction. In reproduction of GA, Sexual reproduction refers to crossover and asexual reproduction refers to elitism. Mutations also take place while producing new offspring from parents in GA.

The preserving best individuals are called as elitism. Elite counting refers to the number of asexual reproduction. Elites directly pass to the next generation without changing their chromosomes.

Crossover is combining pairs of parent chromosomes. Two new child individuals are produced by swapping the genetic information between the mating (parent) individuals. The simplest methods choose one or more locations within genes in the chromosomes to mark as the crossover points. An example of single point crossover for binary coding, which is one of the simplest methods, is shown in Figure 28.

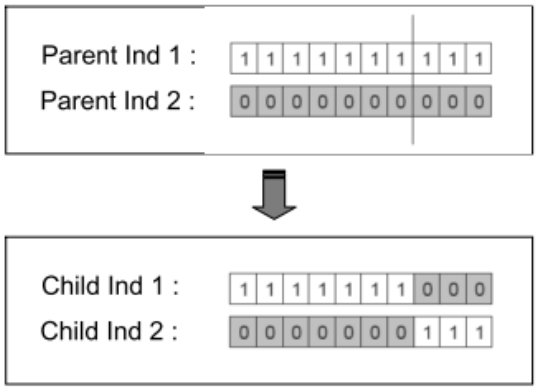

Figure 28 Single Point Crossover

In nature, mutations occur randomly and contribute to the process of evolution by replacing one allele of a gene with another. In GA, mutations are introduced to modify the genes randomly in the chromosomes with low probability. The mutation probability of each gene is typically in the range of 0.001 and 0.01 Mutation is usually considered to be a background operator that guarantees that the possibility of searching a specific subspace of the design space is never zero. Possibility of converging to a local optimum, rather than the global optimum, can be prevented by mutation operation. Moreover, mutations provide a safety net for recovering good genetic material, which otherwise will be lost through selection and crossover [42].

In binary coding, offspring are produced from parent individuals (or chromosomes) by altering a gene randomly. If binary code of the gene is “1”, it becomes ”0”. If binary code of the gene is “0”, it becomes ”1”. A very common binary mutation example is given in Figure 29.

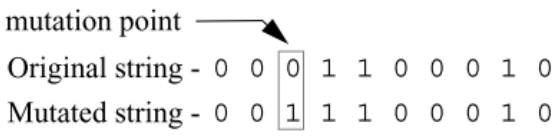

Figure 29 Binary Mutation

For the application of crossover and mutation of mixed integer problems, which have real value coding, require more complex methods. Deep and his colleagues extended “power mutation [43]” and ”laplace crossover [44]” for real-value coded problems. Deep and his colleagues [45] extended their work for integer and mixed-integer problems by applying additional parameters to consider the integer decision variables. In this thesis, this methodology is used for crossover and mutation because the problem is defined as mixed integer problem. In Laplace crossover, possible positions of two offsprings are formulated from two real-valued parents by using Laplace distribution function. An example of parents-offspring relation of Laplace crossover is given in Figure 30. In Figure 30, the density functions (f(x)) of offspring genes which show the probability distribution of offspring values (x) are drawn. Each offspring is selected according to its density function. Probability distributions of each offspring are centered with respect to the parent values which is shown with the black dots in Figure 30.

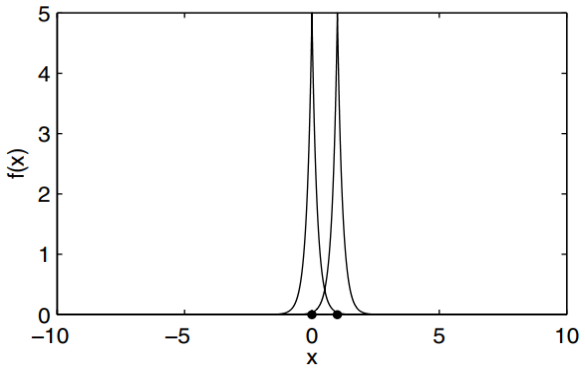

Figure 30 Spread of Offsprings [44]

Representation of elitism, crossover and mutation used for real-valued coded and integer included chromosomes are given in Figure 31. As it can be seen from Figure 31, the chromosomes of elite parents do not have any change in their chromosomes while passing to the next generation. The parent couples are subjected to the crossover operator which produces two offspring. Offspring genes are different than the parent

genes in this example but related to the parents with Laplace crossover operator. The mutated chromosome example given in Figure 31 shows a chromosome having a single gene mutation and it is produced randomly. Given values are just for the illustration. They do not reflect the real mutation and crossover children outputs.

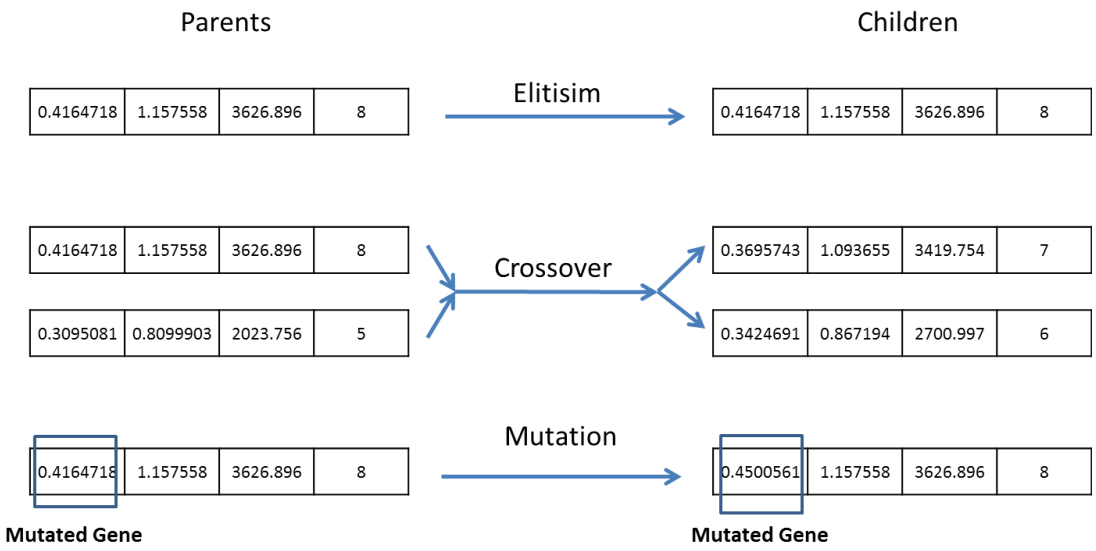

Figure 31 Reproduction Illustration of Real-Value Coded Genes

3.3.1.6 Reproduction Options

Reproduction options in GA, refers to the number or the fraction of sexual reproduction (crossover), asexual reproduction (elitism) and mutations which occur in a population while offspring are produced from parents. It is to be noted that the total number of individuals are conserved while reproduction before describing the reproduction options and Eqn. (3-1) is formulated to show this conservation,

$$\#\,Individuals = \#Elite + \#Crossover + \#Mutation \qquad (3\text{-}1)$$

where *#Individuals*, *#Elite*, *#Crossover* and *#Mutation* represents the total number of individuals, the number of elites, the number of crossover individuals and the number of mutation individuals in the population, respectively. The number of elites (or elite count) is defined at the beginning of the optimization and conserved in every reproduction step. Since total number of individuals and the number of elites are defined at the beginning, the sum of the number of sexual reproduction (crossover) and the number of mutations can be calculated from Eqn. (3-1). If any ratio between the number of crossover and the number of mutations is known, both the number of crossover and the number of mutations can be calculated. This ratio is called as crossover fraction. It refers to the ratio of the number of crossover individuals to the sum of crossover individuals and mutation individuals. The crossover individuals are randomly selected by conserving the crossover fraction. In conclusion, elite count and the crossover fraction are the reproduction options used in this thesis.

In this thesis, as a Matlab default, elite count is taken as 2 and crossover fraction is set as 0.8. Since the number of individuals is 70 in the present optimization problem and elites are 2, the sum of individuals subjected to crossover and mutation are 68. The individuals subjected to crossover are 68 x 0.8 ≅ 54 and the number of mutated individuals is 68 - 54 = 14.

3.3.1.7 Termination of GA

After the completion of crossover and mutation, the child individuals are taken to be the parents of the next population. The creation of a new population from the previous one is called as “single generation” in GA terminology. In GA, new generations are produced until a stopping criterion is satisfied. Mostly, stopping criteria are related to the convergence of the solution or the time consumed during the optimization. Finally, the fittest individual of the population is taken as the optimum solution when the termination of GA occurs.

3.3.2 Cross-Section Optimization (CSO) Constraints

Design variables are limited considering the manufacturability, applicability to design constraints and applicability to geometric constraints. As an example of manufacturability, production of a very small cylindrical nose weight and curing it with the nose block becomes difficult and ineffective in terms of cost. As an example for the applicability to the geometric constraints, nose block boundary limits the maximum nose weight radius because nose weight surface cannot exceed nose weight outer boundary geometrically. As an example of applicability to design constraints, a very thin spar may lead to an unexpected failure because production defects may lead to unexpected and catastrophic failure modes for thin composites and the moisture ingression can also take place in thin composites.

CL, $R_{baseline}$, $STA_{INITIAL}$, STA_{FINAL} and *BS* represent the chord length, nose mass radius of the baseline model, spanwise starting-ending position of the functional region and the blade span length, respectively. The design variable constraints are then defined as:

$$0.29 * CL < X_1 < 0.49 * CL \tag{3-2}$$

$$0.6 * R_{baseline} < X_2 < 1.2 * R_{baseline} \tag{3-3}$$

$$8 < X_3 < 18 \tag{3-4}$$

$$0.1885\ (STA_{INITIAL}/BS) < X_4 < 1(STA_{FINAL}/BS) \tag{3-5}$$

where X_1 is the wall distance from the leading edge, X_2 is the nose weight radius, X_3 is the number of 0-degree plies in the D spar after the drop-off and X_4 is the spanwise ply drop-off position of the spar plies.

For the strength constraint, maximum strain criterion is chosen. For carbon epoxy material, which has the minimum UTS capability among materials used in blade modeling, UTS value is given as 13200 με by Samborsky et al. [46]. However,

considering the impurities, notch sensitivity, material defects, debonding and fatigue behavior, in the present study maximum strain is taken conservatively as 5400 με. The details of the selected strength methodology are given in Critical Design Constraints section.

$$S_{MAX} < 5400\ \mu\varepsilon \tag{3-6}$$

In the present study, 3% chord length eccentricity from the FA is accepted for the CG, SC and the NA in the chordwise direction. Previously, chordwise positions of the sectional centers are nondimensionalized as given by Eqn. (3-7) - Eqn. (3-9),

$$CG_n = x_{m2}/CL \tag{3-7}$$
$$SC_n = x_{s2}/CL \tag{3-8}$$
$$NA_n = x_{t2}/CL \tag{3-9}$$

where CL is the chord length of cross-section, x_{m2} is the location of chordwise CG, x_{s2} is the location of chordwise SC and x_{t2} is the location of chordwise NA. These parameters are calculated from the modelling outputs as explained in Section 2.3.3. Constraint equations in terms of non-dimensional chordwise positions are given by Eqns. (3-10) - (3-12).

$$-3\% < CG_n < 3\% \tag{3-10}$$
$$-3\% < SC_n < 3\% \tag{3-11}$$
$$-3\% < NA_n < 3\% \tag{3-12}$$

3.3.3 Objective Function for the Cross-Section Optimization (CSO)

In the present study, MATLAB Genetic Algorithm Toolbox is used for the CSO. Objective function is defined by Equation (3-13). In Eqn. (3-13) , weight function *f* is subjected to constraints through the penalty parameter (*r*) resulting in the augmented objective function *Φ*. Normalized values of the weight function and the constraints are used, because it is desired to penalize the weight function in a similar order of magnitude due to the constraint violation.

$$\Phi = f + r * (\sum_{k=1}^{N} Constraint_k{}^2) \tag{3-13}$$

Weight of the functional region is normalized by dividing blade weight with the weight of the functional region of the baseline blade, as shown in Eqn. (3-14).

$$f = \frac{\text{Blade Weight of the Functional Region}}{\text{Baseline Blade Weight of Functional Region}} \tag{3-14}$$

Suitable penalty parameter (*r*) is taken as 100 after adequate number of trials performed for the case studies.

$$r = 100 \tag{3-15}$$

Because spanwise drop-off occurs in the spar, two different cross-sections are modeled; one for the section with thick spar and one for the section with thin spar. The assigned constraints have to be satisfied in both sections with the thin and the thick spar. Normalized constraints for the outputs of these two models are given by Eqns. (3-16) -(3-23). The normalized constraint equations are set as inactive for the negative results which means that the problem is in feasible region for the relevant constraint.

$$Constraint_1 = max\left(0\ , \frac{abs(\ CG_{n\_Thick}\ ) - \ 0.03}{0.03}\right) \quad (3\text{-}16)$$

$$Constraint_2 = max\left(0\ , \frac{abs(\ NA_{n\_Thick}\ ) - \ 0.03}{0.03}\right) \quad (3\text{-}17)$$

$$Constraint_3 = max\left(0\ , \frac{abs(\ SC_{n\_Thick}\ ) - \ 0.03}{0.03}\right) \quad (3\text{-}18)$$

$$Constraint_4 = max\left(0\ , \frac{S_{MAX\_Thick} - 5400}{5400}\right) \quad (3\text{-}19)$$

$$Constraint_5 = max\left(0\ , \frac{abs(\ CG_{n\_Thin}\ ) - \ 0.03}{0.03}\right) \quad (3\text{-}20)$$

$$Constraint_6 = max\left(0\ , \frac{abs(\ NA_{n\_Thin}\ ) - \ 0.03}{0.03}\right) \quad (3\text{-}21)$$

$$Constraint_7 = max\left(0\ , \frac{abs(\ SC_{n\_Thin}\ ) - \ 0.03}{0.03}\right) \quad (3\text{-}22)$$

$$Constraint_8 = max\left(0\ , \frac{S_{MAX\_Thin} - 5400}{5400}\right) \quad (3\text{-}23)$$

3.3.4 Convergence Criterion for the Cross-Section Optimization (CSO)

For the CSO, the convergence criterion is set as the maximum number of iterations after performing several trials on case studies. The convergence is assumed to be

reached according to the difference in the augmented objective function Φ between CSO iterations. If the difference in Φ between the last iteration and 3 iterations before the last iteration is less than 10^{-3}, the convergence is satisfied. The details of the convergence criterion selection are given in APPENDIX E. The formulation is given in Eqn. (3-24) and I is defined as the CSO iteration number in the equation.

$$abs(\Phi_{\mathrm{I}} - \Phi_{\mathrm{I}-3}) < 10^{-3} \tag{3-24}$$

3.3.5 Cross-Section Optimization (CSO) Case Studies

Various case studies are chosen to investigate the effect of design variables (X_1, X_2, X_3, X_4) and the suitable penalty parameter and the population size. Selected case studies are held under benchmark constant load condition meaning that the case studies are only subjected to CSO. Several optimization trials have been completed to find suitable penalty parameter for each of the case studies. The details of these trials are given in APPENDIX E. For all cases, population size is set to 70. For the case study 1 and the case study 4, the suitable penalty parameter is found as 100. For the case study 2 and the case study 3, suitable penalty parameter is found as 10. Since the FBO has the same design variables as case study 4, penalty parameter is also taken as 100 for the FBO optimization.

In case study 1, nose mass radius & wall location (X_1 and X_2) are the design variables. Thin cross-section constraints (Eqn. (3-20)-(3-23)) are eliminated as drop-off is not used in this case study.

In case study 2, nose mass radius, wall location and ply number of the spar (X_1, X_2 and X_3) are the design variables. Thin cross-section constraints (Eqn. (3-20)-(3-23)) are eliminated as drop-off is not in this case study.

In case study 3, nose mass radius, wall location and spanwise ply drop-off position (X_1, X_2 and X_4) are the design variables.

In case study 4, nose mass radius, wall location, ply number of the spar for the cross-section after drop-off position, spanwise ply drop-off position (X_1, X_2 and X_3 and X_4) are the design variables.

For case study 3, ply number of the spar after the ply drop-off position is taken constant as 16.

For case studies 3 and 4, ply number of the spar before the drop-off position is taken constant as 18.

3.4 Full-Blade Optimization (FBO)

3.4.1 Full-Blade Optimization (FBO) Constraints

For this study, frequency constraint is considered up to the 8th vibration mode of the blade. Since the first and second modes (first rigid lag and first rigid flap) are not elastic modes and they cannot be changed by the inner blade design, they are not considered in the frequency constraint. Hence natural frequency constraint is formulated as:

$$abs(\omega_n \,/\, \omega_{ref} - j) > 0.2 \qquad (3\text{-}25)$$

where n = 3, 4, 5, 6, 7 and *j* is the closest integer symbolizing the non-dimensional /rev value. ω_{ref} is the operational rotor speed, ω is the current rotor speed and ω_n is the natural frequency of the blade for the current rotor speed

The fan plot representation of natural frequency bounds for $\omega_n \,/\, \omega_{ref} = 7$ is given in Figure 32 as an example. Fan plot description is given in the Section 2.2. Red lines in Figure 32 refer to natural frequency constraint boundaries. In this example, the mode

shown with the purple line violates frequency constraints because it is in between the red lines at the operational speed (ω_{ref}) .

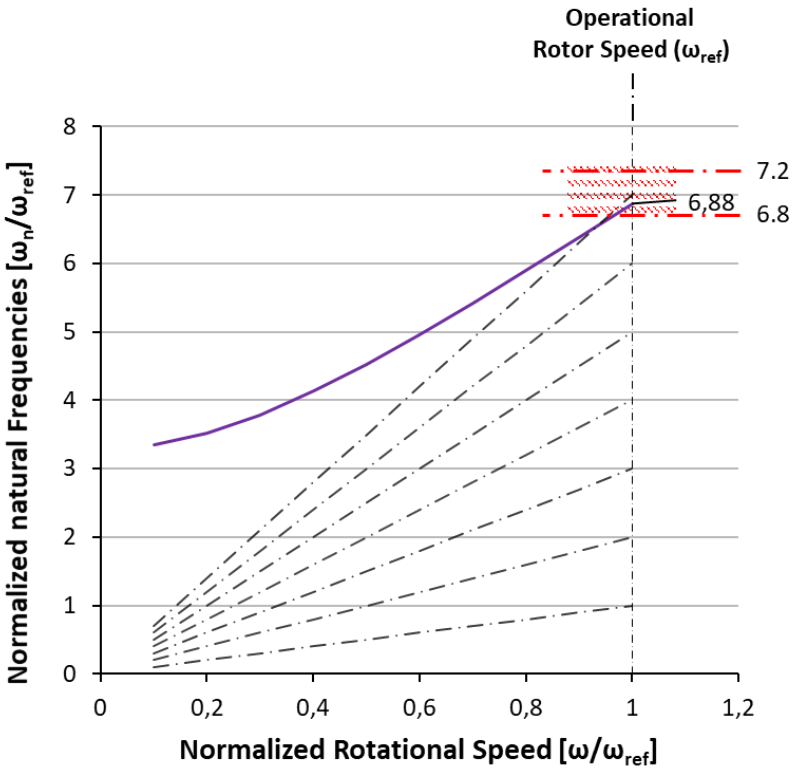

Figure 32 Illustration of Natural Frequency Constraints

3.4.2 Blade Tuning

Satisfying dynamically suitable natural frequencies of the blades can be achieved with the proper tuning of stiffness and mass properties of the structure itself. However, this work is highly tough because many properties are coupled with each other. Another way of natural frequency tuning is performed by manipulating dynamic behavior of the blade without altering structural form of the blade. This can be done via adding nonstructural lumped mass/masses on suitable chordwise and spanwise location/locations of the blade. This method, ”frequency placement”, lets users to tune

the blade in more deterministic way. “Frequency placement” of helicopter rotor blades has been employed since the early stages of the helicopter design.

In the study of Hirsch and coworkers [47], first flapwise natural frequency value was shifted away from 3/rev by introducing additional 300-lb weights to each one of the blades of the XH- 17 helicopter.

Peters and colleagues [17] have studied on the generic design of Bell UH-ID main rotor as a baseline. They tried to move natural frequencies away from resonances for the flapping, cyclic and collective modes of vibration independently. The dynamic behavior was modified by adding nonstructural mass on various positions along the blade and controlled movement of natural frequencies has been achieved.

Walsh and Chattopadhyay [18] used lumped masses while minimizing weight of the helicopter rotor blade in order to tailor the natural frequencies.

As it is given in optimization flow chart, blade tuning is repeated after every Cross-Section Optimization (CSO) step of each iteration of the Full Blade Optimization (FBO). A couple of assumptions are necessary to set a standardized blade tuning methodology. The natural frequency and mode shape behavior of the “baseline blade” and the “CSO optimized blades” are assumed similar to each other. Hence, a significant change in the natural frequency magnitudes and the peaking points of each mode shape is not expected during the overall optimization process. For example, 0.3/rev natural frequency change of any mode can be accepted as significant for natural frequencies and 5% span change of any peaking point of any mode can be accepted as significant for the mode shapes. This is done by considering the limits of design variables and dominance of other parameters such as the rotation frequency, constant span and chord length and cross-section topology.

The fan plot of the baseline blade model obtained by Dymore analysis is given in Figure 33 (See Section 2.2 for the fan plot description). Red lines refer to natural frequency constraint boundaries. Only the elastic modes are shown in the fan plot as the kinematic (or rigid) modes are not considered. Torsion_1, Lag_1 and Flap_3 are the

possible critical modes since they violate or about to violate the natural frequency constraints. The absolute difference between the normalized natural frequencies and the closest /rev of $Torsion_1$, Lag_1 and $Flap_3$ are less than 0.2 or about 0.2. These differences are given as "Normalized Difference" and underlined in Table 5.

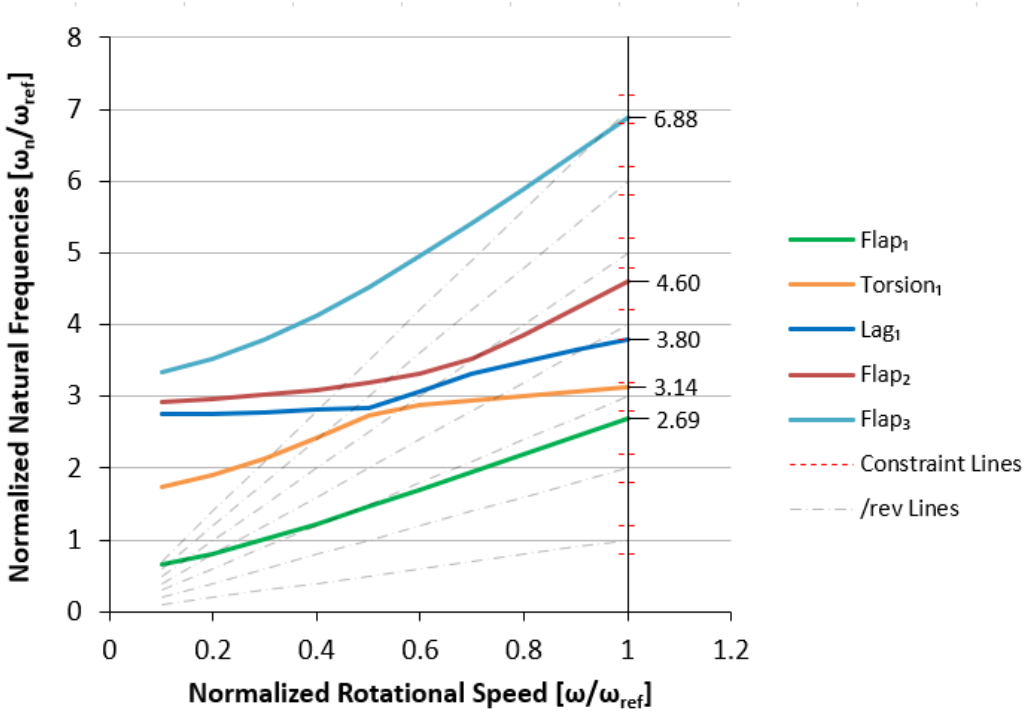

Figure 33 Fan Plot of the Baseline Blade Model

Table 5 Normalized Natural Frequencies of the Baseline Blade Model

	$Flap_1$	$Torsion_1$	Lag_1	$Flap_2$	$Flap_3$
$[\omega_n/\omega_{ref}]$ at Operational Rotor Speed	2.69	3.14	3.80	4.60	6.88
Closest /rev Value	3	3	4	5	7
Normalized Difference	0.31	**0.14**	**0.20**	0.40	**0.12**

According the continuous vibrations, bending modes of a beam generally can be tuned by the application of nonstructural lumped masses. For the beams, natural frequencies

of the bending modes can be decreased by attaching lumped mass. The position and the amount of the lumped mass are the critical parameters. Attachment position to obtain maximum frequency decrement with constant mass is a critical parameter for the optimization. The most effective attachment of the lumped mass is at the peak points of the mode shapes of the corresponding tuned mode. The least effective attachment is the nodal points of the mode shapes. On the other hand, for the rotating beams such as the helicopter rotor blades, there is stiffening effects of lumped mass attachments due to centrifugal forces. Stiffening effect of a lumped mass increases as it gets close to the tip of the blade. Therefore, selecting the peak points closer to the root of the blade is more suitable when the natural frequency of the corresponding mode is desired to be decreased. On the other hand, selecting the nodal point closer to the tip is more suitable to increase natural frequency of the corresponding mode. The simplified diagram of the bending modes and frequency tuning by means of lumped mass addition is given in Figure 34. The lumped mass is assumed as 1 dimensional and the spanwise length of the lumped mass is taken as constantly 200 mm. The necessary lumped mass of each FBO iteration is numerically added to blade cross-section mass properties without changing the 2D cross-sectional model. Mass per unit spanwise length (μ, see APPENDIX A) value of the lumped mass is calculated by dividing the necessary mass by 200 mm. Mass per unit spanwise length values of the blade cross-section and lumped mass are summed in order to find overall mass per unit length value. Then, the summation is substituted into 6x6 mass matrix as mass per length term for the cross-sections where the lumped mass is defined. The lumped mass is added to the cross-sectional CG as the other terms of the mass matrix is not manipulated. “Lumped mass position” term is used as the spanwise position of the midpoint of the lumped mass.

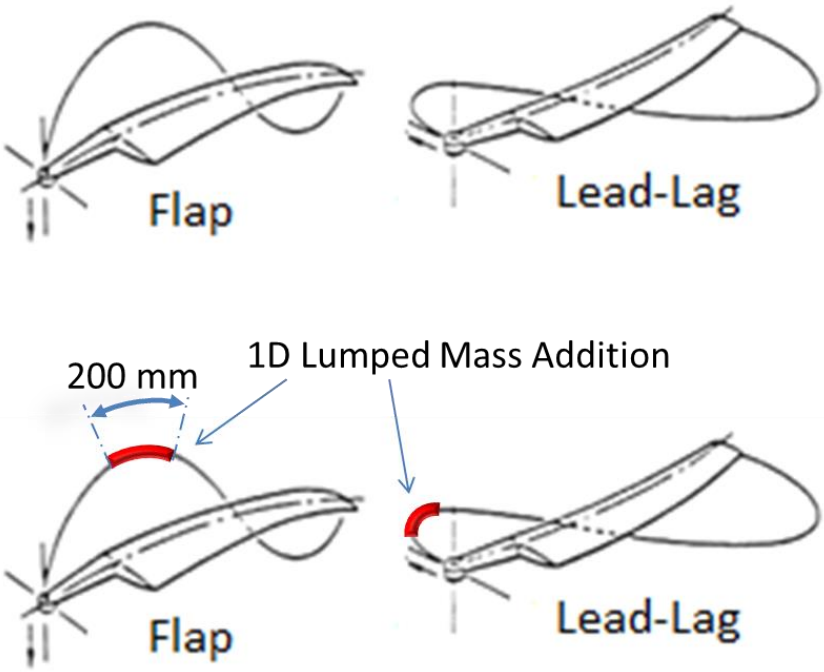

Figure 34 Frequency Tuning of the Bending Modes

Mode shapes of the baseline blade model are shown and critical peaks are marked in Figure 35. In order to tune the Lag_1 and the $Flap_3$ modes at the same time, 27% blade span is selected as the spanwise lumped mass attachment position. Although this position is not peak point of both, it is close to the peaks of both modes and it can still be considered effective for both modes. The cross-sectional position of the lumped mass for both in spanwise and chordwise direction are set as the CG position of the cross-sectional analysis outputs for the current FBO iteration.

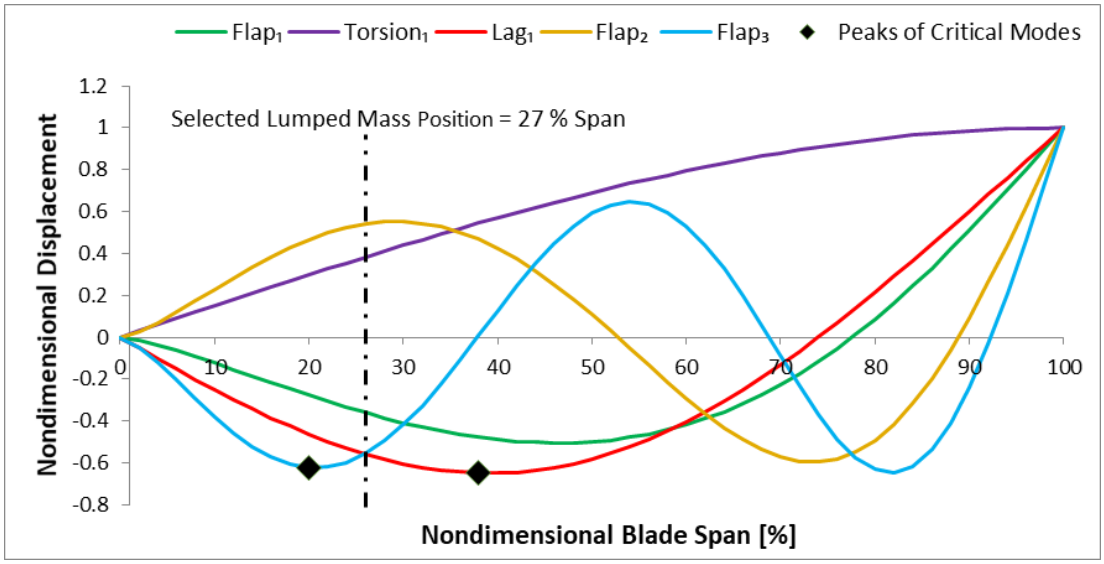

Figure 35 Mode Shapes of the Baseline Blade Model

For the critical natural frequency of the $Torsion_1$ mode, it is necessary to increase normalized natural frequency from 3.14 to at least 3.20. The difference is 1.9%. For the natural frequency tuning of the torsion mode, polar moment of inertia and torsional stiffness changes are the dominant parameters. In this thesis, there is no significant torsional stiffness change because the erosion shield, inner-outer wraps and skin remain constant during the optimization process. Hence, torsional stiffness tuning is only possible by polar moment of inertia change. Decreasing the polar moment of inertia without changing torsional stiffness leads to an increase in the natural frequency. Fortunately, the decrement in the polar moment of inertia of the blade is expected during the optimization process itself, because the aim of the overall optimization is weight minimization. Moreover, violation of the natural frequency constraint is only 1.9%. Hence, natural frequency tuning of the $Torsion_1$ mode by the optimization process itself is expected, and no other modifications specifically for the torsion mode is performed.

Consequently, in this thesis, mass tuning position is selected at 27% span of the blade on the feathering axis. Mass tuning is only applied for Lag_1 and $Flap_3$ which are expected as the critical modes of each iteration of the FBO. The amount of the lumped

mass is identified according to the natural frequency mismatch of the current FBO iteration by several trials. Moreover, self-tuning is expected from the $Torsion_1$ mode. Fan plots and mode shapes of the CSO optimized blade models are checked after every CSO optimization. This is done because significant changes might occur and the assumptions would fail. For example, spanwise peaking positions of the mode shapes may significantly shift because spanwise mass per length distribution can significantly change during the optimization. If unexpected behavior is not observed, the procedure is repeated. In the case of any unexpected behavior, lumped mass application point is altered. In the results section, mode shapes and fan plots of every iteration of the FBO and their tuned versions are shown and compared. The validity of the assumptions is also shown by the comparisons in the results section.

3.4.3 Calculation of the Blade Loads

Blade loads are calculated with respect to feathering axis for each cross-section. The blade loads, which are calculated for the blade model in vacuum, are magnified to cover the overall flight conditions. It is assumed that rotor works with 200% of its operational speed while magnifying the loads. This magnification is based on a private conversation with a consultant who has experience in decades on helicopter field and worked with pioneer companies of helicopters such as Bell Helicopters. Magnified loads are used for both load convergence check and the strain calculation steps. Three forces and three moments subject to each cross-section at the feathering axis are symbolized as F_1, F_2, F_3, M_1, M_2 and M_3. F_1 is the spanwise force. F_2 is the chordwise shear force. F_3 is the flapwise shear force. M_1 is the torsion. M_2 is the flap bending moment. M_3 is the chord bending moment. It is to be noted that reference axis system of the calculated loads is the same as S_{ref}. Hence, Section 2.3.3 as S_{ref} is defined can be seen for the detailed information for the load direction information.

3.4.4 Convergence Criterion for the Full-Blade Optimization (FBO)

In the second level of the FBO process, as defined in Eqns. (3-26) - (3-28), 0.1% difference in the axial internal load (F_1) and 20% difference in the internal bending moments (M_2 and M_3) between iterations is accepted as the convergence criterion. The bending moment convergence is taken as a large figure, because the moments are expected to be relatively small compared to the axial internal load. The reason is that since aerodynamic loads are excluded, the moments are created by the centrifugal force only and the center mismatch of the NA and the FA is constrained to be small by the CSO optimization. The convergence is only accepted when all three equations are satisfied.

Load data of 2 cross-sections are used while calculating the strains in CSO steps, one is the blade root and the other one is the spanwise position where drop-off ends. Because, the maximum axial load occurs in the blade root for the thick cross-section and the maximum axial load occurs in the spanwise position where drop-off ends for the thin cross-section. However, only the loads of the spanwise position where drop-off ends are used while calculating the load convergence. The reason is that the latest load convergence is expected at the drop-off position along the blade by the virtue of the variability of the drop-off position between FBO iterations. Moreover, drop-off position tends to be more critical than the root position due to having smaller spar at the drop-off position. In addition to convergence check with these three inequalities, spanwise distribution of F_1, F_2, F_3, M_1, M_2 and M_3 are visualized for each FBO iteration. The convergence of each load distribution is also checked visually with the help of these plots because the plots of serial iterations get close to each other as the iteration number increases and convergence is approached. The internal loads are calculated by Dymore for each cross-section continuously in each iteration of FBO.

$$\mathrm{abs}(F_{1(j)} - F_{1(j-1)}) < 1\% \qquad (3\text{-}26)$$

$$\text{abs}(M_{2(j)} - M_{2(j-1)}) < 20\% \quad (3\text{-}27)$$

$$\text{abs}(M_{3(j)} - M_{3(j-1)}) < 20\% \quad (3\text{-}28)$$

where j is the FBO iteration number. In Eqns.(3-26) - (3-28), F_1, M_2 and M_3 denote the axial internal load, flapwise bending moment and chordwise bending moment at the spanwise ply drop-off station respectively.

3.4.5 Extended Flow Chart of the Optimization Approach

The expanded flow chart of the overall optimization approach is given in Figure 36 for a complete understanding of the process. Calculation of the baseline and the optimized loads, connection of CSO and FBO steps, input-output flow of the utilized tools and design variables and constraints are all included in this chart.

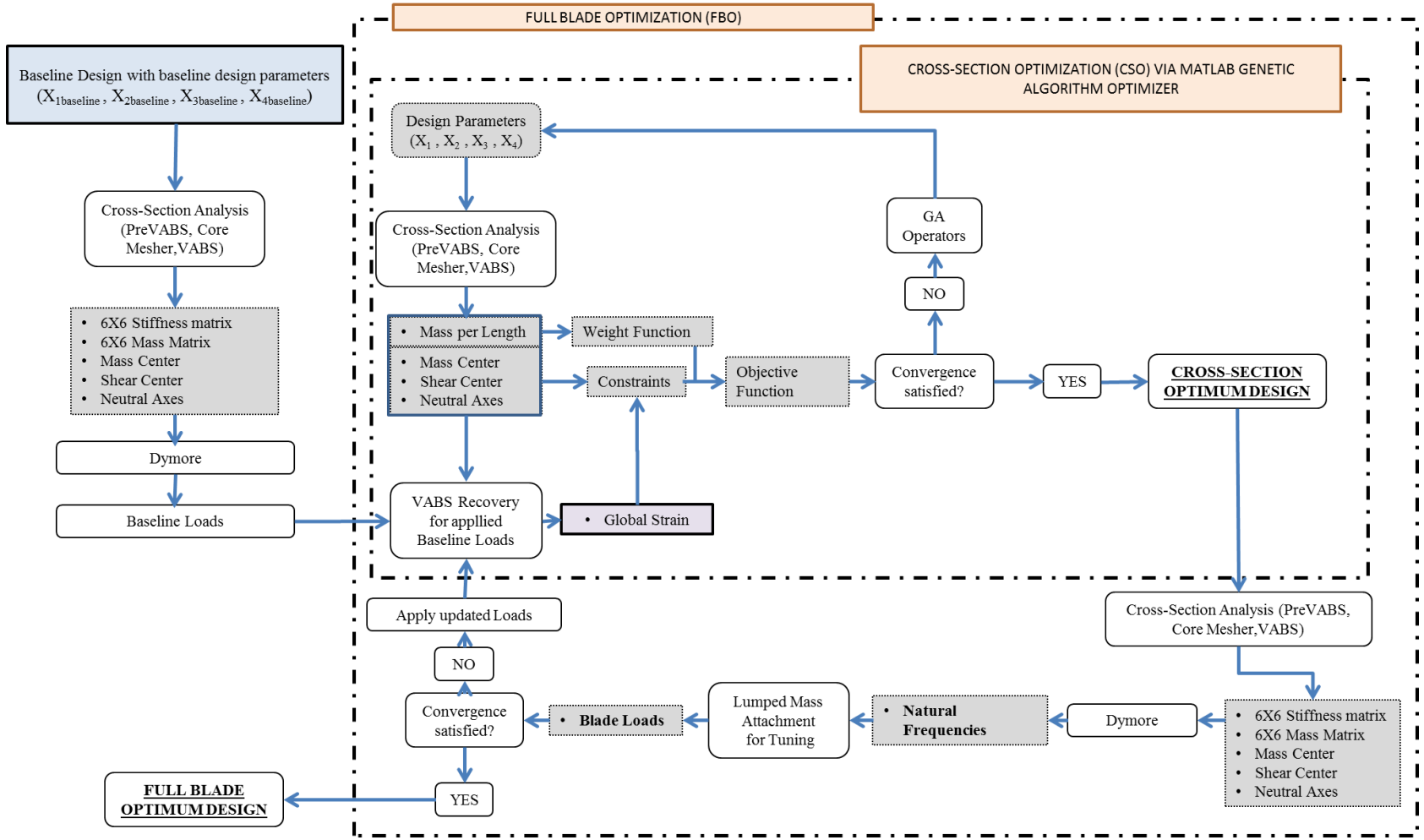

Figure 36 Extended Optimization Flow Chart

CHAPTER 4

RESULTS

4.1 Case Study Results

Various case studies are chosen to investigate the effect of design variables (X_1, X_2, X_3, X_4), the suitable penalty parameter and the population size. Selected case studies are held under benchmark constant load condition meaning that the case studies are only subjected to CSO. In case study 1, X_1 and X_2 are the design variables. In case study 2, X_1, X_2 and X_3 are the design variables. In case study 3, X_1, X_2 and X_4 are the design variables. In case study 4, X_1, X_2 and X_3 and X_4 are the design variables. The detailed description of the case studies is given in Section 3.3.5. For the first step of the optimization (CSO only), Figure 37 give the variation of fitness value with the generation number for case studies 1-4. For the first step of the optimization, Table 6 compares the optimized blade configurations with the baseline design. Table 6 shows that when four of the design variables (case study 4) are taken into account in the optimization process, highest weight reduction is achieved.

Table 6 Comparison of the Baseline Design with the Optimized Designs Obtained in Case Studies 1-4

	Baseline Design	Case 1	Case 2	Case 3	Case 4
Mass					
Mass of Functional Region (kg)	36.91	34.44	33.21	31.32	30.88
Weight Reduction (kg)	-	2.47	3.70	5.59	6.03
% Weight Reduction	-	6.68	10.02	15.14	16.34
Optimum Design Variables					
X_1: Non-Dimensional Wall Distance from LE	0.390	0.375	0.380	0.380	0.379
X_2: Nose Weight Radius (mm)	5.00	3.11	3.00	3.00	3.01
X_3: Spar Ply Number	18	-	16	16 (cnst.)	8
X_4: Non-Dimensional Spanwise Drop-off Position	-	-	-	0.492	0.540

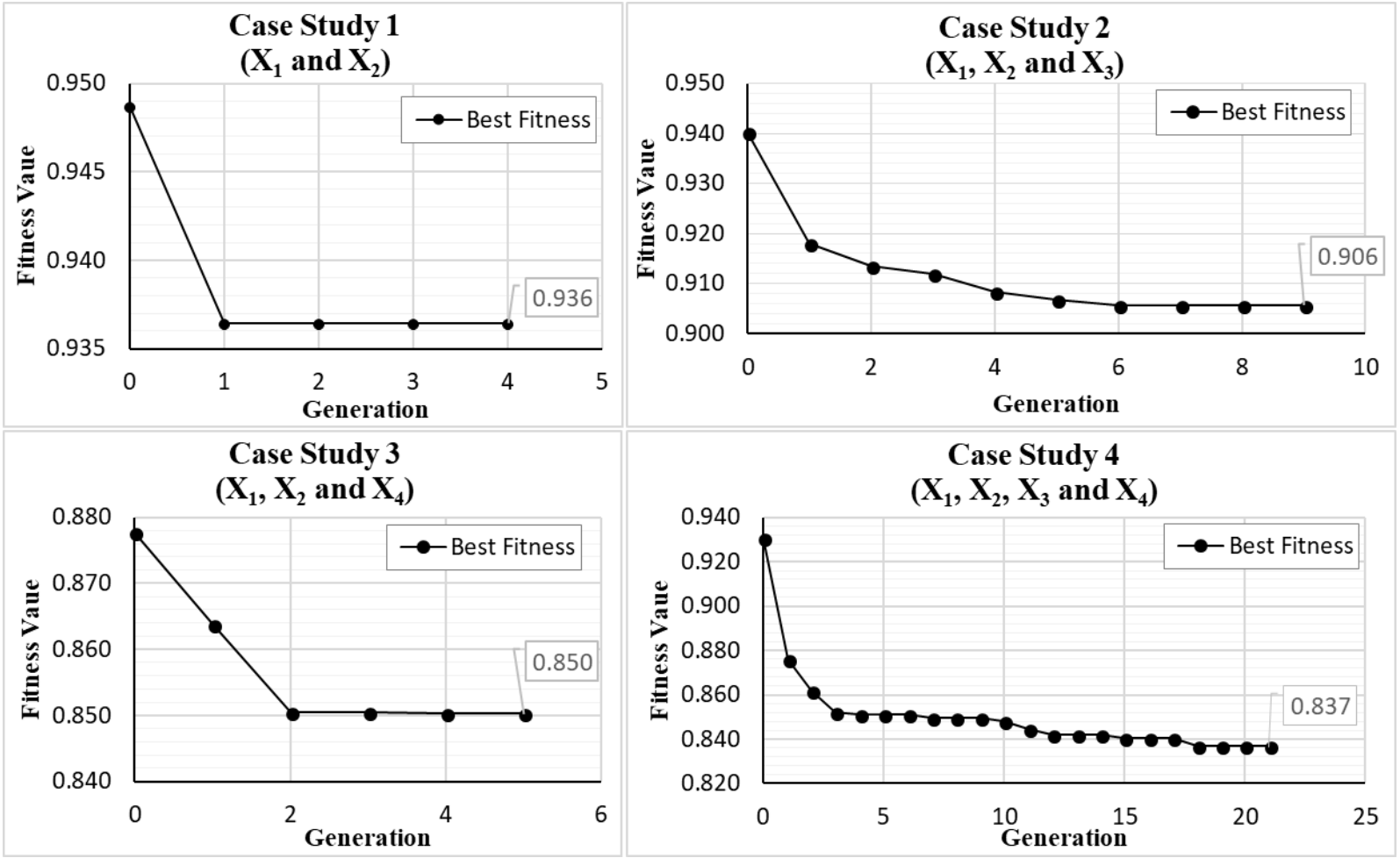

Figure 37 Fitness Variation of Case Studies

4.2 Full-Blade Optimization (FBO) Results

Full blade optimization procedure is done in 3 iterations. The first iteration refers to the cross-section optimization with the internal loads calculated for the baseline blade design. The second and the third iterations refer to the cross-section optimization performed with the updated internal loads calculated by Dymore with the mass tuned blade. The convergence is assumed to be achieved when 0.07% maximum difference occurs in the tuned axial loads between iterations 2 and 3. Figure 38 shows the spanwise load distributions (F_1, F_2 and F_3) and Figure 39 shows the spanwise moment distributions (M_1, M_2 and M_3) along the blade for the baseline design and iterated designs for mass tuned versions.

Fan plots of all iterations with un-tuned and tuned versions are given in Figure 40 (See Section 2.2 for fan plot description). Red lines refer to natural frequency constraint boundaries. Only the elastic modes are shown in the fan plot as the kinematic (or rigid) modes are not taken into account. Normalized natural frequencies and their closest /rev difference of each FBO iteration at operational speed are also listed in Table 7. In Table 7, underlined values show the /rev difference values less than 0.2, hence the natural frequency constraint violation.

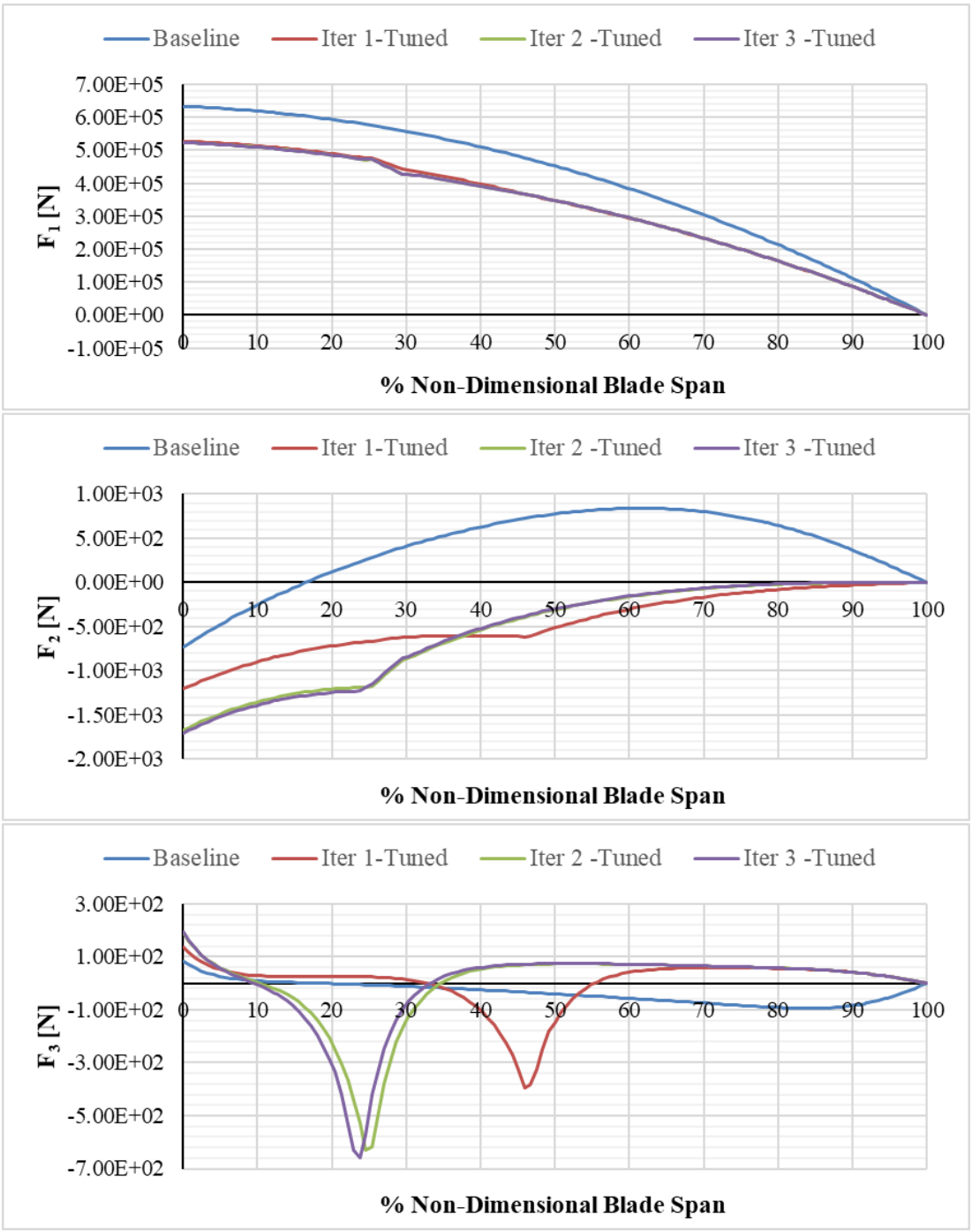

Figure 38 Spanwise Distribution of Axial, Chordwise and Flapwise Forces for ongoing FBO Iterations

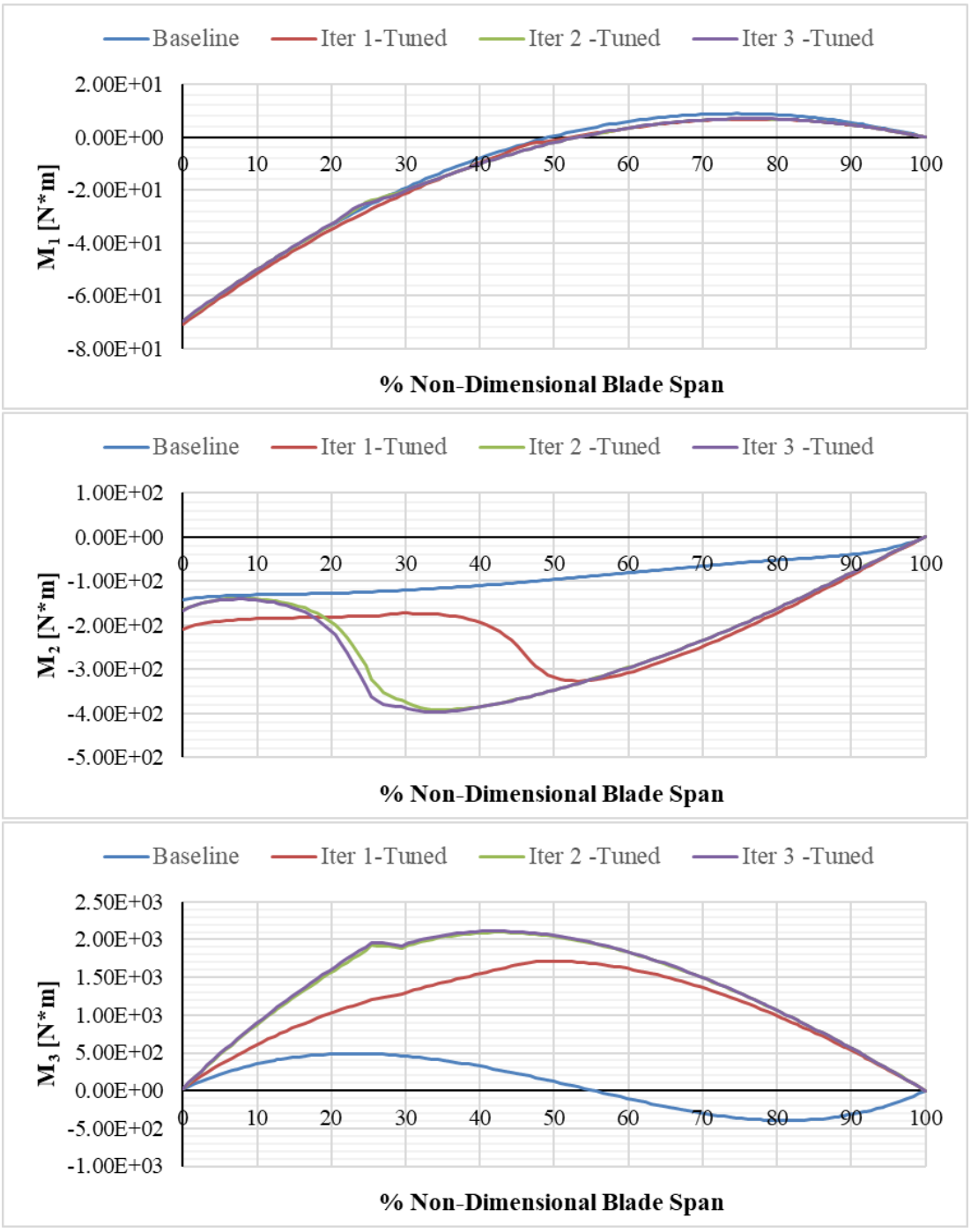

Figure 39 Spanwise Distribution of Torsional, Flapwise Bending and Chordwise Bending Moments for ongoing FBO Iterations

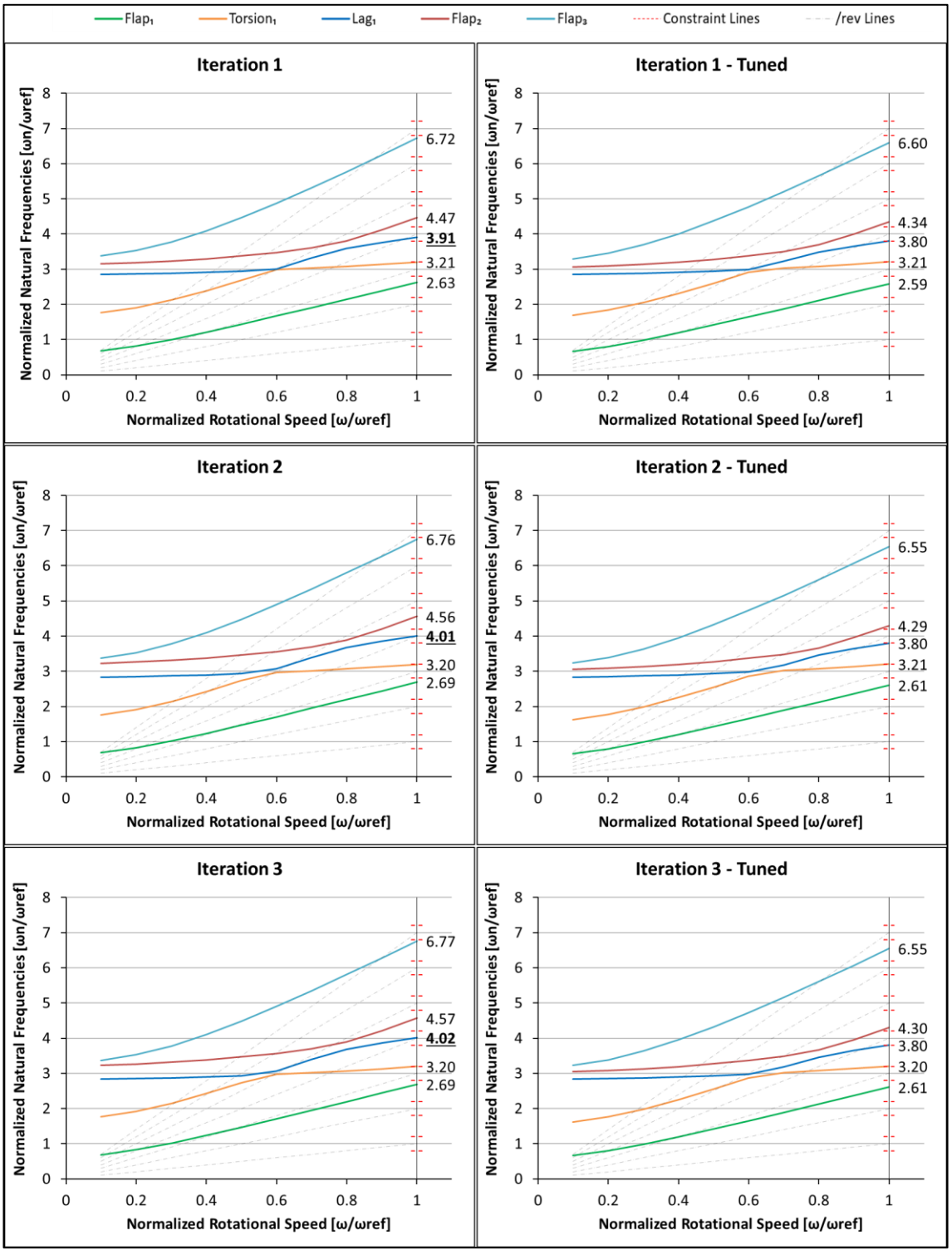

Figure 40 Fan Plot Representations of FBO Iterations

Table 7 Normalized Natural Frequencies of FBO Iterations

Iteration 1	$Flap_1$	$Torsion_1$	Lag_1	$Flap_2$	$Flap_3$
$[\omega_n/\omega_{ref}]$ at Operational Rotor Speed	2.63	3.21	3.91	4.47	6.72
Closest /rev Value	3	3	4	5	7
Normalized Difference	0.37	0.21	**0.09**	0.53	0.28

Iteration 1 - Tuned	$Flap_1$	$Torsion_1$	Lag_1	$Flap_2$	$Flap_3$
$[\omega_n/\omega_{ref}]$ at Operational Rotor Speed	2.59	3.21	3.80	4.34	6.60
Closest /rev Value	3	3	4	5	7
Normalized Difference	0.41	0.21	0.20	0.66	0.40

Iteration 2	$Flap_1$	$Torsion_1$	Lag_1	$Flap_2$	$Flap_3$
$[\omega_n/\omega_{ref}]$ at Operational Rotor Speed	2.69	3.20	4.01	4.56	6.76
Closest /rev Value	3	3	4	5	7
Normalized Difference	0.31	0.20	**0.01**	0.44	0.24

Iteration 2 - Tuned	$Flap_1$	$Torsion_1$	Lag_1	$Flap_2$	$Flap_3$
$[\omega_n/\omega_{ref}]$ at Operational Rotor Speed	2.61	3.21	3.80	4.29	6.55
Closest /rev Value	3	3	4	5	7
Normalized Difference	0.39	0.21	0.20	0.71	0.45

Iteration 3	$Flap_1$	$Torsion_1$	Lag_1	$Flap_2$	$Flap_3$
$[\omega_n/\omega_{ref}]$ at Operational Rotor Speed	2.69	3.20	4.02	4.57	6.77
Closest /rev Value	3	3	4	5	7
Normalized Difference	0.31	0.20	**0.02**	0.43	0.23

Iteration 3 – Tuned (Final Model)	$Flap_1$	$Torsion_1$	Lag_1	$Flap_2$	$Flap_3$
$[\omega_n/\omega_{ref}]$ at Operational Rotor Speed	2.61	3.20	3.80	4.30	6.55
Closest /rev Value	3	3	4	5	7
Normalized Difference	0.39	0.20	0.20	0.70	0.45

Figure 40 and Table 7 show that at the end of the iteration 3, natural frequency constraints are all satisfied. The lowest difference between the normalized natural frequency and the non-dimensional /rev value is approximately 0.2 for iteration 3. This value is specified as the natural frequency constraint given by Eqn. (3-25). Hence, final configuration satisfies the natural frequency constraint.

When the optimized natural frequencies (at the end of iteration 3) are compared with the baseline natural frequencies given in Table 5, improvements can be seen for the critical modes which are $Torsion_1$, Lag_1 and $Flap_3$. $Torsion_1$ shifts to the constraint boundary from the infeasible region by optimization itself as it is expected. Lag_1 is shifted to the constraint boundary with the proper lumped mass attachment in a deterministic manner along the FBO iterations. $Flap_3$ shifts from 6.88/rev to the 6.55/rev. $Flap_3$ becomes one of the safest mode because the closest constraint boundaries are 6.8/rev and 6.2/rev. The other modes, $Flap_3$ and $Flap_3$, saved their feasible positions although their values have moved in the feasible region.

The mode shapes of FBO iterations with their tuned versions are given in Figure 41. The peak points of each iteration and their tuned versions are similar. This similarity proves the beginning assumption on mode shape behavior which is the peak positions of mode shapes do not change or change in very small values between FBO iterations. Therefore, correct choice of lumped mass attachment position is achieved because the peak positions of mode shapes determines the effective lumped mass attachment position.

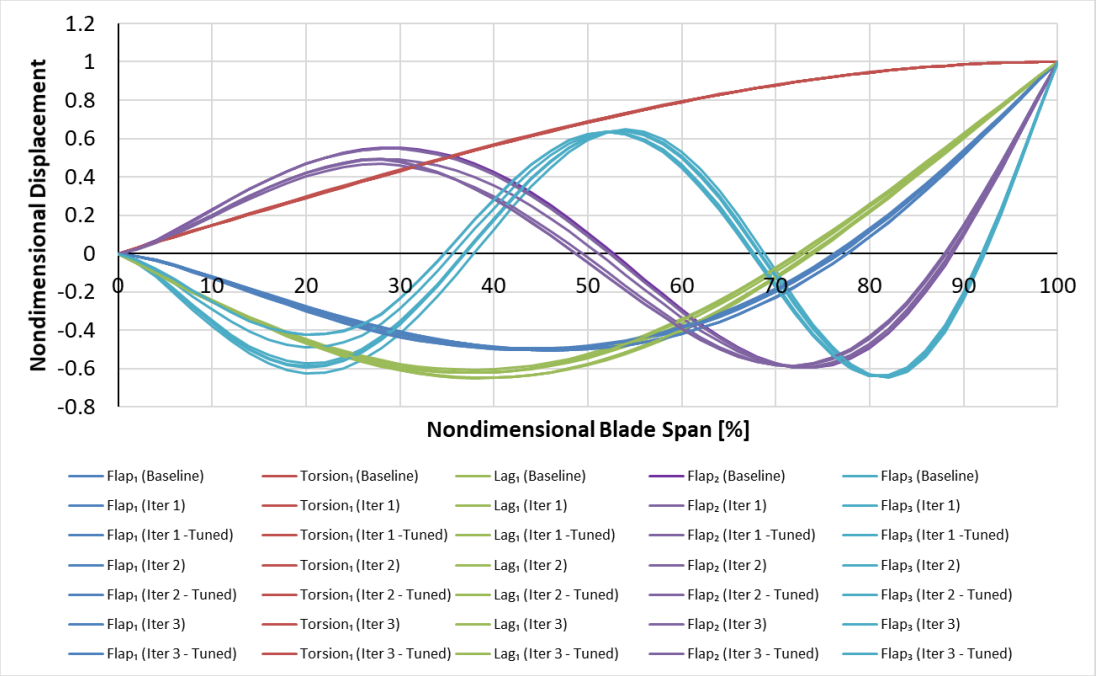

Figure 41 Mode Shapes of FBO Iterations with Their Tuned Versions

For the full blade optimization, Figure 42 gives the variation of the fitness value with the generation number for iterations 1,2 and 3, respectively.

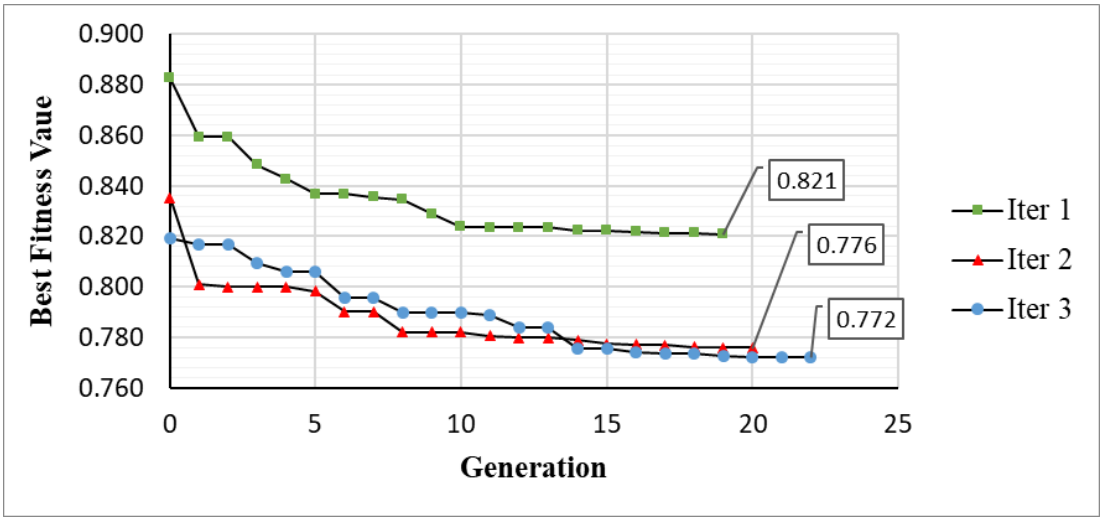

Figure 42 Fitness Variation for Iteration 1, 2 and 3 in FBO

In order to show the difference between the baseline and the optimized design, cross-sections of the baseline and the optimized blade obtained at the end of iteration 3 are given in Figure 43. In Figure 43, thick cross-section corresponds to the constant cross-section from the root of the blade to the spanwise drop-off position. Thin section corresponds to the constant cross-section from spanwise drop-off position to the tip of the blade.

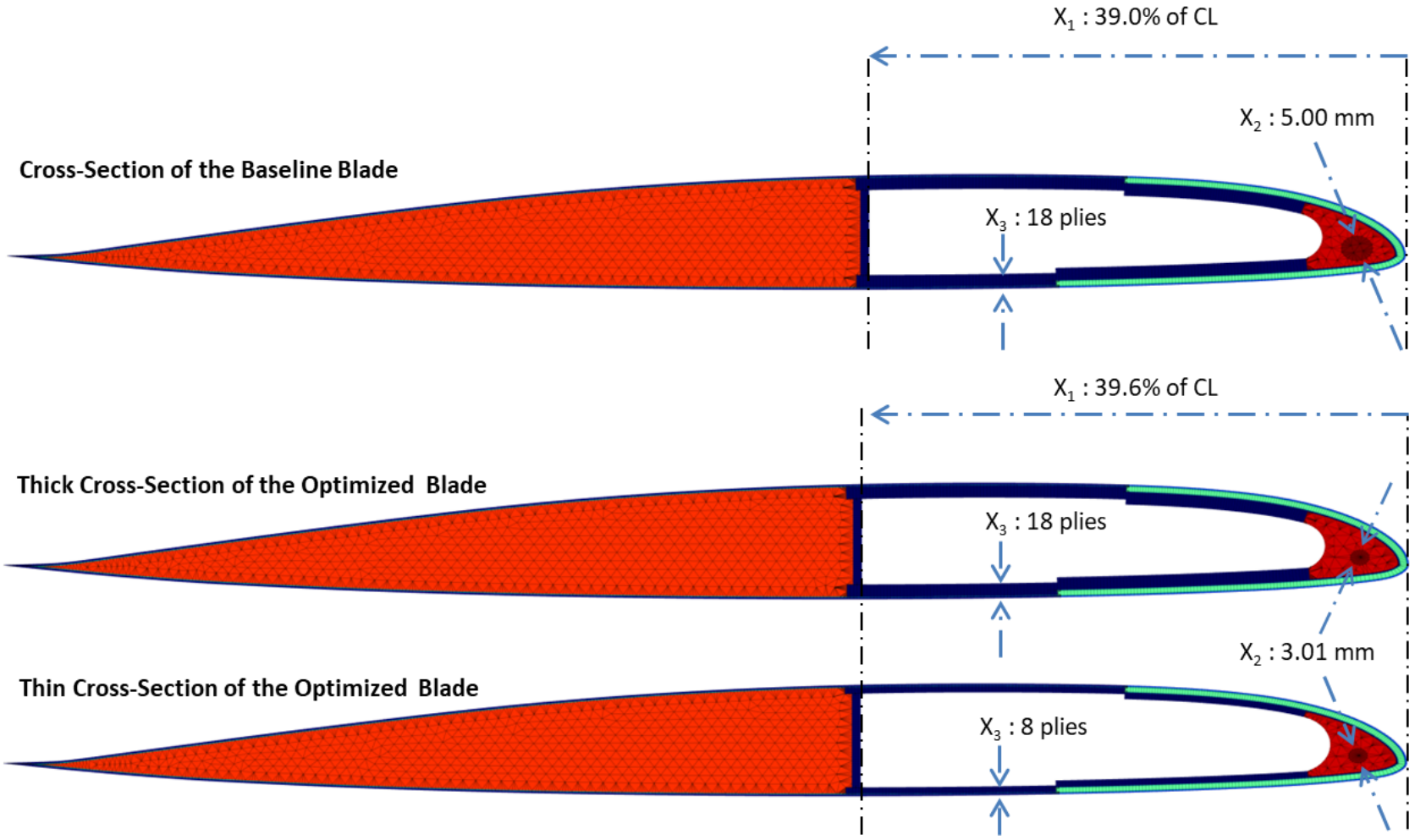

Figure 43 Cross-Sections of the Baseline and the Optimized Blades

Spanwise mass and stiffness distribution of the optimized blade is given in Figure 44 and Figure 45 respectively. Only diagonal terms of mass and stiffness matrixes are shown. The descriptions of sectional property symbols are explained in APPENDIX A. Mass and Stiffness values are normalized by dividing them to the values of baseline blade. Lumped mass effect can be seen from outgrowth of μ distribution in the upper-left subplot of Figure 44. The most significant changes caused by the optimization are observed in m_{22}, S_{11} and S_{55} after the spanwise drop-off position of the spar. On the other hand, m_{22}, S_{11} and S_{55} values of the blade before the spanwsie drop-off position are similar with the baseline design. Hence, the decrement of number of plies on the spar has about 20% effect on flapwise inertia, flapwise stiffness and axial stiffness values.

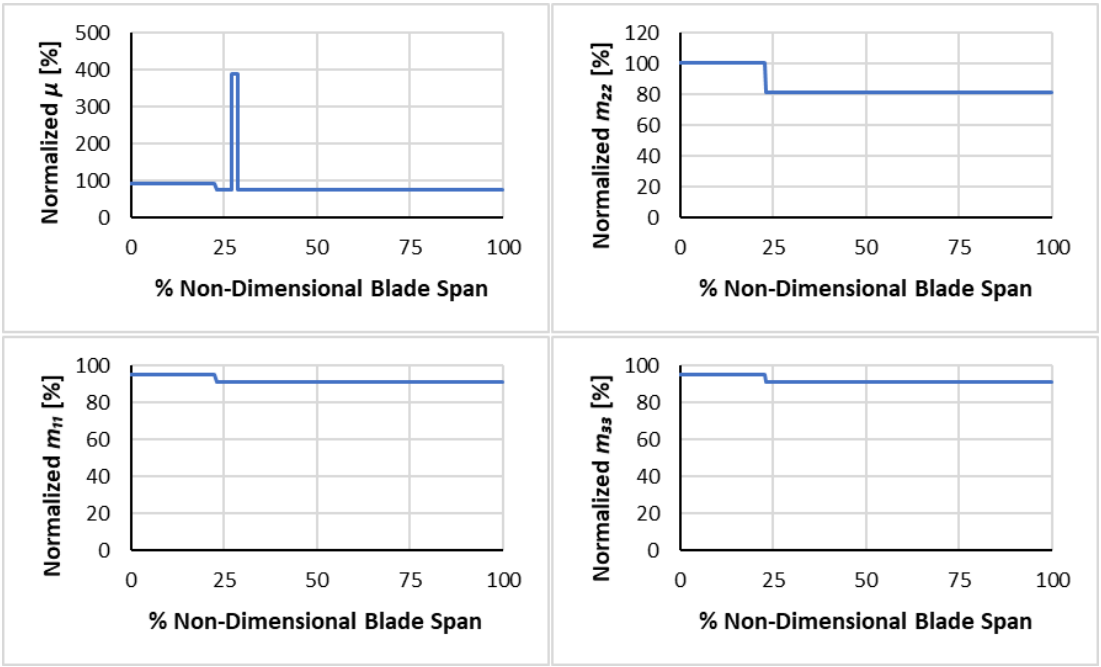

Figure 44 Spanwise Mass Property Distributions of the Optimized Blade

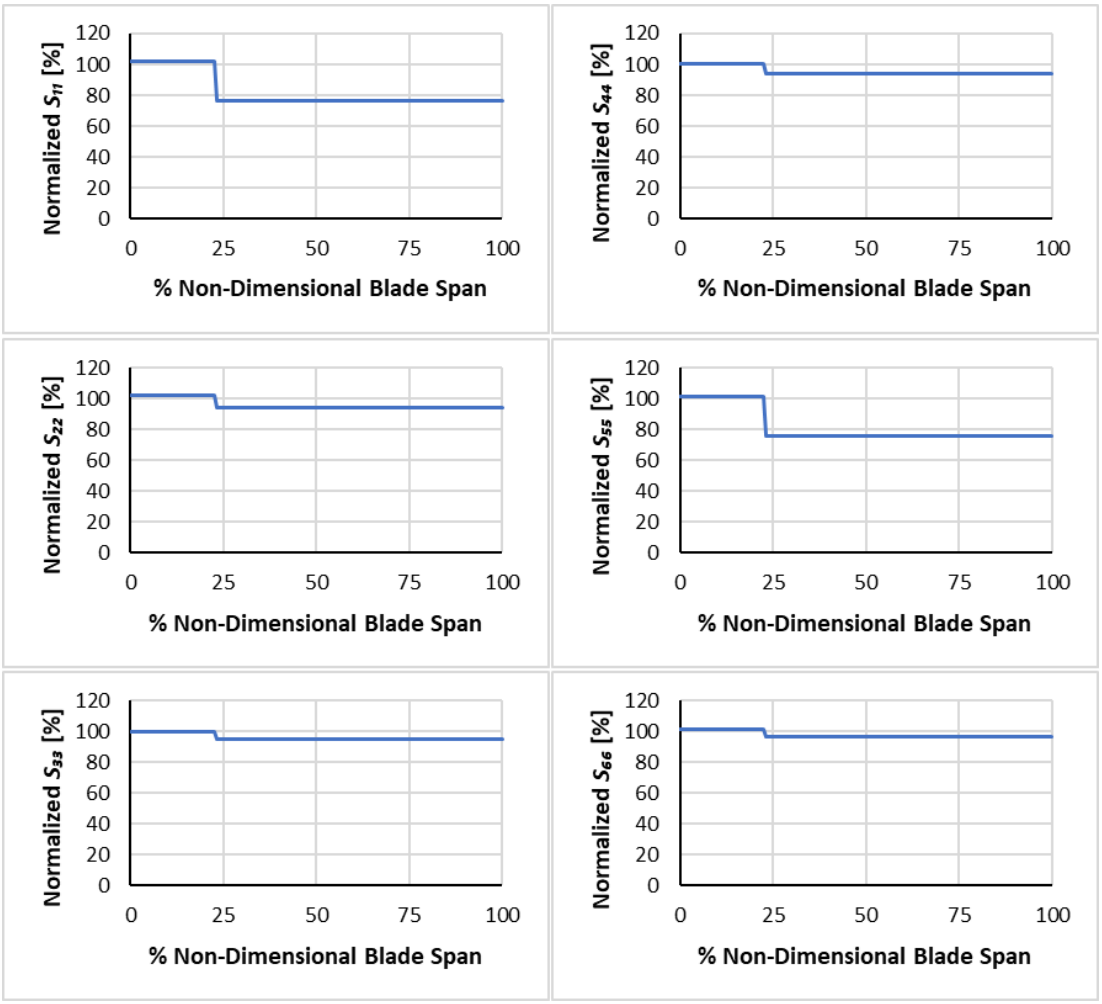

Figure 45 Spanwise Distributions of Normalized Stiffness Properties of the Optimized Blade

Spanwise sectional center distributions of the baseline and optimized designs are compared in Figure 46. Chordwise CG, NA and SC distributions with respect to the FA are nondimensionalized by dividing them to the Chord Length (*CL*). Non-dimensional equations of sectional centers are given from Eqn. (3-7) to Eqn. (3-9). Chordwise CG, NA and SC values are given as x_{m2}, x_{t2} and x_{s2} respectively. The symbols, x_{m2}, x_{t2} and x_{s2}, are explained in APPENDIX A. As it can be seen from the Figure 46, non-dimensional centers in chordwise direction (CG_n, SC_n *and* NA_n) of optimized blade are in 3% with respect to the FA. This shows that optimized blade satisfies the sectional-center constraints.

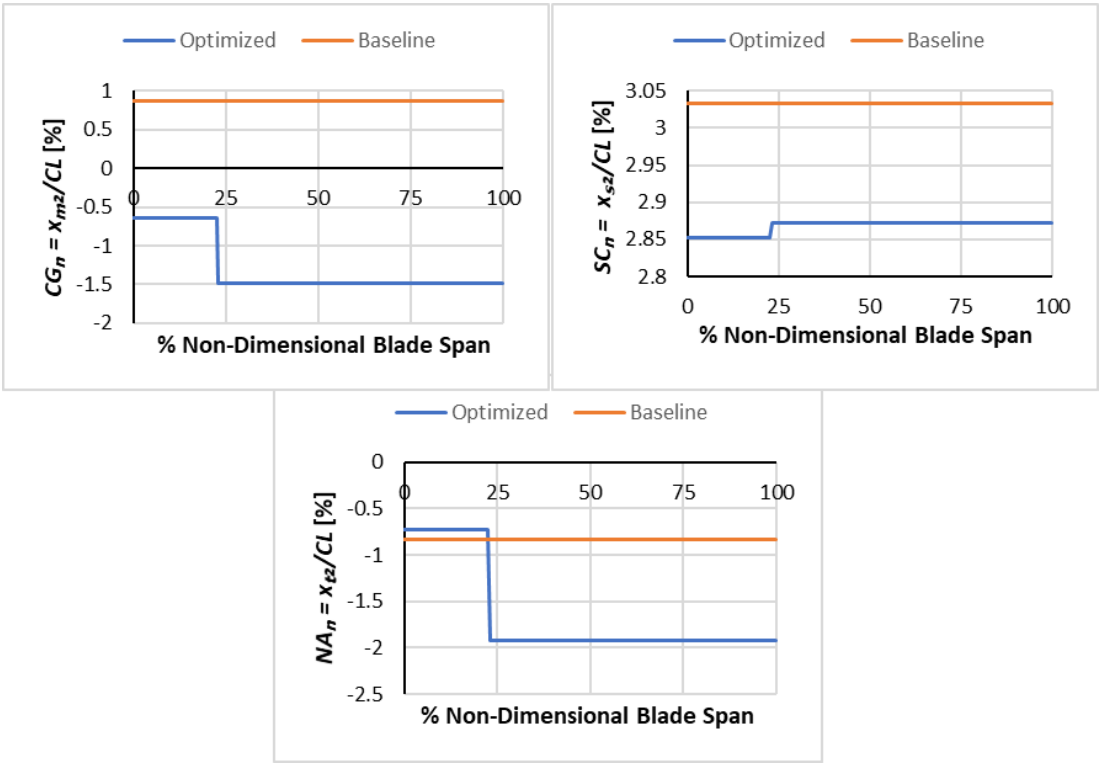

Figure 46 Spanwise Distributions of Sectional Centers (CG, SC and NA) with respect to the FA

For the critical sections along the blade span, blade root (0% blade span) and ply drop-off position (22.6% blade span), cross-sectional strain plots of the baseline and the optimized blade are given in Figure 47 and Figure 48 in 2D FEM format, respectively. Maximum and minimum strain values and sectional positions are also included in the figures. Figure 48.a represents the root section while Figure 48.b represents ply drop-off section. Maximum spanwise strain value of the thick cross-section (S_{MAX_Thick}) is 3794 με while the maximum spanwise strain value of the thin cross-section (S_{MAX_Thin}) is 5410 με. S_{MAX_Thick} and S_{MAX_Thin} are compared to the sectional strain constraint of the optimization procedure which is 5400. S_{MAX_Thick} satisfies this constraint safely at the end of the optimization. The S_{MAX_Thin} converges to the constraint boundary with 0.18% constraint violation which is acceptable. Higher magnitude of S_{MAX_Thin} and constraint boundary convergence of S_{MAX_Thin} makes this cross-section the critical

cross-section. In addition, for both of the optimized cross-sections, upper-top of the blade is the position where maximum strain occurs. It is to be noted that, spar, skin, erosion shield, inner-outer wraps and dummy heater mat are all close to this point.

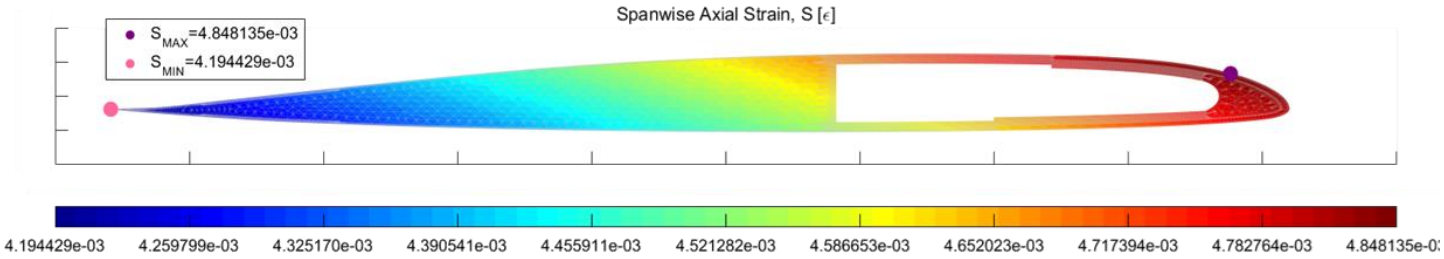

Figure 47 Cross-Sectional Strain Distribution at the Root of the Baseline Blade

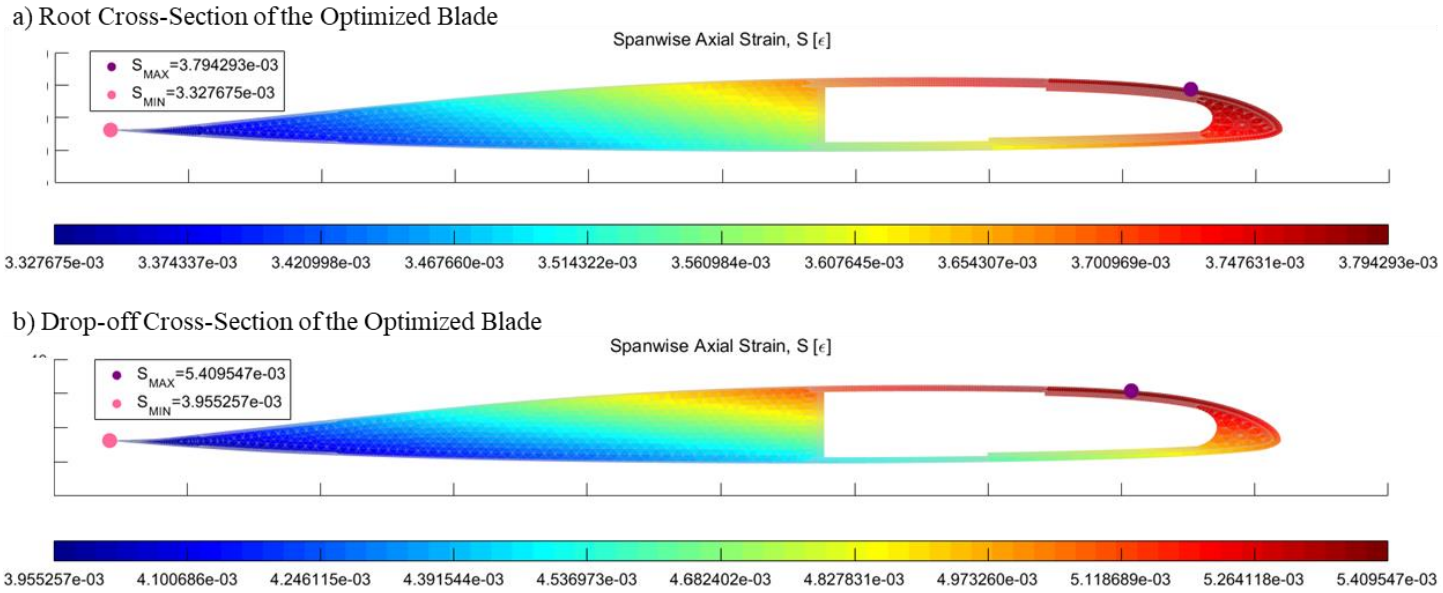

Figure 48 Cross-Sectional Strain Distribution at the a) Root and b) Drop-off Position of the Optimized Blade

Table 8 summarizes the design variables of the full blade optimization, and the achieved weight reduction. Table 8 also gives the differences in the axial load at the ply drop-off position between the iterations. At the end of iteration 3, the difference in the axial force, chordwise and flapwise bending moments at the ply drop-off location are 0.07%, 15.18% and 2.97% lower with respect to the optimum design achieved at the end of iteration 3, respectively. Table 8 shows that at the end of iteration 3, 16.55% mass reduction can be achieved compared to the baseline design.

Table 8 Full Blade Optimization (FBO) Results

	Baseline Design	**Iter 1**	**Iter 2**	**Iter 3**
Mass				
Mass of the Functional Region (kg)	36.91	30.30	28.64	28.49
Necessary Lumped Mass for Tuning (kg)	-	1.22	2.26	2.31
Total Mass (kg)	36.91	31.52	30.90	30.80
Mass Reduction (kg)	-	5.39	6.01	6.11
% Mass Reduction	-	14.60	16.28	16.55
Load Convergence				
% Load Convergence at the Drop-off Position (F_{1j}-$F_{1(j-1)}$)	-	23.24	0.99	0.07
% Load Convergence at the Drop-off Position (M_{2j}-$M_{3(j-1)}$)	-	175.92	62.20	15.18
% Load Convergence at the Drop-off Position (M_{3j}-$M_{3(j-1)}$)	-	785.00	57.15	2.97
Variables				
X_1: Non-Dimensional Wall Distance from the LE	0.390	0.391	0.395	0.396
X_2: Nose Weight Radius (mm)	5.00	3.11	3.02	3.01
X_3: Spar Ply Number	18	8	8	8
X_4: Non-Dimensional Spanwise Drop-off Position	-	0.467	0.247	0.226

It should be noted that there is a slight difference between the optimized mass outputs of Case 4 and the first iteration of the FBO although equal optimized mass outputs are expected. The reason for this is the improvements in the Dymore model between the case studies and the FBO.

CHAPTER 5

CONCLUSION

In this study, weight optimization of the helicopter rotor blade is performed for the centrifugal load case only without considering the aerodynamic loads. Four different case studies are considered by changing the design variables. Full Blade Optimization (FBO) is performed including the Cross-Section Optimization (CSO) utilizing four design variables, blade tuning for natural frequency constraints and the load updating. For the four case studies, cross-section optimizations are performed with constant load condition calculated by the multi-body simulation of the rotor blade and in each case study, different design variables are included in the optimization process in order to observe the effect of each design variable on the optimum blade configuration.

From the results obtained by the case studies the following conclusions are drawn.

- It is seen that when all of the four design variables are used in the optimization process, highest reduction can be achieved in the mass of the functional region of the blade.
- Convergence time increases with the number of variables.
- Spanwise ply drop-off position (design variable x4) has the highest contribution to mass reduction, as expected.
- Up to 16.34% mass reduction is achieved without mass tuning and natural frequncy check.

From the results obtained by the full blade optimization, the following conclusions are drawn.

- The axial blade loads (F_1) decrease at every iteration because mass reduction causes lower centrifugal loads at every step.

- Up to 16.55% mass reduction is obtained without changing the topology of the blade and with the use of four of the design variables. It is to be noted that, 2.31 kg tuning mass is also counted while calculating the mass of the functional region. If mass contribution of tuning mass is not considered, the weight reduction of the functional region is 22.81%.
- The optimized solution is obtained in only 3 FBO iterations. This shows that considerable computational time can be saved compared to including Dymore multi-body solution to update loads in every optimization step in the cross-section optimization.
- Peak point positions of mode shapes has not been changed significantly as it is assumed.
- Lumped mass attachment at the peak regions of the mode shapes properly works for mass tuning and satisfying the natural frequency constraint.
- Self-tuning of the torsional mode is achieved because the polar moment of inertia is decreased by the optimization process itself, as it is expected.
- The spanwise starting position of the thin section is selected as the critical section in terms of preliminary strength concerns. Upper-LE side of the blade is the critical position for this cross-section. It is to be noted that, spar, skin, erosion shield, inner-outer wraps and dummy heater mat are all close to this point. More detailed strength analysis and testing may be necessary for the further design stages of the blade for this section such as fatigue assesment.
- Optimized blade satisfies the strength, natural-frequency and sectional-center constraints.
- Design variables, nose mass radius (X_2) and number of spar plies (X_3), converged to the lower design boundaries. Since the lower boundary of the nose mass radius is considerably small, removal of nose mass may lead to a feasible design and save production cost.

This study can be enhanced in terms of the flight condition spectrum, strength methodology and optimization efficiency. First of all, full blade optimization under

the centrifugal and aerodynamic loads using the two-step approach can be studied. This study can be conducted both in hover and forward flight conditions. Aerodynamic loads can be taken constant as centrifugal loads for each iteration of the full blade optimization and updated between iterations. Secondly, for the strength point of view, a fatigue methodology can be implemented such as “Peak to peak” or “Rainflow counting” under the flight conditions providing oscillatory loads. Hover and forward flight conditions with aerodynamic loads can be given as an example of flight conditions having oscillatory loads. Finally, a more efficient optimization approach can be investigated for the CSO optimization instead of GA used in this thesis study. Although GA is robust and applicable to the integer variables, the optimization efficiency still can be increased. Different global search algorithms can be employed such as Particle Swarm method or Simulated Annealing. In addition, GA or other global search algorithms can be combined with local search methods. It is to be noted that the efficiency of the optimization method changes according to optimization problem defined. Similar studies on rotor blade optimization and similar benchmark problems can be investigated in order to reach a more efficient method for this study.

REFERENCES

[1] P. D. Mangalgiri, “Composite materials for aerospace applications,” *Bull. Mater. Sci.*, vol. 22, no. 3, pp. 657–664, 1999.

[2] Salkind Michael J. and Geoffry S. Holister, “APPLICATIONS OF COMPOSITE MATERIALS,” 1973.

[3] D. H. Hodges, “a Review of composite rotor blade modeling,” *AIAA J.*, vol. 28, no. 3, pp. 561–565, 1990.

[4] C. E. S. Cesnik and D. H. Hodges, “VABS: A New Concept for Composite Rotor Blade Cross-Sectional Modeling,” *J. Am. Helicopter Soc.*, vol. 42, p. 27, 1997.

[5] W. Yu, V. Volovoi, D. H. Hodges, and X. Hong, “Validation of the variational asymptotic beam sectional analysis,” *AIAA J.*, vol. 40, no. 10, pp. 2105–2112, 2002.

[6] H. Chen, W. Yu, and M. Capellaro, “A critical assessment of computer tools for calculating composite wind turbine blade properties,” *Wind Energy*, vol. 13, no. 6, pp. 497–516, 2009.

[7] O. A. Bauchau, “DYMORE USER ’ S MANUAL,” 2007.

[8] D. Han, W. Yu, and S. Roy, “A geometrically exact active beam theory for multibody dynamics simulation,” *Smart Mater. Struct.*, vol. 16, pp. 1136–1147, 2007.

[9] O. A. Bauchau, “Computational Schemes for Flexible , Nonlinear Multi-Body Systems,” *Multibody Syst. Dyn.*, vol. 2, no. 2, pp. 169–225, 1998.

[10] O. A. Bauchau *et al.*, “Validation of flexible multibody dynamics beam formulations using benchmark problems,” *Multibody Syst. Dyn.*, vol. 37, no. 1, pp. 29–48, 2016.

[11] O. A. Bauchau and D. H. Hodges, “Analysis of Nonlinear Multibody Systems with Elastic Couplings,” *Multibody Syst. Dyn.*, vol. 3, pp. 163–188, 1999.

[12] J. Ku, “A HYBRID OPTIMIZATION SCHEME FOR HELICOPTERS WITH COMPOSITE ROTOR BLADES,” 2007.

[13] D. Crossley, W., Laananen, “Conceptual design of helicopters via genetic algorithm,” *J. Aircr.*, vol. 33, no. 6, pp. 1062–1070, 1996.

[14] P. Hajela, “Nongradient methods in multidisciplinary design optimization - Status and potential,” *J. Aircr.*, vol. 36, no. 1, pp. 255–265, 1999.

[15] S. B. Visweswaraiah, H. Ghiasi, D. Pasini, and L. Lessard, “Multi-objective optimization of a composite rotor blade cross-section,” *Compos. Struct.*, vol. 96, pp. 75–81, 2013.

[16] L. Li, V. V Volovoi, and D. H. Hodges, “Cross-sectional Design of Composite Rotor Blades,” pp. 1–11, 2007.

[17] D. A. Peters, M. P. Rossow, A. Korn, and T. Ko, “Design of helicopter rotor blades for optimum dynamic characteristics,” *Comput. Math. with Appl.*, vol. 12, no. 1 PART A, pp. 85–109, 1986.

[18] J. L. Walsh and A. Chattopadhyay, “Minimum Weight Design of Helicopter Rotor Blades with Frequency Constraints,” *Optimization*, no. February, 1988.

[19] Z. Gürdal, R. T. Haftka, and P. Hajela, *Design and optimization of laminated composite materials*. John Wiley & Sons, 1999.

[20] R. P. Thornburgh, A. R. Kreshock, and M. L. Wilbur, “Structural Optimization of Active-Twist Rotor Blades,” *Proc. 67th Annu. Forum Am. Helicopter Soc.*, 2011.

[21] C. J. He and D. A. Peters, “Optimization of rotor blades for combined structural, dynamic, and aerodynamic properties,” *Struct. Optim.*, vol. 5, no. 1–2, pp. 37–44, 1992.

[22] “Damage Tolerance and Fatigue Evaluation of Composite Rotorcraft Structures,” in *Federal Aviation Administration Advisory Circular (AC) 29–2C*, Federal Aviation Administration, 2014, pp. C132–C164.

[23] H. A. Armstrong, “Rotorcraft Directorate Policy, Certification Secondary Composite Structure Memorandum.” Federal Aviation Administration, 1998.

[24] V. Volovoi, S. Yoon, C.-Y. Lee, and D. H. Hodges, “Structural optimization of composite rotor blades,” in *Collection of Technical Papers - AIAA/ASME/ASCE/AHS/ASC Structures, Structural Dynamics and Materials Conference*, 2004, vol. 5.

[25] W. Yu, D. H. Hodges, V. Volovoi, and C. E. S. Cesnik, “On Timoshenko-like modeling of initially curved and twisted composite beams,” *Int. J. Solids Struct.*, vol. 39, no. 19, pp. 5101–5121, 2002.

[26] R. V. Grandhi and V. B. Venkayya, “Structural optimization with frequency constraints,” *AIAA J.*, vol. 26, no. 7, pp. 858–866, 1988.

[27] R. Ganguli and I. Chopra, “Aeroelastic Optimization of a Helicopter Rotor to Reduce Vibration and Dynamic Stresses,” *AIAA J.*, vol. 34, no. 4, pp. 835–854, 1996.

[28] A. Chattopadhyay, A. Services, J. L. Walsh, and M. F. Riley, “Integrated AerodynamidDynamic Optimization of Helicopter Rotor Blades,” vol. 28, no. 1, pp. 58–65, 2028.

[29] O. A. Bauchau and J. I. Craig, *Structural Analysis*, vol. 163. 2009.

[30] S. P. Timoshenko, “X. On the transverse vibrations of bars of uniform cross-section,” *London, Edinburgh, Dublin Philos. Mag. J. Sci.*, vol. 43, no. 253, pp. 125–131, Jan. 1922.

[31] S. P. Timoshenko, “LXVI. On the correction for shear of the differential equation for transverse vibrations of prismatic bars,” *London, Edinburgh, Dublin Philos. Mag. J. Sci.*, vol. 41, no. 245, pp. 744–746, May 1921.

[32] M. Borri and T. Merlini, “A large displacement formulation for anisotropic beam analysis,” *Meccanica*, vol. 21, no. 1, pp. 30–37, 1986.

[33] W. Yu and D. H. Hodges, “Errata: Generalized Timoshenko Theory of the Variational Asymptotic Beam Sectional Analysis,” *J. Am. Helicopter Soc.*, vol. 50, no. 1, pp. 46–55, 2005.

[34] W. Yu, D. H. Hodges, V. V. Volovoi, and E. D. Fuchs, “A generalized Vlasov theory for composite beams,” *Thin-Walled Struct.*, vol. 43, no. 9, pp. 1493–1511, 2005.

[35] B. Popescu and D. H. Hodges, “Asymptotic treatment of the trapeze effect in finite element cross-sectional analysis of composite beams,” *Int. J. Non. Linear. Mech.*, vol. 34, no. 4, 1999.

[36] W. Yu and D. H. Hodges, “Elasticity Solutions Versus Asymptotic Sectional Analysis of Homogeneous, Isotropic, Prismatic Beams,” *J. Appl. Mech.*, vol. 71, no. 1, p. 15, 2004.

[37] H. Chen and W. Yu, “Manual of PreVABS,” *Stress Int. J. Biol. Stress*, pp. 1–11, 2008.

[38] A. J. Chipperfield and P. J. Fleming, “The MATLAB genetic algorithm toolbox,” *Appl. Control Tech. Using MATLAB, IEE Colloq.*, p. 10/1-10/4, 1995.

[39] A. Chipperfield, P. Fleming, and H. Pohlheim, “Genetic Algorithm Toolbox for use with MATLAB,” *Dep. Autom. …*, 1994.

[40] MathWorks, “Global Optimization Toolbox User ’ s Guide,” *Order A J. Theory Ordered Sets Its Appl.*

[41] C. W. Ahn, *Practical genetic algorithms*, vol. 18. 2006.

[42] D. E. Goldberg, *Genetic Algorithms in Search, Optimization, and Machine Learning*, vol. Addison-We. 1989.

[43] K. Deep and M. Thakur, “A new mutation operator for real coded genetic

algorithms," *Appl. Math. Comput.*, vol. 193, no. 1, pp. 211–230, 2007.

[44] K. Deep and M. Thakur, "A new crossover operator for real coded genetic algorithms," *Appl. Math. Comput.*, vol. 193, no. 1, pp. 211–230, 2007.

[45] K. Deep, K. P. Singh, M. L. Kansal, and C. Mohan, "A real coded genetic algorithm for solving integer and mixed integer optimization problems," *Appl. Math. Comput.*, vol. 212, no. 2, pp. 505–518, 2009.

[46] D. D. Samborsky, T. J. Wilson, P. Agastra, and J. F. Mandell, "Delamination at Thick Ply Drops in Carbon and Glass Fiber Laminates Under Fatigue Loading," *J. Sol. Energy Eng.*, vol. 130, no. 3, p. 22, 2008.

[47] H. Hirsch, R. E. Hutton, and A. Rasumoff, "Effect of Spanwise and Chordwise Mass Distribution on Rotor Blade Cyclic Stresses," *Journal of the American Helicopter Society*, vol. 1, no. 2. pp. 37–45.

[48] W. Yu, "VABS Manual for Users," pp. 1–22, 2013.

[49] MIL HDBK-17-2F, "Composite Materials Handbook," *Def. Stand. Progr. Off.*, vol. 2–5, no. June, p. 689, 2002.

[50] M. HDBK-17-3, *Handbook Composite Materials Handbook Volume 3 . Polymer Matrix Composites*, vol. 3, no. June 2002. 2003.

[51] R. C. Rice, J. L. Jackson, J. Bakuckas, and S. Thompson, *Metallic Materials Properties Development and Standardization (Mmpds)*, no. January. 2013.

[52] (3M), "Technical Datasheet: Scotch-weld Structural Adhesive Film AF163-2," 2009.

[53] J. Tomblin, J. Mckenna, Y. Ng, and K. S. Raju, "B-Basis Design Allowables for Epoxy-Based Prepreg: Newport E-Glass Fabric 7781/NB321," *Adv. Gen. Aviat. Transp. Exp.*, no. September, pp. 2–120, 2001.

[54] M. H. Aliabadi, *Woven Composites*, vol. 1. 2015.

[55] HEXCEL, “HexWeb ® HRH-10,” *Prod. Data Sheet*, pp. 1–6, 2017.

[56] S. Guruswamy, *Engineering Properties and Applications of Lead Alloys*, vol. 9. 1999.

APPENDIX A

STIFFNESS AND MASS MATRIX TERMS & DEFINITION OF CRITICAL CENTERS

The stiffness and mass matrices are tabulated in Table A1 and Table A2 respectively. The stiffness matrix is diagonally symmetric. The diagonal terms of the stiffness matrix are the main deformation stiffness terms. The mass matrix is also diagonally symmetric. The non-diagonal terms are the coupling terms of main deformations. The symbols used to define stiffness and mass matrix terms are compatible with the symbols used in VABS manual [48].

The components of the critical centers are symbolized. Sectional properties and sectional centers are calculated with respect to S_{ref} S_{ref} is the cross-sectional reference axis system where the origin is the FA, "1" direction is towards outboard of the blade, "2" direction is parallel to the chord line towards leading edge and "3" direction is towards the upper surface satisfying the right-hand rule. Hence, cross-sections are modeled without twist. The detailed definition of S_{ref} is given in Reference Axis System & Twist Definition section. It is to be noted that "2" and "3" vector components of S_{ref} has the same meaning of chordwise and flapwise direction terms respectively. Critical centers used in this thesis are the center of gravity (CG or mass center), the neutral axes (NA or tension center), and shear center (SC or the elastic axis). x_{m2} is the location of the CG in the chordwise direction. x_{m3} is the location of the CG in the flapwise direction. x_{s2} is the location of the SC in the chordwise direction. x_{s3} is the location of the SC in the flapwise direction. x_{t2} is the location of the NA in the chordwise direction. x_{t3} is the location of the NA in the flapwise direction.

Table A1 Terms of Stiffness Matrix

S_{11}, axial stiffness	S_{12}	S_{13}	S_{14}	S_{15}	S_{16}
	S_{22}, flapwise shear stiffness	S_{23}	S_{24}	S_{25}	S_{26}
		S_{33}, chordwise shear stiffness	S_{34}	S_{35}	S_{36}
			S_{44}, torsional stiffness	S_{45}	S_{46}
				S_{55}, flapwise bending stiffness	S_{56}
					S_{66}, chordwise bending stiffness

Table A2 Terms of Mass Matrix

μ, mass per spanwise length	0	0	0	$\mu * x_{m3}$	$- \mu * x_{m2}$
	μ, mass per spanwise length	0	$- \mu * x_{m3}$	0	0
		μ, mass per spanwise length	$\mu * x_{m2}$	0	0
			$m_{11} = (m_{22} + m_{33})$, polar moment of inertia	0	0
				m_{22} flapwise mass moment of inertia	m_{23}, product of inertia
					m_{33}, chordwise mass moment of inertia

APPENDIX B

MATERIAL PROPERTY TABLE

Table B1 Material Property Table

MATERIAL		S2 Glass Epoxy (S2-449 43.5k/ SP 381 UD tape)	Carbon Fiber Epoxy (T-300 15k/976 UD tape)	AISI 301 1/4 H	Film Adhesive (AF 163-2K Film-red)	E-Glass (Newport E-Glass Fabric 7781 / NB321)	Nomex Honeycomb (nomexhrh 10 1/8-3)	Lead
E_{11}	[MPa]	**47640**	**135137**	**186204**	**1110**	**28130**	0.1	**16000**
E_{22}	[MPa]	**13310**	**9239**	**186204**	**1110**	**28130**	0.1	**16000**
E_{33}	[MPa]	*13310*	*9239*	**186204**	**1110**	12200	**621**	**16000**
G_{12}	[MPa]	**4750**	**6274**	**73084**	**414**	**4206**	0.1	**5555**
G_{13}	[MPa]	*4750*	*6274*	**73084**	**414**	*10251*	**121**	**5555**
G_{23}	[MPa]	*4440*	*3000*	**73084**	**414**	*10251*	**76**	**5555**
v_{12}	[-]	0.296	**0.31**	**0.27**	**0.34**	**0.138**	0.001	**0.44**
v_{13}	[-]	0.296	*0.31*	**0.27**	**0.34**	0.372	0.001	**0.44**
v_{23}	[-]	0.499	0.54	**0.27**	**0.34**	*0.372*	0.001	**0.44**
Density	[kg/m^3]	**1850**	**1620**	**7916**	**1210**	**1830**	**48**	**11340**
Ply Thickness	[mm]	**0.226**	**0.134**	-	**0.24**	**0.25**	-	-
Reference	-	[49],[50]	[49],[50]	[51]	[52]	[53][54]	[55]	[56]

Bold	First reference
Underlined	Second reference
Italic	Estimated by assuming transversely isotropy

Assumptions:

- RTD (Room Temperature & Dry Conditioned) & mean values of the properties are used.
- Unidirectional composites (S2 glass epoxy and carbon fiber epoxy) behave as transversely isotropic materials.

- In litterature, v_{23} value of the selected carbon fiber epoxy (T-300 15k/976 UD tape) and v_{23} value of the selected S2 glass epoxy (S2-449 43.5k/SP 381 UD tape) are not available. However, for unidirectional composites, v_{23} value does not considerably affect the overall behavior as it is mentioned in [50]. Considering this penomennon, v_{23} values of different kinds of carbon fiber epoxy and S2 glass epoxy materials are used to complete the material property table. v_{23} value of S2/3501-6 56.5% FVF and v_{23} value of AS1/3501-6 59.5% are used as properies of S2 glass epoxy and carbon fiber epoxy material, respectively.
- Data of S2/3501-6 56.5% FVF is used as v_{12} value of S2 glass epoxy because v_{12} is not available in the first reference [49] of S2 glass material column given in Table B1.
- For the missing experimental E-glass properties in the thickness direction, computational solution properties of Hybon 2022 woven E-glass material in thickness direction are used to complete the material table. It is to be noted that 7781 woven E-glass and Hybon 2022 woven E-glass have similar in-plane properties.

APPENDIX C

PREVABS INPUT EXAMPLE

Prevabs input is composed of 4 text files. These files are control input, layup input and material input and profile input. Example files of an airfoil having 2 webs are given below.

Control Input File

!---

! (I) input file names

! (I.1) the file name for sectional profile (outer surface)

1examp_profile.Input

! (I.2) the file name for cross-sectional chordwise layup configuration (lamina schema file)

1examp_layup.Input

! (I.3) name of the input file for material properties

1examp_material.Input

! (I.4) output file names (VABS input file names) for later VABS' running

examp_rectangular

!---

! (II) Plot control parameters

! (II.1) Plot rotated, shifted and dimensional outer profile? (plot_profile), 'yes' or 'no'

yes

! (II.2) Do you want to monitor the coarse mesh-generating processing (generate quadratical and/or triangluar areas)?

! 'yes' or 'no' ('Is_plot_area')

yes

! (II.3) Do you want to plot the final meshed results?

! 'yes' or 'no' ('plot_glbelm_mesh')

Yes

!---

! (III) Modeling parameters

! (III.1) Define relative mesh_size for element meshing (RMS)

! (relative ratio of the element width to mininum layer thickness)

6

!---

Profile Input File

! Sec_profile_real_balde_exam5_MH104_R173_258.input

!===
===

! (1) Chord length (in)   twisted angle (deg)   pitch axis location (x y) (in)

!===
===

       100.0   3.0   0.000

!===
===

! (2) (a) Nondimensional positions for Web centers ((x,y) position for the center of each web)

!   (b) webs' tittling angles (w.r.t. chord line)

!   Web center should be on the cord line (y=0.0)

```
!=====================================================================
===
! Total number of webs in this cross section
!    Nwebs
      2
!    Webi_nd_x, Webi_nd_y     Web_tl_angles (deg)
      .10      0.0             90
      .35      0.0             90
!=====================================================================
===
! (3)  Nondimensional profile data for low pressure surface (LPS)
!=====================================================================
===
!  chord line status  'Tilt' or 'Regular'
!  Currently (8/08) always 'Regular' -->: farthest trailing edge point lies on the
      Regular
!   chord line rotation angle (deg)  (0 deg if cord line is on x axis)
      0.0
!      number of knods @ LPS   (top surface)
57
!      x       y (nondimensional)
0          0
0.00405394         0.0117348
.                      .
.                      .
```

. .

0.99725665 0.0001336

1.00E+00 0.00E+00

!===
===

! (5) Nondimensional profile data for high pressure surface (HPS)

!===
===

! number of knods @ HPS (bottom surface)

58

! x y (nondimensional)

0 0

0.00682453 -0.00988165

. .

. .

. .

0.9970425 -0.00036119

1 0

Layup Input File

! Sec_Layup_Confg_real_balde_exam5_MH104_R173_258.input

!===
===

! (1) Chordwise lamina data for low press surface (LPS, top surface)

! (thickness or offset, ply angle, and material ID)

```
!=========================================================================
===

!Surface indicator ('Low_PS' or 'High_PS', (top/bottom surface))  Id_Hig_low_PS

      Low_PS

! Total number of chordwise segments (N_segm)

      3

! Segment number

! Segment number for a particular cross section must run from leading edge to trailing edge

! and in that order.

!      Left  Middle  Right

      1       2       3

!-------------------------------------

! Segment No. 1 (LE)

!---------------------

! Starting and ending node number of Segment No. #1

! node here refers to the spline node used generate the foil cross section profile.

! starting node            ending node

    1                    15

! Number of lamina in this segment

3



! thickness (in)   fiber orientation (deg)   material id

0.02    -30           1

0.03        0          1
```

0.02 30 1

!-------------------------------------

! Segment No. 2 (Sand_1)

!-------------------------------------

! Starting and ending node number of Segment No. #2

! node here refers to the spline node used generate the foil cross section profile.

! starting node ending node

15 34

! Number of lamina in this segment

5

! thickness (in) fiber orientation (deg) material id

0.01 -45 1

0.02 -30 1

0.03 0 1

0.02 30 1

0.01 45 1

!-------------------------------------

! Segment No. 3 (Spar_Cap)

!-------------------------------------

! Starting and ending node number of Segment No. #3

! node here refers to the spline node used generate the foil cross section profile.

! starting node ending node

34 57

! Number of lamina in this segment

1

! thickness (in) fiber orientation (deg) material id

0.02 0 1

!===
===

! (2) Chordwise lamina data for high press surface (HPS, bottom surface)

! (thickness or offset, plyer angle, and material ID)

!===
===

!Surface indicator ('Low_PS' or 'High_PS') Id_Hig_low_PS

High_PS

! Total number of cordwise segements (N_segm)

3

! Segement number

! Segment number for a partilar cross section MUST run from leading edge to trailing edge

! and in that order.

! Left Middle Right

1 2 3

!-----------------------------------

! Segment No. 1 (LE)

!-----------------------------------

! Starting and ending node number of Segement No. #1

! node here refers to the spline node used generate the foil cross section profile.

! starting node ending node

```
     1                   15
! Number of lamina in this segment
3
! thickness (in)   fiber orientation (deg)   material id
0.02    -30           1
0.03        0         1
0.02        30        1
!-------------------------------------
! Segment No. 2 (Sand_1)
!-------------------------------------
! Starting and ending node number of Segement No. #2
! node here refers to the spline node used generate the foil cross section profile.
! starting node             ending node
     15                   34
! Number of lamina in this segment
5
! thickness (in)   fiber orientation (deg)   material id
0.01       -45       1
0.02    -30          1
0.03        0        1
0.02        30       1
0.01        45       1
!-------------------------------------
! Segment No. 3 (Spar_Cap)
```

```
!-----------------------------------

! Starting and ending node number of Segment No. #3

! node here refers to the spline node used generate the foil cross section profile.

! starting node            ending node

    34                    58

! Number of lamina in this segment

1

! thickness (in)   fiber orientation (deg)   material id

0.05       0          1

!====================================================================

!  (3)  Webs layup configuration data

!       (thickness or offset, plyer angle, and material ID)

!====================================================================

! Total number of webs in this cross section

      2

! (3.1) lamina layup configuration of Web 1: main shear web

!-------------------------------------------

! Number of lamina: Nweb1

5

! thickness (in)   fiber orientation (deg)   material id

0.001     -45        1

0.002    -30         1

0.003      0         1

0.002      30        1
```

0.001 45 1

! (3.2) lamina layup configuration of Web 2: aft shear web

!----------

! number of lamina: Nweb 2

5

! thickness (in) fiber orientation (deg) material id

0.001 -45 1

0.002 -30 1

0.003 0 1

0.002 30 1

0.001 45 1

! (3.3) lamina layup configuration of Web 3

!----------

! number of lamina: Nweb 3

0

!thickness (in) fiber orientation (deg) material id

! (3.4) lamina layup configuration of Web 4

!----------

! number of lamina: Nweb 4

0

!thickness (in) fiber orientation (deg) material id

Material Input File

! VABS title flags

```
!=====================================================

! Timoshenko_flag   recover_flag  thermal_flag

1   0   0

!  curve_flag (k1 (deg/in), k2, k3)   oblique_flag   Trapeze_flag   Vlasov_flag

        0                        0            1            1

!=====================================================

! MAterial Properties

!=====================================================

! number of material ids

1


! Material Properties

! material ID 1      orth_flag 1

1   1

!      E1          E2            E3     (lb/in^2)

5.3664E+06       1.3053E+06       1.3053E+06

!      G12         G13           G23    (lb/in^2)

5.8015E+05       5.8015E+05       5.8015E+05

!      nu12        nu13          nu23

       0.28        0.28          0.28

!  rho  (lb-sec^2/in^4)

1.740449E-04
```

APPENDIX D

VABS INPUT FILE EXAMPLE

VABS input file example of a beam having an L shaped cross-section is given below. The elements of the cross-section is composed of composite materials.

```
0 0

1 0  0  #Timoshenk_flag recover_flag thermal_flag

0 0 0 0  # curve_flag oblique_flag trapeze_flag Vlasov_flag


8        3        1 # nnode, nelem, nmat


1        -0.5     -0.5 #coordinates of the nodes

2        0.5      -0.5

3        1.5      -0.5

4        -0.5     0.5

5        0.5      0.5

6        1.5      0.5

7        -0.5     1.5

8        0.5      1.5

1        2        5        4        1        0        0        0        0        0        #        element
connectivity

2        2        3        6        5        0        0        0        0        0

3        4        5        8        7        0        0        0        0        0
```

1 1 0 180.0 540 0 0 0 0 0 0 0 # mat_id & orientation of layups in each element

2 1 0 180.0 540 0 0 0 0 0 0 0

3 2 0 180.0 540 0 0 0 0 0 0 0

1 1 # mat_id, orthotropy flag

4.50E+04 1.33E+04 1.33E+04 #E11 E22 E33

4.81E+03 4.81E+03 4.81E+03 #G12 G13 G23

2.80E-01 2.81E-01 3.80E-01 #v12 v13 v23

1.85E-09

2 1 # mat_id, orthotropy flag

1.05E+02 1.05E+02 1.05E+02 #E11 E22 E33

4.20E+01 4.20E+01 4.20E+01 #G12 G13 G23

2.50E-01 2.50E-01 2.50E-01 #v12 v13 v23

7.50E-11

0 0 0

1 0 0

0 1 0

0 0 1

1.0 0.0 10.0000E+00 0.0 # F1 M1 M2 M3

0.0 0.0 # F2 F3

APPENDIX E

PENALTY PARAMETER, POPULATION SIZE AND CONVERGENCE CRITERION SELECTION FOR CROSS-SECTION OPTIMIZATION (CSO)

In this thesis, Genetic Algorithm is utilized for the CSO. Constructing suitable optimization parameters for GA is essential. For the most of these parameters, the information of problem definition and types of design variables used is sufficient. However, several trials are necessary for some of them because they are problem specific and can be decided their convenience from the trial outputs. In this study, these trials are needed for suitable Penalty parameter (*r*, see Section 3.3.3) and population size (*i*, see Section 3.3.1.2) selection. These trials are applied for the case studies and suitable parameters are selected for each case study.

For the penalty parameter, powers of 10 are tested such as 10^1 and 10^2. As it mentioned in Section 3.3.1.2, values suggested for a population size differs between 30 and 100. Up to %0.5 constraint violation is assumed acceptable for the normalized constraints and it also means that the solution is converged to the constraint boundary. In order to observe convergence behavior, each trial of each case is not stopped until it reaches 25 generations. It is to be noted that the convergence of each trial is satisfied in 25 generations within 10^{-3} objective difference. The trials are started from the Case 1 which has the lowest number of variables because faster convergence than the other cases is expected from the trials of Case 1. Suitable penalty parameter and population size are obtained from the trials of Case 1. The obtained parameters for Case 1 are used as a starting point for the trials of the other cases. Case 1, Case 2, Case 3 and Case 4 are subjected to trials respectively. The outputs of the trials are given in Table E1.

Firstly, Case 1 is taken into account. In the first trial of Case 1, penalty parameter is taken as 10 for the first and second trials. 40 and 70 are utilized as population size for the first and second trials respectively. The second trial gives a lower objective value

with unacceptable constraint violation for $Constraint_3$. Considering this violation, the second trial is repeated as the third trial by increasing the penalty parameter from 10 to 100 without changing population size. Since the output is converged to the constraint boundary for $Constraint_3$ within acceptable violation, active parameters for the third trial (r= 100 and i = 70) is found as suitable and the trials are stopped for the Case 1.

Secondly, Case 2 is taken into account. Two trials are completed for r = 100 (first trial) and r = 10 (second trial) by taking population size constantly 70. The objective value obtained from the second trial is lower than the one obtained from the first trial. Besides, the optimization is converged to the constraint boundary for $Constrain_4$ within acceptable violation. The parameters of the second trial (r = 10 and i = 70) are found as suitable and the trials are stopped for the Case 2.

Thirdly, Case 3 is taken into account. Three trials are completed for r =10000 (first trial), r = 1000 (second trial), r = 100 (third trial) and r = 10 (fourth trial) by taking population size constantly as 70. It can be seen from the table that X_1, X_4 and the objective value is converging as the population size decreases from 10000 to 10. Besides, X_2 is converging to its lower design limit which is 0.6. Considering these convergences, the parameters of the trial where r = 10 and i = 70 are found as suitable and the trials are stopped for the Case 3.

Finally, Case 4 is taken into account. Four trials are completed for r = 10000 (first trial), r = 1000 (second trial), r = 100 (third trial) and r = 10 (fourth trial) by taking population size (i) constantly 70. The constraint convergence for $Constraint_4$ within acceptable violation and the minimum objective values are obtained at the third and the fourth trial. Since the constraint violation is lower for the third trial than the fourth trial, r = 100 and i = 70 are found as suitable and the trials are stopped for the Case 4.

Table E1 Outputs Obtained from the Case Study Trials for Various Penalty Parameters and Population Sizes

	Trial #	Penalty Parameter (*r*)	Population Size (*i*)	Number of Generations	Variables				Objective Value	Weight Value	Constraint Violation							
					X_1	X_2	X_3	X_4			$Constraint_1$	$Constraint_2$	$Constraint_3$	$Constraint_4$	$Constraint_5$	$Constraint_6$	$Constraint_7$	$Constraint_8$
Case 1	1	10	40	25	0.389	3.10	-	-	0.946	0.946	0	0	0	0	-	-	-	-
	2	10	70	25	0.367	3.13	-	-	0.933	0.927	0	0	2.40%	0	-	-	-	-
	3	**100**	**70**	**25**	**0.375**	**3.11**	**-**	**-**	**0.936**	**0.933**	**0**	**0**	**0.49%**	**0**	**-**	**-**	**-**	**-**
Case 2	**1**	**10**	**70**	**25**	**0.380**	**3.00**	**16**	**-**	**0.906**	**0.900**	**0**	**0**	**0**	**0.24%**	**-**	**-**	**-**	**-**
	2	100	70	25	0.392	3.18	18	-	0.937	0.937	0	0	0	0	-	-	-	-
Case 3	1	10000	60	25	0.379	3.10	-	0.513	0.855	0.855	0	0	0	0	0	0	0	0
	2	1000	70	25	0.390	3.22	-	0.491	0.861	0.861	0	0	0	0	0	0	0	0
	3	100	70	25	0.381	3.07	-	0.492	0.851	0.851	0	0	0	0	0	0	0	0
	4	**10**	**70**	**25**	**0.380**	**3.00**	**-**	**0.492**	**0.850**	**0.850**	**0**	**0**	**0**	**0**	**0**	**0**	**0**	**0**
Case 4	1	10000	70	25	0.381	3.21	12	0.414	0.865	0.865	0	0	0	0	0	0	0	0
	2	1000	70	25	0.380	3.00	8	0.540	0.838	0.838	0	0	0	0	0	0	0	0
	3	**100**	**70**	**25**	**0.379**	**3.01**	**8**	**0.540**	**0.837**	**0.837**	**0**	**0**	**0**	**0**	**0**	**0**	**0**	**0.07%**
	4	10	70	25	0.381	3.00	8	0.537	0.837	0.837	0	0	0	0	0	0	0	0.38%

Variation of fitness for Case 4 for the selected parameters is given in Figure E1 to illustrate the convergence criterion selection. 10^{-3} difference between iterations is assumed that convergence is achieved because the normalized fitness values are utilized. However, during the trials of Case 4, it is seen that convergence may not takes place even if the consecutive trials give lower than 10^{-3} difference. Local minimums may lead this behavior. A stair like decrement may occur as illustrated with red dashed rectangle. Three consecutive iterations give same results however decrement of fitness continues for the fourth iterations. During the trials no stair like decrement is seen if the difference between last 4 consecutive iterations is less than 10^{-3}. Considering these trials, the difference between the last and three iterations before must be under 10^{-3} to claim the convergence is achieved. Hence, for the given example, the convergence is accepted as achieved at the twenty-first iteration.

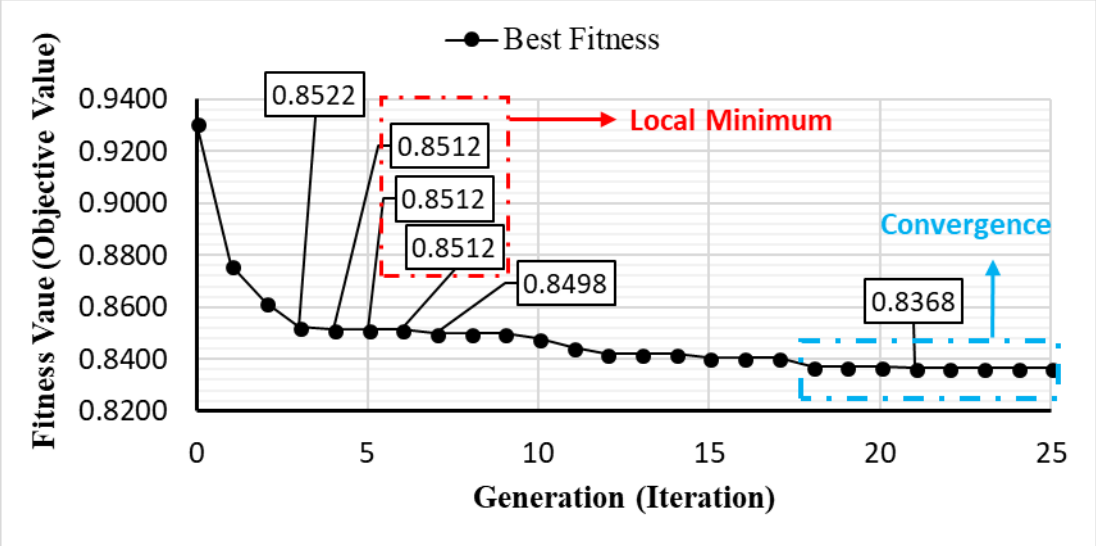

Figure E1 Fitness Variation and Convergence Details of Case Study 4